

1

NASA CONTRACTOR
REPORT



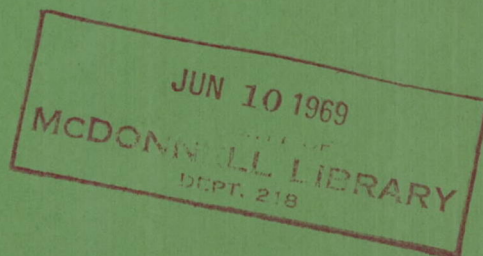
NASA CR-1359

NASA CR-1359
COPY ON MICROFICHE
169-28099

SOLID ELECTROLYTE SYSTEM
FOR OXYGEN REGENERATION

by L. Elikan and J. P. Morris

Prepared by
WESTINGHOUSE ELECTRIC CORPORATION
Pittsburgh, Pa.
for Langley Research Center



SOLID ELECTROLYTE SYSTEM FOR OXYGEN REGENERATION

By L. Elikan and J. P. Morris

Distribution of this report is provided in the interest of information exchange. Responsibility for the contents resides in the author or organization that prepared it.

Prepared under Contract No. NAS 1-7306 by
WESTINGHOUSE ELECTRIC CORPORATION
Pittsburgh, Pa.

for Langley Research Center

NATIONAL AERONAUTICS AND SPACE ADMINISTRATION

Page Intentionally Left Blank

ABSTRACT

Solid electrolyte electrolysis of carbon dioxide and water offers an attractive method for regenerating oxygen for long duration manned space flights. This work demonstrated that high efficiency multi-cell batteries employing $(\text{ZrO}_2)_{0.9}(\text{Y}_2\text{O}_3)_{0.1}$ electrolyte can be constructed and operated for periods exceeding 100 days. Three five-cell batteries were life-tested; their lives were 152, 112, and 77 days. The 152 day life test was carried out at 920°C employing a current density of 200 ma/cm^2 .

A continuous carbon deposition reactor, in which the CO in the $\text{CO-CO}_2\text{-H}_2\text{-H}_2\text{O}$ mixture produced by electrolysis was decomposed to form solid C and CO_2 , was operated for 100 days without interruption and without decline in catalyst activity. Over 60% conversion was obtained throughout the test. The carbon produced was dry, free flowing, and non-clogging. Palladium foils were found to be an effective means of removing H_2 from a $\text{CO, CO}_2, \text{H}_2, \text{H}_2\text{O}$ mixture. Operated at 800°C and above, no carbon deposition was observed on the foil.

Based on the performance of the multi-cell electrolysis battery, carbon deposition reactor, and palladium foils tested in this work, it is estimated that a solid electrolyte oxygen system can be built for a 4-man, 100-day mission which will weigh 121 pounds and require 1160 watts of power.

Page Intentionally Left Blank

ACKNOWLEDGEMENT

The research described in this report was carried out at the Westinghouse Research Laboratories under Contract Number NAS1-7306. The authors gratefully acknowledge the contributions of the following members of the staffs of NASA and Westinghouse: Charles G. Saunders, Contract Monitor, and Dan C. Popma of NASA Langley Research Center for their guidance in planning the work; D. H. Archer for his many suggestions and assistance in data interpretation; H. L. Taylor and G. N. Schneider for construction and testing of the electrolysis cells and batteries; T. E. Gestrich for the operation of the carbon deposition reactors and for chromatographic analysis; N. J. Maskalick and G. E. Zymboly for sputtering of Pt-ZrO₂ electrodes; P. Phillips and R. F. Geist for writing the equations of Appendix E; Dwight Clarke for testing of single cell devices; Judy Evans for mass spectrographic analysis; and the staff of the analytical chemistry laboratory for many analyses of Pt-ZrO₂ electrode deposits and of precipitated carbon.

Page Intentionally Left Blank

TABLE OF CONTENTS

	<u>Page</u>
ABSTRACT	iii
ACKNOWLEDGEMENT	v
1. INTRODUCTION AND SUMMARY	1
2. SOLID ELECTROLYTE ELECTROLYSIS	6
2.1 Principles of Operation	6
2.2 Evaluation of Electrode Materials	10
2.2.1 Cell Configuration and Test Apparatus	11
2.2.2 Performance of Sputtered Pt-ZrO ₂ Anodes	12
2.2.3 Performance of Sintered Platinum Anodes and Cathodes	14
2.2.3.1 Resistance and Polarization Measurements	14
2.2.3.2 Life Test of SCD #9	16
2.2.4 Performance of In ₂ O ₃ Anodes	20
2.2.5 Conclusions Based Upon the Testing of Single- Cell Devices	22
2.3 Evaluation of Cell Joining Techniques	23
2.3.1 Tightness and Conductivity of High-platinum Bell-and-spigot Joints	24
2.3.2 All Platinum Butt Joints	29
2.4 Performance of Multi-cell Batteries	29
2.4.1 Initial Performance Characterization	30
2.4.1.1 Overall Battery Performance - OBS #8	30
2.4.1.2 Initial Performance - OBS #9 and OBS #10	33
2.4.1.3 Individual Cell Performance	34
2.4.1.4 Power Efficiencies as a Function of Current Density	37
2.4.1.5 Effect of Feed Gas Composition	37
2.4.2 Life Test Results	38
2.4.2.1 OBS #8	38
2.4.2.2 OBS #9	46
2.4.2.3 OBS #10	52
2.4.2.4 Time Variation of Current Efficiency	52
2.4.2.5 Time Variation of Power Efficiency	56
2.4.2.6 Effects of Fabrication Variables and Conditions	59
2.4.3 Battery Performance Summary	62

3.	CARBON PRECIPITATION FROM CO-CO ₂ -H ₂ MIXTURES.....	64
3.1	Catalyst Evaluation Study with Packed-Bed Reactor.....	65
3.2	Continuous Reactor Experiments.....	69
3.3	100 Day Life Test of Continuous Carbon Deposition Reactor.....	73
3.3.1	Description of Reactor.....	73
3.3.2	Start Up and Procedure.....	77
3.3.3	Results of 100-Day Test.....	78
3.3.3.1	Description of Carbon.....	82
3.3.3.2	Condition of Catalyst Liner at End of Test.....	82
3.3.3.3	Condition of Carbon Scraper.....	85
3.3.3.4	Conversion of H ₂ to H ₂ O.....	88
3.3.3.5	Hydrocarbon Formation in Reactor.....	89
3.3.3.6	Effect of H ₂ on Carbon Deposition Rate..	90
3.3.4	Development of Mathematical Model for Carbon Deposition.....	90
3.3.4.1	Effect of Temperature on Carbon Deposition.....	96
4.	HYDROGEN SEPARATION STUDY.....	98
4.1	Experimental Procedure.....	99
4.2	Results.....	99
5.	SYSTEMS ANALYSIS - AN INTEGRATED OXYGEN REGENERATION SYSTEM..	102
5.1	The Electrolysis Battery.....	104
5.1.1	Computation of Battery Weight.....	106
5.1.2	Method of Optimization-Geometric Programming.....	109
5.1.3	The Optimal Design.....	110
5.2	The Carbon Deposition Reactor.....	114
5.2.1	Design Equations.....	114
5.3	The Heat Exchangers.....	118
5.4	Overall System Optimization.....	126
6.	CONCLUSIONS AND RECOMMENDATIONS.....	128
6.1	Conclusions Concerning Overall System Operability.....	128
6.2	Conclusions Concerning Design, Construction, and Operation of Major System Components.....	129

6.2.1	The Electrolysis Battery.....	129
6.2.2	Carbon Deposition.....	130
6.2.3	H ₂ Removal.....	131
6.3	Recommendations.....	131
Appendix A	Determination of Open-Circuit Voltage for C-H-O System.....	133
Appendix B	Methods Used to Determine Ohmic and Polarization Losses.....	140
Appendix C	Electrode Application Techniques.....	144
C.1	Sputtered Platinum Zirconia Anodes.....	144
C.2	Sintered Platinum Electrodes (anodes and cathodes).....	146
C.3	Indium Oxide Electrodes.....	147
Appendix C	Cell Joining Techniques.....	149
D.1	Bell and Spigot Joints.....	149
D.2	All Platinum Butt Joints.....	151
Appendix E	153
	Equations for Computerized Heat Transfer Computations.....	153
	Nomenclature Listing for Heat Exchanger Simulation.....	159
Appendix F	Daily Log of 100-day Life Test of Carbon Deposition Reactor.....	162
REFERENCES	165

ILLUSTRATIONS

<u>Figure</u>	<u>Title</u>	<u>Page</u>
1	Schematic of solid-electrolyte oxygen production cell	7
2	Electrolyte resistivity-temperature characteristics (Y_2O_3 stabilized ZrO_2)	9
3	Photomicrograph of discontinuity between oxygen electrode and bell-and-spigot joint	10
4	Schematic drawing of SCD device	11
5	Total driving voltage as a function of current for cells of SCD #9 at 1000°C	14
6	Life test performance of SCD #9 at driving voltage of 1.7 volts	17
7	Cell current as a function of total driving voltage for cells of SCD #9 at 900°C just prior to start of life test	17
8	SCD #9 after 102 days of continuous testing at 900°C	18
9	Bare electrolyte tube surface of In_2O_3/Pt working cell after In_2O_3 had been reduced by hydrogen at approximately 1000°C. (5X magnification)	22
10	Five-cell electrolysis battery after construction	25
11	Pictures of OBS #5 after failure	28
12	Overall voltage required as a function of current density for OBS #8 at 1000°C	30
13	Overall voltage required for OBS #8 at 920°C	31
14	Total battery voltage vs current-density OBS #9	34
15	Total driving voltage vs current density for OBS #10 at 1000°C	34
16	Current interrupt pictures of OBS #8	35

17	V-I curves for individual cells of OBS #10 during initial characterization	36
18	Performance of the five cells of OBS #8 during life tests	39
19	Cell resistance of OBS #8 at 920° vs time	40
20a	Picture of OBS #8 after failure	41
20b	Pictures of individual cells of OBS #8 after failure	42
20c	Pictures of individual cells of OBS #8 after failure	43
20d	Pictures of individual cells of OBS #8 after failure	44
21	Current flow in cell after high resistance develops in outside electrode	45
22a	Pictures of OBS #9 after failure	47
22b	Pictures of individual cells of OBS #9 after failure	48
22c	Pictures of individual cells of OBS #9 after failure	49
22d	Pictures of individual cells of OBS #9 after failure	50
23	Performance of the five cells of OBS #9 during life test	51
24	Picture of OBS #10 after failure	53
25	Performance of the five cells of OBS #10 during life test	54
26	Battery test apparatus including feed system and oxygen flow rate measurement	57
27	Power efficiency of the batteries during life test	58
28	Time to failure as a function of joint composition	61
29	Packed bed carbon-deposition reactor	65
30	Typical conversion of CO as a function of time when H ₂ was not included in feed	66
31	Schematic diagram of 100-day carbon deposition reactor	74

32	Carbon deposition reactor and auxiliary equipment used in continuous 100-day test	76
33	Log of 100-day life test of carbon deposition reactor	80
34	Carbon produced on 74th day of continuous 100-day test	83
35	Temperature profiles in carbon deposition reactor and variation of catalyst wall thickness with length at end of test	84
36	Section through carbon deposition reactor at end of 100-day test	85
37	View of inlet end of carbon deposition reactor, showing region of maximum corrosion of catalyst liner	86
38	View of gas outlet end of carbon deposition reactor	87
39	Variation of CO conversion with H_2 content of feed gas	90
40	Plot of $X - X_e / X_o - X_e$ versus distance along reactor in uniform temperature zone	92
41	Predicted local Nusselt numbers plotted vs local Graetz numbers for parabolic velocity profile and uniform wall temperature after McAdams ¹⁶ p. 233	93
42	Effect of temperature on CO conversion	96
43	Temperature dependence of $p_{CO_2} / (p_{CO})^2$ in low flow rate tests compared with the reaction equilibrium constant	97
44	Schematic diagram of H_2 diffusion apparatus	98
45	Results of H_2 diffusion study with palladium tube	101
46	Flow diagram of oxygen regeneration system	103
47	Schematic cross section of electrolysis battery	105
48	Heat exchanger design parameters	119
49	Heat flow for a generalized countercurrent heat exchanger	123
A1	Thermodynamic voltage, E_t , as a function of the percent of available oxygen removed and as a function of H/C at 1023°C	137

A2	Thermodynamic voltage, E_t , at 923°C	138
A3	Effect of temperature on E_t at fixed H/C ratio	139
B1	Illustration of method used to obtain IR and V_p from V-I curves	140
B2	Minimum decomposition voltage as a function of total current drawer when the inlet gas flow equals 280 cc/min	141
B3	Use of current interrupt photo to determine IR, E_t and V_p	142
C1	Apparatus used for spraying $ZrO_2Y_2O_3$ tube with Sn doped In_2O_3	148
D1	Section view of bell and spigot segment before and after electrode application	150
D2	Butt jointing apparatus	152

TABLES

<u>Table</u>	<u>Title</u>	<u>Page</u>
I	Initial Performance at 1000°C of Cells with Sputtered Pt-ZrO ₂ Anodes	13
II	Initial Performance of SCD #9 at 1000°C	15
III	$\frac{\rho_a}{\delta_a}$ vs Time of Operation for the In ₂ O ₃ Electrode of SCD #2	21
IV	Composition, Tightness, and Conductivity of Bell-and-Spigot Joints	26
V	Comparison of Curve-Computed Cell Parameters vs Current Interrupt Photo-Computed Parameters for OBS #8 at 0.4 amps	32
VI	Initial Power Efficiency of Life Tested Batteries	37
VII	Current Efficiency Measurements OBS #8	55
VIII	Fabrication Summary for Life Tested Batteries	60
IX	Results of Carbon Deposition Tests with Packed Bed Reactor	67-68
X	Results of Carbon Deposition Tests with Stainless Steel Continuous Reactor	70
XI	Results of Carbon Deposition Tests with Carbon Steel-Lined Continuous Reactor	72
XII	Results of 100-Day Life Test of Carbon Deposition Reactor	79
XIII	Conversion of H ₂ to H ₂ O in Carbon Deposition Reactor and Comparison with Predicted Conversion	88
XIV	Methane Formation in Carbon Deposition Reactor	89
XV	Optimal Battery Design as a Function of Temperature	111

XVI	Description of 4-Man, 100-Day Carbon Deposition Reactor and Postulated Effects of Varying Diameter	117
XVII	Predicted Description of Heat Exchanger 1 as a Function of System Parameters	125
XVIII	Weight of the Optimum Overall System	127
C.1	Summary of Weights, Compositions, and Sputtering Cathode for the Pt-ZrO ₂ Electrodes of SCD's Number 3 through 8 ...	145

Page Intentionally Left Blank

SOLID ELECTROLYTE SYSTEM FOR OXYGEN REGENERATION

By L. Elikan and J. P. Morris
Westinghouse Electric Corporation

1. INTRODUCTION AND SUMMARY

Regeneration of oxygen from respiratory carbon dioxide and water, rather than carrying a stored oxygen supply, appears to be an important means of reducing launch weight on future manned space flights of long duration.

Solid electrolyte electrolysis has a number of features which make it an attractive method of regenerating oxygen. Both water and carbon dioxide, as well as mixtures of the two, can be decomposed in the same battery. The oxygen produced requires no purification since it contains only CO_2 and H_2O as impurities, and it can be delivered to the space cabin at almost any desired pressure or temperature. No difficult gas-liquid separations at zero-g are required since no liquids are required for its operation. Since the electrolyte used is a stable oxide, no corrosion problems are encountered. Both the physical weight and power requirements for the operation of a solid electrolyte system are small, resulting in a low overall weight penalty.

The overall system required for solid electrolyte oxygen regeneration includes an electrolyses battery in which the reactions



are carried out; a carbon deposition reactor where the carbon deposited by the reaction



and removed from the system; a hydrogen diffusion cell where H_2 produced in the battery is removed by diffusion through a palladium membrane;

two heat exchangers; and a means of recycling the CO_2 produced in the reactor back to the electrolysis battery.

Considerable study of this system has already been performed. Elikan, Archer, and Zahradnik^{1(a)} have estimated the probable weight and power requirements on the basis of system thermodynamics, extensive experience in operating solid electrolyte fuel cells, and a limited number of electrolysis experiments. Chandler and his co-workers^{2,3,4} have demonstrated experimentally the feasibility of the total concept by constructing and operating a number of small scale solid electrolyte oxygen regeneration systems, including an engineering model^{3,4} which produced 150 cc/min of O_2 . However, while technical feasibility was demonstrated, performance was not. The weight and power requirements of Chandler's systems were high and the life achieved was short. Performance of the electrolysis unit appears to have been limited by the inefficiencies of the current collectors required for the large single cells used. Another difficulty was the loss of catalyst activity in the carbon deposition reactor after 137 hours operation.

Weissbart and Smart⁵ investigated a new solid electrolyte material, $(\text{ZrO}_2)_{0.85-x}(\text{CeO}_2)_x(\text{CaO})_{.15}$, with the hope of achieving higher performance at lower temperatures than was achievable with the $(\text{ZrO}_2)_{0.85}(\text{CaO})_{.15}$ and $(\text{ZrO}_2)_{0.9}(\text{Y}_2\text{O}_3)_{0.1}$ materials conventionally employed as solid electrolytes. However, reproducible current efficiency results were not obtained for the new electrolyte, and 100% efficiencies for $(\text{ZrO}_2)_{0.5}(\text{CaO})_{0.15}$ were reported as low as 785°C. Their predicted power requirement for a 1/8 man electrolysis battery was 64 watts, or 512 watts per man.

The objectives of this work were to demonstrate that (1) high-efficiency, multi-cell batteries of conventional solid electrolyte could be constructed and operated for a period of 100 days or longer, (2) a continuous carbon deposition reactor suitable for use in series with the electrolysis battery could be designed and operated for 100 days, and

(a) Reference numbers are placed superior to the line of text. See References.

(3) that palladium foils could be used to separate H_2 from H_2 , CO , CO_2 , H_2O mixtures at temperature exceeding $600^\circ C$. In addition, a systems study was performed to re-estimate the weight of a 4-man system based upon the data collected in achieving the above three objectives.

The use of series-connected batteries of small-area cells requires development of leak tight joints which do not interact with the electrode materials to shorten cell life. Preliminary screening of electrodes materials showed that both sintered Pt and sputtered $Pt-ZrO_2$ could be used to produce adherent, stable low-polarization anodes and that sintered Pt cathodes were tightly adherent with polarization voltages less than 0.34 volts.

Leak-tight, conductive bell-and-spigot joints containing 30-70% Pt and 30-70% Au by weight were developed which showed no visible interaction with sputtered $Pt-ZrO_2$ electrodes. Attempts to construct all-platinum joints were unsuccessful.

Based upon the results of the above screening tests, three five-cell batteries (OBS #8, #9, #10) were constructed with sputtered $Pt-ZrO_2$ anodes, sintered platinum cathodes and bell-and-spigot joints. The anodes of two of the batteries were overcoated with a sintered platinum layer to reduce the cell resistance. OBS #8 achieved 152 days of continuous operation and OBS #9 achieved 112 days. The testing of OBS # 10 was terminated after 77 days because of a crack in the end cap.

Operating at $920^\circ C$, OBS #8 required 5.9 volts at a current density of 200 ma/cm^2 to produce approximately 7.0 cc/min of oxygen at the start of the life test. This corresponds to a current efficiency of 0.90, a power efficiency of 0.62, and an overall power requirement of 0.34 watts/cc/min. After 100 days the driving voltage at the same current density had risen to 9.1 volts, the current efficiency had dropped to 0.68 and the power efficiency to 0.40.

The decline in current efficiency was due to increased shunt currents through the joint areas caused by the increased operating voltage rather than to an increase in the electronic conductivity of the electrolyte.

Examination of single cells and batteries which failed during the initial screening of electrode materials and joining techniques showed that failure occurred as a result of (1) evaporation of the anode, (2) disattachment of the anode, and (3) electrolyte cracking. Examination of the life tested batteries after failure confirmed these observations.

Preliminary evaluation of the catalysts for carbon deposition revealed that the addition of 3-8% H_2 to the CO feed resulted in increased rates of reaction and the elimination of catalyst decay for all catalysts employed.

A carbon deposition reactor was designed, constructed, and operated continuously for 101 days. The only catalyst employed was the wall of the reactor itself. Carbon was removed from the reactor by a manually-operated rotary scraper which required approximately 5 minutes per day for operation.

During the 100 day test an average conversion (moles of CO decomposed/mole of CO feed) was 0.62. The feed to the reactor was a mixture containing 75.8% CO, 19.8% CO_2 , and 4.4% H_2 at a flow rate of 0.614 g moles/hr; average operating temperature was 554°C; average carbon production was 42 grams/day.

The carbon collected was found to contain approximately 3.7% iron based upon chemical analysis. A computation based upon weight loss of the reactor (154.4 grams) divided by total carbon collected (4467 grams) gave a result of 3.5% in close agreement with the chemical analysis. The carbon collected was dry, containing less than 1% water, and free flowing. 90% of the carbon particles were greater than 48 mesh in size, and no clogging of filters was observed.

The palladium diffusion foil was found to have a permeability of $1.46 \text{ cm}^3 \text{ mm/cm}^2 \text{ atm}^{1/2}$ at 800°C with no observable carbon deposition occurring over a period of several days.

A mathematical analysis of an overall oxygen regeneration system including electrolysis battery, carbon deposition reactor, hydrogen diffusion cells, heat exchangers, and recirculation pump was performed. Based on the actual performance of OBS #8 and the continuous carbon deposition reactor, and the hydrogen studies discussed above, a

four-man oxygen regeneration system with 99% probability of achieving 100-day life was designed. Its physical weight was 121 pounds or 30 pounds/man. The total weight penalty including the physical weight, plus penalties of 340 pounds per KW of power and 0.01 lb per BTU/hr of heat loss, was 524 pounds or 131 pounds per man. Elikan, Archer, and Zahradnik⁽¹⁾ estimated 109 pounds per man exclusive of reliability considerations.

The analysis showed that a reduction in total equivalent weight exceeding 15% could be achieved by increasing the current efficiency from the present average value of 0.80 to 0.95 and by achievable improvement in cell life. Smaller but still significant improvements could be obtained by reducing cell polarization losses in the electrolysis battery and by developing better insulation materials.

2. SOLID ELECTROLYTE ELECTROLYSIS

The objective of this portion of the research was the development of a long-lived electrolysis battery for generating pure oxygen from mixtures containing CO_2 , H_2O , CO , and H_2 .

The development work was scheduled in two phases. In the first phase candidate electrode materials and application techniques, as well as candidate methods for joining cells into batteries, were screened. The electrodes were evaluated in single cell devices (SCD's) where interactions between dissimilar materials in the joint region could be avoided. In addition the separation of individual electrode effects was facilitated. Two different joining techniques, high platinum-bell-and-spigot joints and all-platinum butt-joints, were evaluated on the basis of initial gas-tightness and conductivity and the ability to maintain an electrically continuous interface between the joint and the oxygen side electrode.

On the basis of these preliminary tests, a decision was made to use sintered platinum cathodes, sputtered Pt-ZrO_2 anodes, and high-Pt-bell-and-spigot joints in the construction of three five cell batteries for evaluation in continuous 100-day tests. The initial performance and variation in power efficiency and current efficiency with time for the five cell batteries are reported in Section 2.4.

This subsection is preceded by a brief discussion of the principles of operation for solid electrolyte electrolysis (Section 2.1) and the presentation of test results for both successful and unsuccessful electrodes and joints in Sections 2.2 and 2.3.

2.1 Principles of Operation

A ceramic electrolyte -- $(\text{ZrO}_2)_{0.9}(\text{Y}_2\text{O}_3)_{0.1}$ -- is the basic component of the O_2 -production cell. At about 1000°C a thin sheet of

this material is a sieve through which oxygen readily passes; $O^{=}$ ions migrate through the crystal structure of the ceramic by activated diffusion. On the other hand, other gases such as N_2 , H_2 , H_2O , CO , and CO_2 will not penetrate the $(ZrO_2)_{0.9}(Y_2O_3)_{0.1}$; nor will electrons be conducted through it. The ceramic electrolyte conducts current only by the passage of $O^{=}$ ions.

In order to make an oxygen cell from a sheet of the ceramic electrolyte thin, porous electrodes are applied to both sides. (See Fig. 1.) On one electrode -- the cathode -- two molecules of CO_2 (or H_2O) are adsorbed from the surroundings. These molecules acquire four electrons from the platinum electrode, and the $O^{=}$ ions enter the crystal lattice of the electrolyte. Simultaneously, at the other electrode -- the anode -- two $O^{=}$ ions emerge from the electrolyte, give up four electrons to the electrode, and recombine to form O_2 .

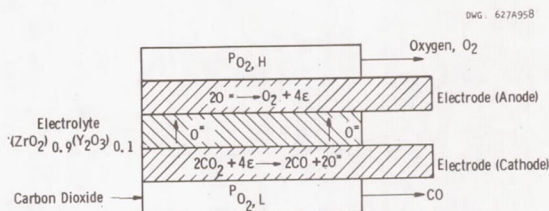


Fig. 1 - Schematic of solid-electrolyte oxygen production cell

In order to bring about the decomposition of the CO_2 (or H_2O), a certain minimum voltage, E_t , must be maintained between the electrodes of the cell. When current is passed between the electrodes in order to produce a flow of pure oxygen through the electrolyte, the required terminal voltage, V , increases above the minimum separation voltage, E_t . The increased voltage is required to overcome the resistance of the electrolyte to $O^{=}$ ion flow and of the electrodes to electron flow as well as the losses which occur due to irreversibilities in the electrode processes. The terminal voltage is then given by the general equation

$$V = E_t + IR + V_{p,a} + V_{p,c} \quad (4)$$

where

I = the current

R = total ionic plus electronic resistance of the cell

V_p = polarization voltages resulting from irreversibilities
in the electrode processes at the anode and cathode

E_t can be computed as a function of the composition of the CO_2 - CO - H_2O - H_2 mixture which is being decomposed and the cell temperature as described in Appendix A.

The current I required to produce an oxygen flow \dot{N}_O can be expressed as:

$$I = \frac{4F \dot{N}_O}{\epsilon} \quad (5)$$

where

F = Faraday number, 96,500 coulombs/g-mole

\dot{N}_O = oxygen flow rate, g-mole/second

ϵ = the current efficiency

For a perfect ionic conductor $\epsilon = 1$. However, in practice this value is reduced by electronic conductivity of the electrolyte, gas leakage, and electrical leaks (shunts) in the joint areas between cells.

The electrical resistance of each cylindrical cell in a series-connected battery of cells can be estimated by

$$R = \frac{\rho_b \delta_b}{\pi D L_e} + \frac{\rho_c}{2\delta_c} + \frac{\rho_a}{2\delta_a} \frac{L_e}{\pi D} + R_j + R_i \quad (6)$$

where

ρ_b = electrolyte resistivity, ohm-cm (see Fig. 2)

δ_b = electrolyte thickness, cm

ρ_c/δ_c = resistivity thickness quotient for the cell
cathode, ohm

ρ_a/δ_a = resistivity thickness quotient for the cell anode, ohm

L_e = mean distance travelled by the electronic current in the electrodes passing from the plus to the minus terminal of the cell, the effective cell length, cm

D = diameter of cell, cm

R_j = the joint resistance between one cell and the next, ohm

R_i = contact resistance at electrode-electrolyte interfaces, ohm

Experimentally-determined values of ρ_b as a function of temperature are shown on Fig. 2. The values of (ρ_c/δ_c) and (ρ_a/δ_a) are functions of the materials used as electrodes, the coating weight, and the coating porosity.

The values of V_p in Equation 1 must be obtained experimentally for each electrode. Application techniques have been developed as part of Westinghouse's effort in fuel cell research⁶ which produce platinum electrodes with low ρ/δ and low polarization. The principal shortcoming of batteries of cells constructed with these electrodes has been a relatively short life of 20-40 days.

The objective of the research in solid-electrolyte electrolysis carried out under this contract was to develop electrode materials (and application techniques) and cell joining techniques which would produce batteries of cells in which (1) ρ_c/δ_c , ρ_a/δ_a , R_j , and V_p are not only low at the outset, but stable for periods of 100 days and longer and (2) the current efficiency, ϵ , is high.

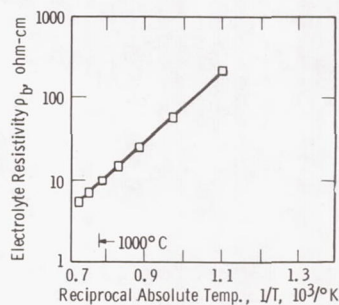


Fig. 2 - Electrolyte resistivity-temperature characteristics (Y_2O_3 stabilized ZrO_2)

2.2 Evaluation of Electrode Materials

Failure of cells of most long-lived solid electrolyte batteries constructed previous to this contract was found to result primarily from the development of a discontinuity at the electrode-joint interface on the oxygen side (anode) as illustrated in Fig. 3.

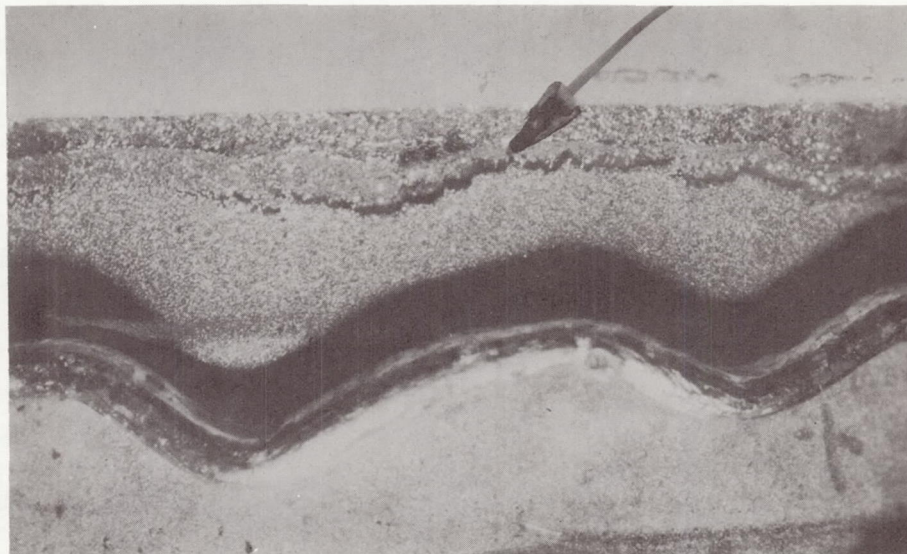


Fig. 3 - Photomicrograph of discontinuity between oxygen electrode and bell-and-spigot joint

This discontinuity is believed to be the result of a multistep process:

1. The gold-platinum alloy formed in this region has a lower melting point and, hence, a lower sintering point than pure platinum. Thus, sintering occurs more rapidly in this region than in the electrode proper.
2. As sintering proceeds, the resistance increases causing an increase in local temperature.
3. As the temperature rises, the rate of reaction of Pt with O_2 to form volatile PtO_2 increases.
4. Eventually all platinum volatilizes from this area.

In an attempt to correct this problem three approaches were pursued. (1) reduce the sinterability of the anode material, (2) reduce

the volatility of the anode material in oxygen, and (3) reduce in amount or eliminate the gold in the joint. In order to reduce the sinterability of platinum electrodes, the metal was dispersion-hardened by the co-deposition of ZrO_2 and Pt using a reactive sputtering process. A conductive oxide, In_2O_3 , was tried as an electrode material because of its low volatility in oxygen.

Single cell tests rather than battery tests were utilized in the initial evaluation of In_2O_3 and sputtered ZrO_2 as anode materials. In this way the measurement of individual electrode IR and polarizations was facilitated, and complications arising from the interactions of dissimilar materials in a joint region were avoided.

2.2.1 Cell Configuration and Test Apparatus

Fig. 4 shows a schematic drawing of the configuration adopted for testing various electrodes on single cells. Each cell is $1/2$ " long and has a mean diameter of about $1/2$ inch, giving an effective area of 5 cm^2 per cell. The three cells on the single electrolyte tube are called a single-cell-device (SCD).

The inside electrodes of the SCD's were of sintered platinum, $6\text{--}10 \text{ mg/cm}^2$ in weight, applied in three to five coatings and fired to $1100\text{--}1250^\circ\text{C}$ after each coating (see Appendix C.2). During cell operation the inside electrodes served as the cathodes at which the $\text{CO}_2 - \text{H}_2\text{O}$ mixture was decomposed.

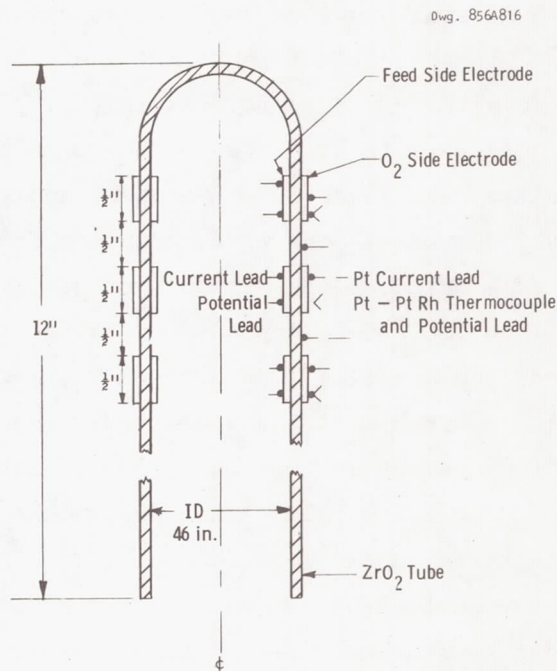


Fig. 4 - Schematic drawing of SCD device

The outside electrode materials included sintered platinum, sputtered Pt-ZrO₂, and vapor-deposited In₂O₃. The outer electrodes served as anodes at which the pure O₂ was produced.

In order to pass current through the cells and measure the potential and temperature, platinum lead wires and platinum-platinum rhodium thermocouples were placed on the outside electrodes as shown in Figure 4. Two electrolyte-potential probes made it possible to measure half-cell voltages. Contact to each inside electrode was maintained by a platinum screen which was held in place by packing a fibrous insulating material into the center of the tube. The inside lead wires and potential probes were attached to the platinum screens.

2.2.2 Performance of Sputtered Pt-ZrO₂ Anodes

The sputtered Pt-ZrO₂ tested in the single-cell devices were found to be tightly adherent. In no case was cell failure due to the detachment, sintering, or evaporation of the Pt-ZrO₂ electrode.*

The electrical performance of the anodic half cells with Pt-ZrO₂ electrodes is summarized in Table I. The apparent half cell resistances were in all cases higher than the computed half-cell electrolyte resistance of 0.075 ohms, and the polarizations ranged from 0.07 to 0.36 volts. The wide variation in polarizations noted with the sputtered electrodes was a result of poor control over the application method (see Table C-I, Appendix C) rather than an inherent deficiency of the electrode material. Subsequent tests with bell-and-spigot batteries employing sputtered Pt-ZrO₂ electrodes (see Section 2.4) showed considerable improvement in the production of reproducible electrodes.

The principal conclusions reached as a result of testing SCD's with sputtered anodes were:

1. Better control of the electrode composition and weight is required in order to produce low-resistance, low-polarization sputtered anodes.

* For the three SCD's discussed in this section, electrolyte cracking was the sole cause of failure.

TABLE I
INITIAL PERFORMANCE AT 1000°C OF CELLS
WITH SPUTTERED Pt-ZrO₂ ANODES

SCD No.	Cell No.	Overall All Performance		Pt-ZrO ₂ Electrode Performance	
		R (ohms)	Polarization at 400 ma/cm ² (volt) ^a	Apparent Ra (ohms)	Polarization at 400 ma/cm ² (volts) ^a
3	1	0.21 ^b	0.41 ^b	c	c
	2	0.26 ^b	0.49	0.126	0.20
	3	0.17 ^b	0.36 ^b	c	c
4	1	(0.18 ^b) 0.138	(0.38 ^b) 0.50	0.095	0.14
	2	(0.255 ^b) 0.235	(0.42 ^b) 0.52	0.15	0.22
	3	(0.17 ^b) 0.14	(0.26 ^b) 0.34	0.10	0.07
8	1	d	d	d	d
	2	0.43	0.60	0.40	0.36
	3	d	d	d	d

a CO₂ flow rate = 280 cc/min

b As determined by slope and intercept of V-I plot rather than by current interrupt.

c No meaningful estimate can be made due to erratic half cell voltage readings. Erratic behavior believed due to poor contact of the electrolyte probe.

d Data not repeatable, performance poor

2. Weight densities of 5-20 mg/cm² are superior to densities greater than 23 mg/cm² (Based upon fact that the heavily coated center cell of SCD #4 performed noticeably poorer than Cell 1 and Cell 3 of the same SCD.)
3. Coating weights of 1.5 mg/cm² (SCD #8) produce both high resistance and high polarization.

2.2.3 Performance of Sintered Platinum Anodes and Cathodes

2.2.3.1 Resistance and Polarization Measurements

SCD #9 was constructed with both the anode and cathode of each cell consisting of sintered platinum applied by the method described in Appendix C. 2. The average electrode weight was 9.1 mg/cm². The overall performance of two of its three cells, both initially and as a function of time, was the best of the single cells tested.

The total driving voltage, V, required as a function of current density for each of the three cells during the initial testing at 1000°C is plotted in Fig. 5. Both the uniformity of performance

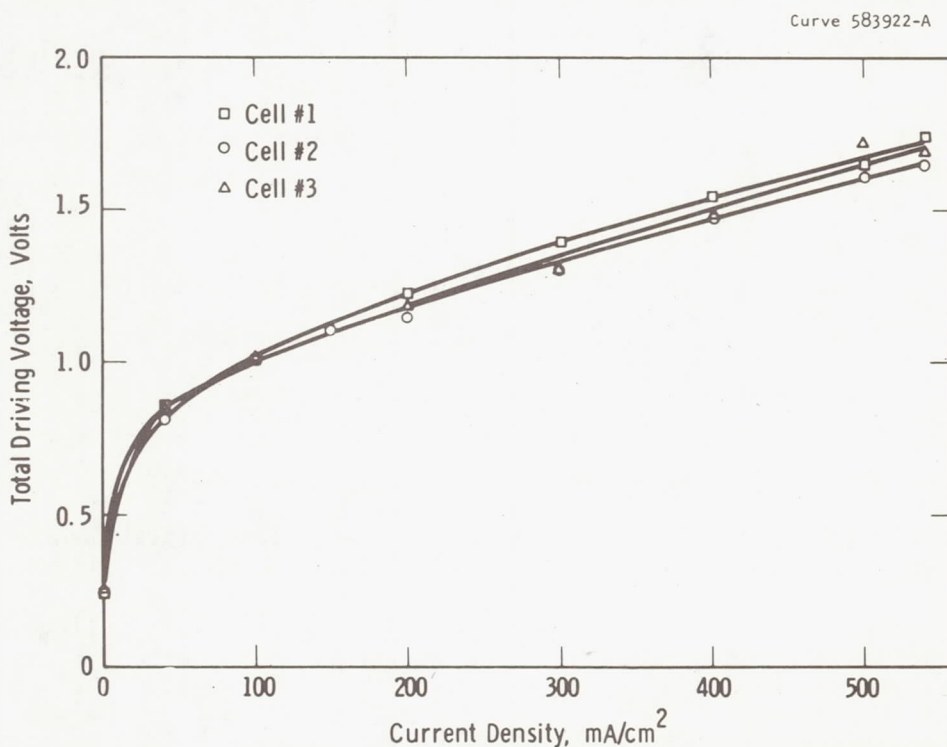


Fig. 5 - Total driving voltage as a function of current for cells of SCD #9 at 1000°C

from cell to cell and the low total driving voltage of less than 1.75 volts at 500 ma/cm² are evident.

In the initial testing period the voltage-current characteristics of each of the device's six half-cells were determined at 1000°C for direct comparison with sputtered Pt-ZrO₂ and In₂O₃ anodes and with previous sintered-Pt cathodes. The results are summarized in Table II.

TABLE II
INITIAL PERFORMANCE OF SCD #9 AT 1000°C

Cell No.	Overall Cell Performance		Anode Performance		Cathode Performance	
	R, ohms	V _p at 400 ma/cm ² , volts	R, ohms	V _{p,a} at 400 ma/cm ² , volts	R, ohms	V _{p,c} at 400 ma/cm ² , volts
1	0.188	0.38	0.147	0.17	0.041	0.21
2	0.147	0.39	0.06	0.11	0.087	0.28
3	0.179	0.38	0.109	0.11	0.070	0.27

The total cell resistances of 0.188, 0.147, and 0.179 ohms measured for the three cells indicate that contact losses were small (less than 0.04 ohms/cell) in comparison with the computed electrolyte resistance of 0.15 ohms. The apparent split between the two half cells is reasonable for Cells #2 and #3; there was essentially no contact loss in Cell #2, and most of the contact loss appeared at the anode of Cell #3. The apparent split in IR for Cell #1 cannot be explained by improper electrolyte probe location, since the apparent R for the cathode half cell is significantly lower than theoretical. Therefore, the most likely cause is improper register of the electrodes; i.e., the inside electrode extends further in the direction toward the electrolyte probe than does the outside electrode.

The anodic polarizations averaged 0.13 volts/cell at 400 ma/cm². Previous tests in which similar solid-electrolyte cells were operated as fuel cells showed average polarizations of 0.05 volts at the oxygen side electrode where O₂ was being adsorbed, rather than desorbed. A simple test, consisting of using the same electrode first for adsorbing O₂ and then desorbing O₂, should be carried out in the future to determine if a higher polarization is, in fact, associated with desorption of O₂ rather than with adsorption.

The cathodic polarizations at 400 ma/cm² of the sintered platinum electrodes of SCD #9 ranged from 0.21 volts to 0.28 volts with an average of 0.25 volts. This is seen to be significantly lower than the polarizations observed for SCD's 3, 4, and 8 (computed by difference from Table I) which ranged from 0.24 to 0.36 volts and averaged 0.29 volts.

2.2.3.2 Life Test of SCD #9

After initial characterization at 1000°C, the cells of SCD #9 were connected in parallel with one another, a driving voltage of 1.7 volts was placed across each, and the cells were used to decompose CO₂ at a temperature of 900°C. The current obtained from each cell as a function of time is shown in Fig. 6. A V-I curve for each cell taken a few hours before the start of the life test is seen in Fig. 7. The output of Cell #1 at 1.7 volts driving voltage decreased from 195 ma/cm² in Figure 7 to 84 ma/cm² at the start of the life test and to 48 ma/cm² after 13 days. Cell #1 was then placed on open circuit for the remainder of the life test. Cell #2 and Cell #3 operated at current densities of 330 and 290 ma/cm², respectively. These are about the values expected from their preliminary V-I curves (Fig. 7). After 102 days of continuous operation the current density (at 1.7 volts) decreased to 264 and 238 ma/cm² respectively.

The temperature was raised then to 1000°C; the current densities rose to 530 and 315 ma/cm² on Cells #2 and #3. After 7 days, however, the current began to fluctuate over a wide range and the life test was, therefore, terminated.

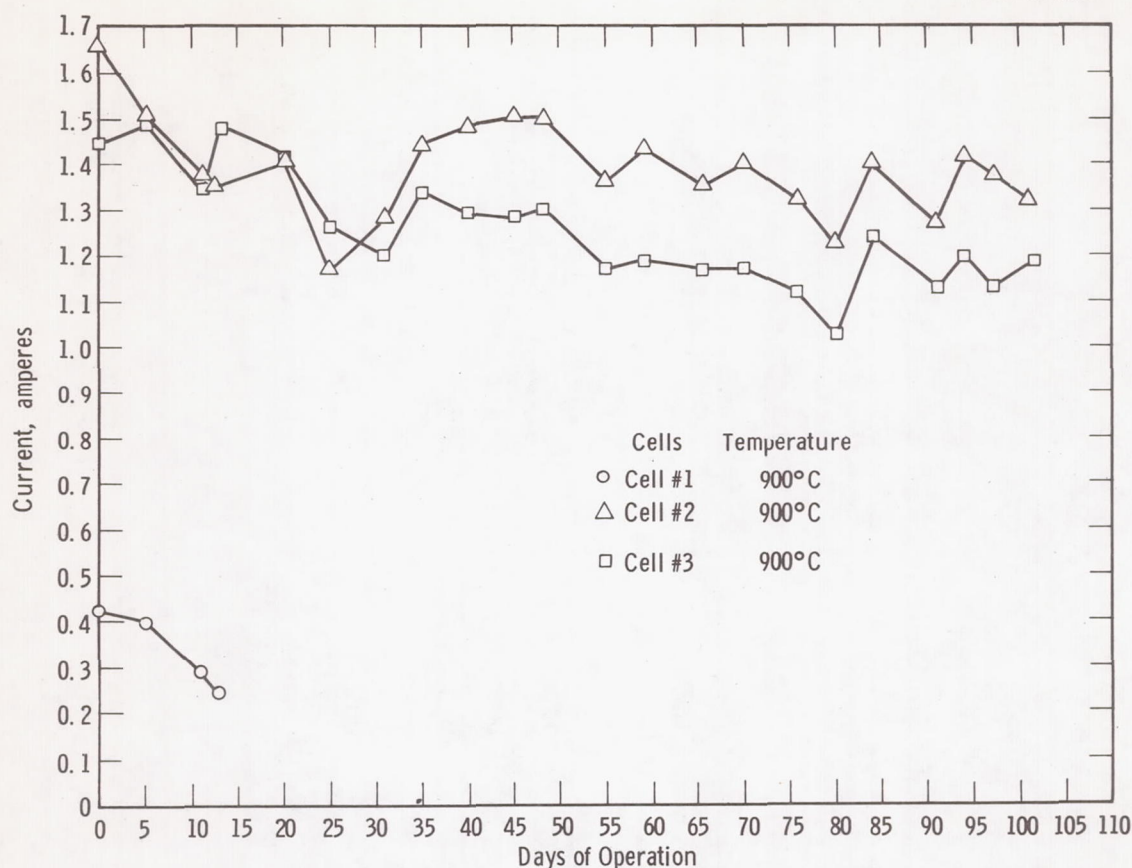


Fig. 6 - Life test performance of SCD #9 at driving voltage of 1.7 volts

Fig. 8 is a picture of SCD #9 at the conclusion of the 102 day test period. The electrolyte tube was broken in two places --just above the top contact wire of the middle cell (#2) and underneath the top contact wire on the bottom cell (#3). The break in the electrolyte of Cell #2 apparently occurred early in the testing; the inside of the crack

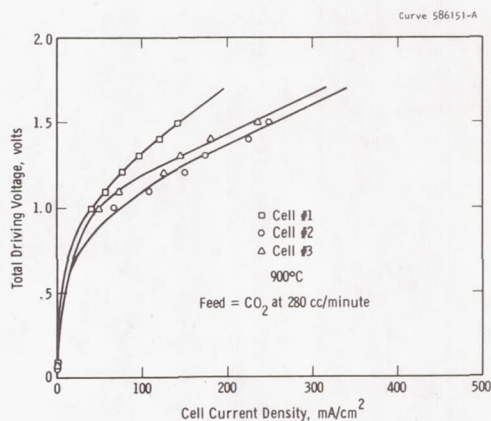


Fig. 7 - Cell current as a function of total driving voltage for cells of SCD #9 at 900°C just prior to start of life test

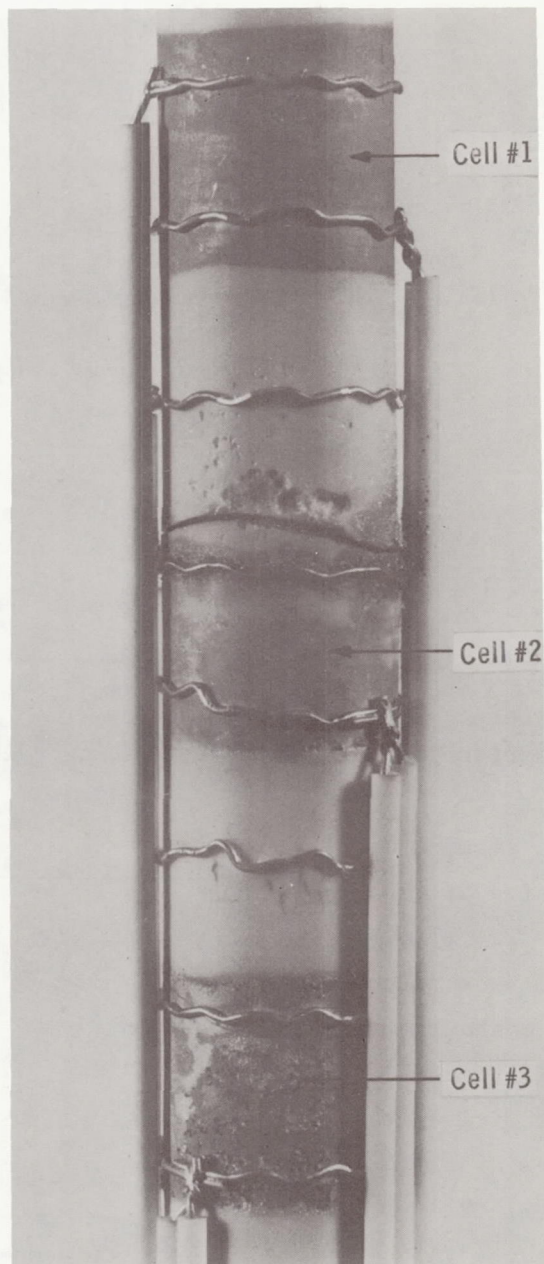


Fig. 8 - SCD #9 after 102 days of continuous testing at 900°C

was partially coated with platinum which apparently had evaporated from the surface of the bottom two cells and recondensed in the general vicinity of the top of the second cell.

A sharp contrast between the appearance of the electrodes of Cells 2 and 3, each operated for 109 days, and that of Cell 1, operated for 13 days is apparent in Fig. 8. The outside electrodes of the cells operated for 109 days have been partially removed by evaporation and peeling while the electrode of Cell #1 remains essentially as applied. If all the O_2 passing through the electrode were saturated with PtO_2 , the rate of weight loss for a current density of 300 ma/cm^2 at 900°C^a could be computed as follows:

$$\ln K = \ln p_{PtO_2}/p_{O_2} = \frac{-\Delta G}{RT} \quad (7)$$

$$p_{PtO_2} = p_{O_2} \exp (-\Delta G/RT) \quad (8)$$

At 900°C , $G = 38,180 \text{ cal/mole}^7$.

Therefore, if $p_{O_2} = 1 \text{ atm}$ at the electrode electrolyte interface

$$p_{PtO_2} = 1.0 e^{-(38180)/(1.98)(1173)} = 7.5 \times 10^{-8} \text{ atm}$$

And the weight loss expected is

$$\begin{aligned} & \frac{7.5 \times 10^{-8} \text{ moles of Pt}}{\text{mole of } O_2} \times \frac{1}{4} \frac{\text{moles } O_2}{(96,500) \text{ amp sec}} \times \frac{0.3 \text{ amp}}{\text{cm}} \\ & \times \frac{195 \text{ gm of Pt}}{\text{mole of Pt}} \times \frac{3600 \text{ sec}}{\text{hr}} \times 10^3 \frac{\text{mg}}{\text{gm}} \\ & = 4.08 \times 10^{-5} \frac{\text{mg Pt}}{\text{cm}^2 \text{ hr}} \end{aligned}$$

^a Assumes that interface temperature is equal to the average all temperature.

Thus, it is seen that in 109 days (2616 hours), the anticipated average weight loss from PtO_2 evaporation is only 0.11 mg/cm^2 .^a The almost complete evaporation of the 9.1 mg/cm^2 outside electrode from some areas of Cell #2, therefore, indicates considerable non-uniformity in either (1) the current density of the ions passing through the electrolyte, (2) the porosity of the platinum, (3) the coating weight of the platinum, or (4) the operating temperature.

Pitting of the electrolyte can be seen in the non-cell area between Cells 1 and 2 and, to a lesser extent, in the active area of Cell #3. The fact that the pitting occurs in a non-cell area as well as under the electrodes would appear to rule out theories which attribute the attack to electrode-electrolyte interactions. Not ruled out are those theories which attribute the pitting to pressure buildup within the electrolyte due to the decomposition of one or more of the compounds present in the electrolyte as trace contaminants.

2.2.4 Performance of In_2O_3 Anodes

The indium oxide electrodes tested exhibited higher polarizations at a given current density than did either sintered platinum or sputtered Pt-ZrO_2 electrodes. The polarization at 150 ma/cm^2 for a typical In_2O_3 anode exceeded 0.5 volts.

In addition, data from both SCD #1 and SCD #2 indicate that the integrity of the In_2O_3 film could not be maintained during operation; whether the destruction of the film was caused by electrochemical decomposition or by physical shattering as a result of the gas flow through the film could not be ascertained. However, the result of either is the same--no electrode remains after a few hours.

Table III shows the variation of ρ_a/δ_a , resistivity/thickness, during the operation of the In_2O_3 cell of SCD #2. The equation used for calculating ρ_a/δ_a from the experimental measurements is

$$\rho_a/\delta_a = V\pi D/Il \quad (9)$$

^aAdjusting this figure for 102 days at 917°C , and 7 days at 1027°C , the true operating conditions for Cell #2, increases the total computed loss to 0.21 mg/cm^2 .

where V, I = voltage and current tabulated
 D = cell diameter, 1.25 cm
 l = distance between potential probes, 0.5 cm

TABLE III

$\left(\frac{\rho_a}{\delta_a}\right)$ VS TIME OF OPERATION FOR
 THE In_2O_3 ELECTRODE OF SCD #2

Date	Time	Current, ma	Voltage, mv	ρ_a/δ_a ohms
8/11/67	11:35	100	8.8	0.692
8/11/67	11:37	200	17.2	0.676
8/11/67	12:35	100	4.4	0.346
8/11/67	12:35	200	6.6	0.259
8/11/67	2:10	200	300-255	11.8-10
8/11/67	2:10	300	400-320-360	10.5-9.7-9.4
8/11/67	2:10	400	480-440	9.4-8.7
8/11/67	2:20	200	220	8.6
8/11/67	2:20	300	320	8.4
8/11/67	3:45	300	350	9.2

The jump in ρ_a/δ_a from 0.259 to 11.8 ohms occurred at the exact same time that the cell behavior became erratic, indicating that a loss in continuity in the In_2O_3 electrode caused the fracture of this cell.

Fig. 9 illustrates another severe problem associated with the use of In_2O_3 electrodes-- H_2 or CO in the oxygen compartment reduces the

In_2O_3 to a lower, volatile oxide. The photograph shows the complete loss of electrode by evaporation which resulted after tube fracture.

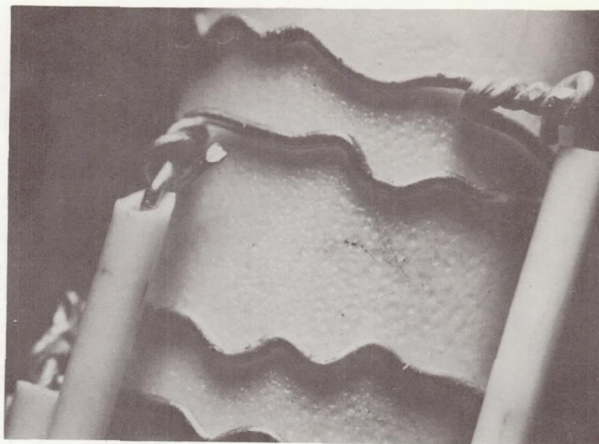


Fig. 9 - Bare electrolyte tube surface of $\text{In}_2\text{O}_3/\text{Pt}$ working cell after In_2O_3 had been reduced by hydrogen at approximately 1000°C . (5X magnification)

2.2.5 Conclusions Based Upon the Testing of Single-cell Devices

1. Both sintered Pt and sputtered Pt-ZrO_2 produce tightly adherent, stable electrodes suitable for use as the oxygen side electrode in multi-cell electrolysis batteries.
2. In_2O_3 has not yet performed well as an electrode material for electrolysis batteries because of high polarization, difficulty in keeping electrodes attached during operation, and instability in the presence of leaks.
3. Sintered platinum is an effective feed side electrode (cathode) material which is tightly adherent and normally yields less than 0.34 volts polarization.
4. Polarizations of 0.11 to 0.17 volts can be anticipated at the sintered platinum anode.
5. Better control over the weight and composition of the sputtered Pt-ZrO_2 electrode must be achieved in order to ascertain the polarizations obtainable with Pt-ZrO_2 electrodes. The best sputtered anode tested has a polarization of 0.07 volts at a current density of 400 ma/cm^2 .

6. Sintered Pt anodes of weight density 9.1 mg/cm^2 were operated continuously for 100 days at 900°C in the absence of gold. However, the rate of Pt evaporation did not appear to be uniform over the entire electrode area even in the absence of gold, and the rate of evaporation in some areas appeared to be as much as 80 times the computed average rate.
7. No reliable estimate of the life of sputtered Pt-ZrO₂ anodes can be made as a result of these tests. Each of the SCD's with Pt-ZrO₂ anodes failed due to electrolyte cracking in less than 40 days at which time the electrodes appeared to be in excellent condition.
8. Electrolyte pitting and cracking occurred in the cell and non-cell regions during the 109 day life test of SCD #9, indicating that electrolyte pitting is not a result of an electrode-electrolyte interaction.

2.3 Evaluation of Cell Joining Techniques

The construction of an efficient, low-weight solid electrolyte electrolysis device having long life requires the use of a large number of relatively small area cells connected in series. Thus, an effective technique for joining individual cells together must be developed. The joint must:

1. Provide a low resistance connection between the anode of one cell and the cathode of the next.
2. Serve as a gas-tight seal separating the partially reduced CO₂-H₂O mixture being electrolysed from the pure oxygen product. (Leakage results in a reduction of the current efficiency, ϵ , and produces localized hot spots which may increase the rate of battery deterioration.)
3. Withstand attack by either the oxygen or the feed gas at operating temperature.
4. Be compatible with both the anode and cathode materials so that reactions do not occur which will cause loss of electrode adherence, electrode sintering or an increase in the rate of electrode evaporation at either electrode joint interface and, thus, limit life.

5. Provide an electrical insulator which isolates the anode of one cell from the anode of adjacent cells, and does similarly for the cathodes. The joint must also discourage the formation of parasitic cells between the seal itself and adjacent cells. Shunt currents and parasitic cells also reduce ϵ .

Bell-and-spigot joints employing platinum-gold and platinum-nickel-gold brazing satisfied four of the five requirements^{6,8}, but were limited in life to less than 40 days by interaction between the electrode and joint on the oxygen side. Because of the lower melting point of Pt-Au alloys compared to platinum, increased sintering occurred at the interface and failure occurred by the mechanism described in Section 2.2.

The use of less gold in the conventional bell-and-spigot joint and the construction of all-platinum butt joints were investigated in this research as a means of extending battery life to the required 100 day minimum.

2.3.1 Tightness and Conductivity of High-platinum Bell-and-spigot Joints

A battery consists of a number of cylindrical cells, plus an end cap and base tube, joined together in series. A five-cell bell-and-spigot battery is shown in Fig. 10. The fabrication technique used to construct such a battery is outlined in Appendix D.1.

The primary difference between this procedure and those used previously was the care taken to obtain a tight fit before brazing and the use of 6 and 8 mil gold wires for brazing rather than a 10 mil wire or a 10 mil. plus a 6 mil as had been previous practice. With a 6 mil wire rather than a 10 mil, the amount of gold in the joint region is reduced by 64% (the gold plating thickness is extremely small), and the liquidus temperature is raised from about 1300°C to approximately 1500°C for the average alloy composition.

Prior to constructing three five-cell bell-and-spigot batteries specifically for life test, seven multi-cell bell-and-spigot batteries were constructed to determine whether tight, low resistance joints could be constructed with less gold than had been standard practice. The tests

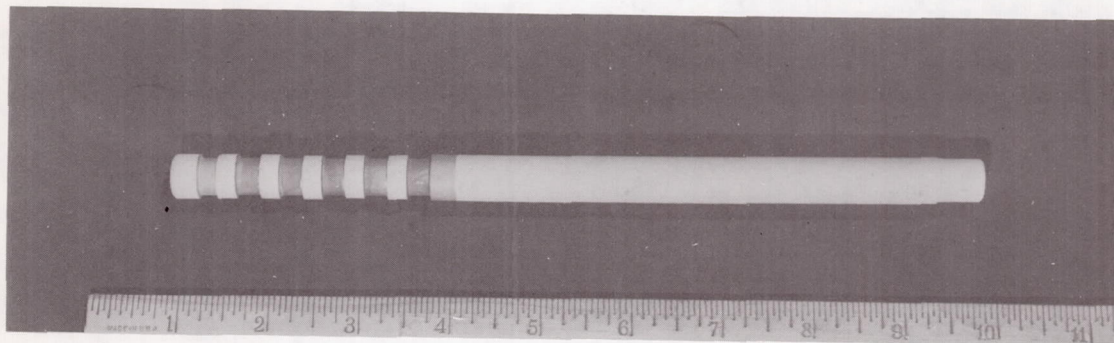


Fig. 10 - Five-cell electrolysis battery after construction

were also designed to yield data on the life of bell-and-spigot batteries (OBS) with sputtered anodes; however, electrolyte cracking^a prevented testing the joints to failure. The joint compositions and results of initial characterizations are summarized for five of the batteries in Table IV. (OBS #1 and OBS #4 were damaged during fabrication) To measure individual cell performance in a BS battery, potential probes are placed on each outside electrode; therefore, each voltage difference includes the potential drop across half of the

^aCracking was found to result from a combination of factors including a batch of electrolyte with poor mechanical properties, reduction of electrolyte caused by exceeding the decomposition voltage of ZrO_2 , and thermal stresses created by the sputtering process. Once the causes were identified, the cracking problem was markedly reduced by obtaining a new batch of electrolyte, by controlling the voltage at lower levels, and by a modification in the sputtering process.

TABLE IV
COMPOSITION, TIGHTNESS, AND CONDUCTIVITY
OF BELL-AND-SPIGOT JOINTS

Segment No.	W _o , mg	W _i , mg	M _o	W _{Au} , mg	% Au	Tightness *	R _m , ohms	R, ohms
OBS #2								
4-04	22	19	Pt	30	42	T	--	0.40
3-06	22	19	Pt	30	42	T	--	0.40
4-06	22	19	Pt	30	42	T	--	0.50
OBS #3								
0-22	20	7	P-z	15.5	37	TT	--	--
0-16	28	8	P-z	15.5	30	TT	--	--
0-13	40	10	P-z	15.5	23	TT	--	--
	8	10	P-z	15.5 + 6	54	ST	--	--
OBS #5								
0-32	5	14	P-z	15.5	45	T	0.19	--
0-37	5	11	P-z	15.5	49	T	0.17	0.25
0-38	5	11	P-z	15.5	49	T	0.12	0.44
0-35	4	14	P-z	15.5	48	T	0.10	0.20
0-33	5	13	P-z	15.5	48	T	0.20	0.35
	5	10	P-z	15.5	51	S	0.30	--
OBS #6								
0-69	10	13	P-z	15.5	40	TTT	0.2	--
0-79	14	11	P-z	15.5	38	TTT	0.3	--
0-78	15	12	P-z	15.5	37	TTT	0.2	--
0-68	14	12	P-z	15.5	37	TTT	0.1	--
0-77	14	13	P-z	15.5	37	TTT	0.2	--
	10	10	P-z	15.5 + 6	52	LLL	0.6	--
OBS #7								
0-73	15	14	P-z	24 + 6	51	SS	0.25	0.28
0-70	14	12	P-z	24 + 6	54	TT	0.06	0.21
0-72	14	15	P-z	24	45	TT	0.1	0.30
0-75	7	12	P-z	24	56	TT	0.2	0.20
0-76	15	13	P-z	24	46	TT	0.3	0.60
	14	13	P-z	15.5	37	TT	--	--

W_o = Weight of platinum in joint contributed by outside electrode
 W_i = Weight of platinum in joint contributed by inside electrode
 M_o = Material of outside electrode; Pt = sintered Pt, P-z = sputtered Pt-ZrO₂
 W_{Au} = weight of gold in joint
 % Au = % gold in joint
 T = tight joint
 S = small leak
 L = large leak
 R_m = approximate joint resistance measured by two probe ohmmeter
 R = measured total resistance from current intercept photos
 * The state of the joint after successive firings is indicated by the successive letters.

outside electrode of an adjacent cell; the IR, V_p , and E_t associated with the cell of primary concern; and the resistance of the joint between the two cells. Each joint in a BS battery is associated with the performance of a single cell (except for one joint which acts only to provide a gas-tight seal between the bottom cell and the base.) Column 1 of Table IV identifies the segment with which the resistance of each joint is associated. The next four columns identify the amount of platinum and gold in each joint and whether the outside electrode associated with the joint is sintered or sputtered. The percent gold (column 6) is defined by:

$$\% \text{ Au} = \frac{W_{\text{Au}}}{W_o + W_i + W_{\text{Au}}} \quad (10)$$

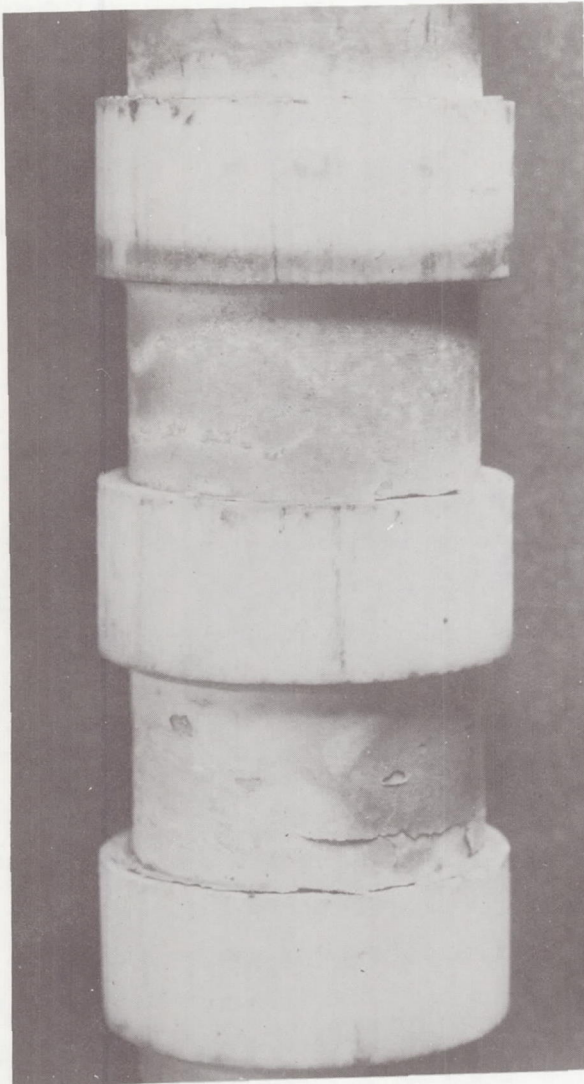
neglecting the gold and platinum added by the electroplating process. Under "tightness", the permeability to gases after each firing is indicated. R_m is not the true joint resistance because each probe has only a point contact; the true joint resistance is between 1/4 and 1/2 of R_m .

Based on the results shown in the table, the following conclusions can be drawn:

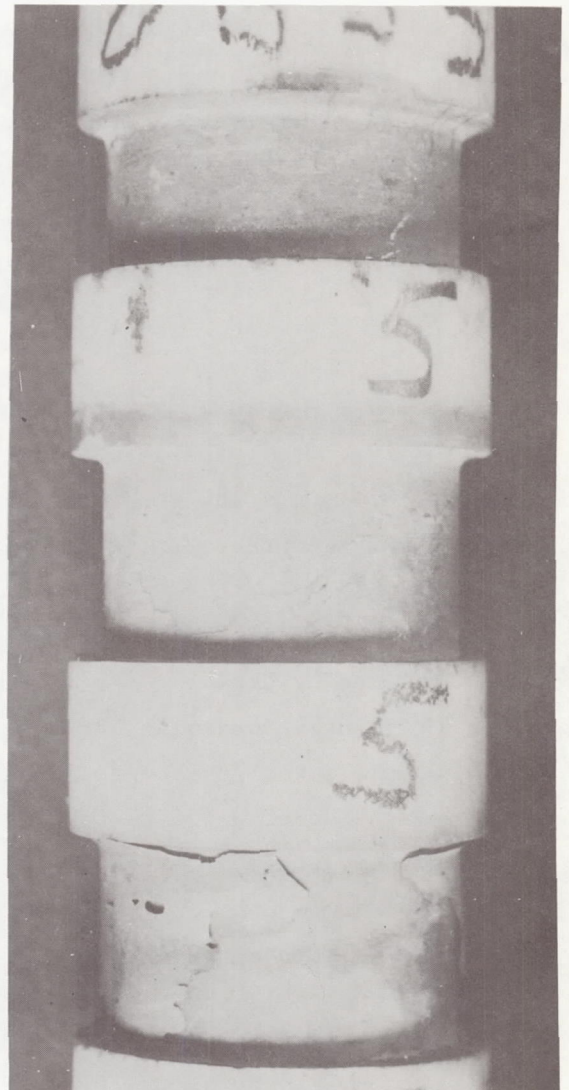
1. For joints containing between 23% and 56% Au, neither the tightness nor the joint resistance appears to be a function of the composition.
2. Over 80% of the joints fabricated were gas tight. Failure to obtain any completely gas-tight 5-cell batteries was due to the uniform temperature zone of the furnace being too short. (Note that all leakage joints are either at the top or the bottom of the batteries.)
3. The total cell ohmic losses, R do not appear to be strongly dependent upon R_m , although a weak correlation can be seen.

Thorough examination of each battery after failure showed that in all cases the outside electrode-joint interface was still continuous at the time of failure.

Pictures taken of OBS #5 after 86 days of continuous testing (Fig. 11) show that continuity was still maintained at the electrode-joint interface (Fig. 11a). Failure of the overall battery occurred because of an accidental loss in furnace power. Prior to this time the performance of three of the battery's five cells had deteriorated badly because of the severe peeling of the outside electrode seen in Fig. 11b.



a



b

Fig. 11 - Pictures of OBS #5 after failure

2.3.2 All Platinum Butt Joints

Butt joint (BJ) batteries are constructed from cylindrical $(\text{ZrO}_2)_{0.9} (\text{Y}_2\text{O}_3)_{0.1}$ segments placed end to end and joined with platinum. The steps followed during construction are outlined in Appendix D.2.

Seven attempts to construct BJ batteries were made. In the first four a platinum shim 0.002" thick was placed between segments, bringing the total platinum in the joint area to approximately 120 mg/cm^2 ; the segments had a wall thickness of 0.060 inches. Each of these was completely tight after first firing. However, in subsequent air firings, the electrolyte adjacent to the joint cracked in several segments. This problem, caused by the difference in thermal expansion between the Pt and the electrolyte, was eliminated in subsequent batteries by removing the shim from the joint, thus reducing the amount of Pt to $15\text{--}25 \text{ mg/cm}^2$. However, this amount of platinum was not sufficient to provide tight, long-lived joints. In subsequent thermal cycling the joints developed leaks and eventually fell apart. Experimentation should be carried out to see if an intermediate Pt weight, between 25 mg/cm^2 and 120 mg/cm^2 , can be found where both electrolyte cracking and joint failure are eliminated.

2.4 Performance of Multi-cell Batteries

Three five-cell batteries were constructed for the purpose of obtaining meaningful data on the power requirements and life of multi-cell devices similar to those which will be used in actual life support systems. Each of the three batteries was life tested at different conditions, and the current efficiency and power efficiency as a function of time were determined.

This section discusses the results of the life testing of OBS #8, OBS #9, and OBS #10. The discussion includes the initial battery performance and variation in performance with time during the life test.

2.4.1 Initial Performance Characterization

2.4.1.1 Overall Battery Performance--OBS #8

The total voltage, V_T , required at 1000°C to drive OBS #8 is shown as a function of the current density in Fig. 12. Since each cell has approximately 2 cm^2 of active area (see Fig. D1), the total area is 10 cm^2 , and the total oxygen produced is ten times the current density times $3.85 \text{ cm}^3/\text{ampere-min}$, as is shown on the upper axis in the figure. The theoretical minimum voltage, E_t , computed from the feed gas flow and composition by the methods of Appendix A are shown on the same figure. From the difference in the slope of the two curves the total battery resistance can be computed as (see Fig. B1):

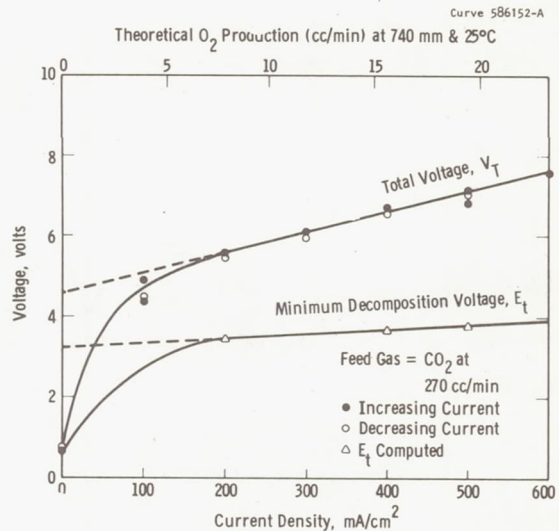


Fig. 12 - Overall voltage required as a function of current density for OBS #8 at 1000°C

$$R = \left[\frac{(7.15 - 4.65) \text{ volt}}{0.5 \text{ amp/cm}^2} - \frac{(3.75 - 3.25) \text{ volt}}{0.5 \text{ amp/cm}^2} \right] / 2 \text{ cm}^2/\text{cell}$$

$$= 2.0 \text{ ohm}$$

and the maximum polarization is: $(4.65 - 3.25) \text{ volts} = 1.4 \text{ volts}$.

From similar plots at 920°C (Fig. 13), the battery resistance is computed to be 2.4 ohms and the polarization, 1.1 volts.

Additional information on the total resistance, polarization, and driving voltage are shown in Table V, where the results of current interrupt tests at the two temperatures are compared with the values computed from Fig. 12 and 13. Note that the results obtained from the two methods agree closely except in the case of battery resistance (and V_T ,

in the case of 920°C*). The precision of the resistance computation is poor in both methods. In the current interrupt method, the result can be altered by the oscilloscope beam intensity, the shutter speed of the camera, the trace speed (cm/milliseconds), and by the voltage scale used. As was just shown above, R is computed from the V - I curves by taking the difference of two slopes. Averaging the results of the two methods, it appears that the total resistance is 1.8 ohms (or 0.36 ohms/cell) at 1000°C and 2.6 ohms (or 0.52 ohms/cell) at 920°C. The computed ionic resistance of the electrolyte at these temperatures (using Figs. 2 and D1) is 0.21 ohms/cell at 1000°C and

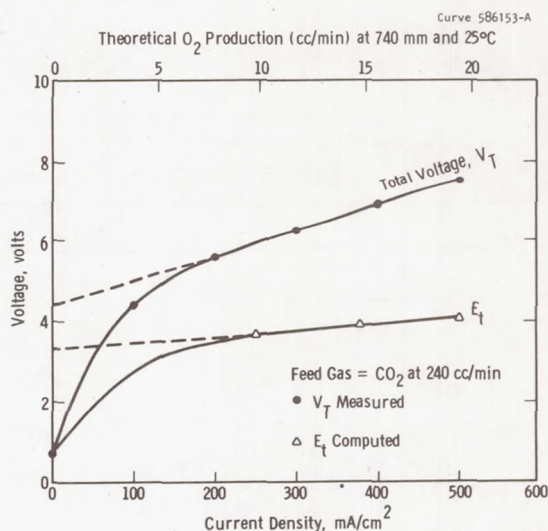


Fig. 13 - Overall voltage required for OBS #8 at 920°C

* Difference in V_T probably indicates that voltmeter used for Fig. 12 and 13 was slightly out of calibration in one of the two cases.

TABLE V
COMPARISON OF CURVE-COMPUTED CELL
PARAMETERS VS CURRENT INTERRUPT PHOTO-COMPUTED
PARAMETERS FOR OBS #8 AT 0.4 AMPS

	Curve	Photos	Theoretical
@ 1000°C			
R (ohms)	2.0	1.6	--
V _p (volts)	1.4	1.5 [‡]	--
E _t (volts)	3.45	3.46	3.45
V _T (volts)	5.6	5.6	--
@ 920°C			
R	2.4	2.8	--
V _p	1.1	1.2 [‡]	--
E _t	3.55	3.58	3.55
V _T	5.6	5.9	--

[‡] Based on assuming that E_t decays linearly
during first 160 milliseconds

0.36 ohms/cell at 920°C, thus, the sum of the joint resistance, electronic resistance of the electrodes, and the resistance of the electrode-electrolyte interface is approximately 0.16 ohms/cell. Based upon the platinum thickness in the electrodes, the electrode resistance can be computed as 0.08 ohms/cell. The electrode-electrolyte interface resistance can be estimated at 0.02 and 0.03 ohms at 1000°C and 920°C, respectively (see Section 2.2.3.1). Thus, on a per cell basis for OBS #8:

	<u>@ 920°C</u>	<u>@1000°C</u>
R_b	0.36	0.21
R_e	0.08	0.08
R_j	0.05	0.05
$R_{\text{interface}}$	0.03	0.02
R	0.52	0.36

2.4.1.2 Initial Performance--OBS #9 and OBS #10

Performance curves for OBS #9 at two temperatures for several feed gas compositions and for OBS #10 at 1000°C are shown in Figs. 14 and 15 respectively.

When operated on CO_2 at 1000°C, the performance of OBS #9 is seen to be essentially identical to that of OBS #8. At 900°C, however, its apparent resistance is 3.8 ohms (0.76 ohms/cell) compared to 2.6 ohms for OBS #8. Approximately 1/3 of the additional resistance can be attributed to the difference in temperature (920°C for OBS #8) but no explanation of the remaining 0.16 ohms/cell is apparent.

The higher resistance and polarizations of OBS #10 can be attributed in part to the fact that an all-sputtered electrode was used which had a very high ZrO_2 content, thus reducing its conductivity.

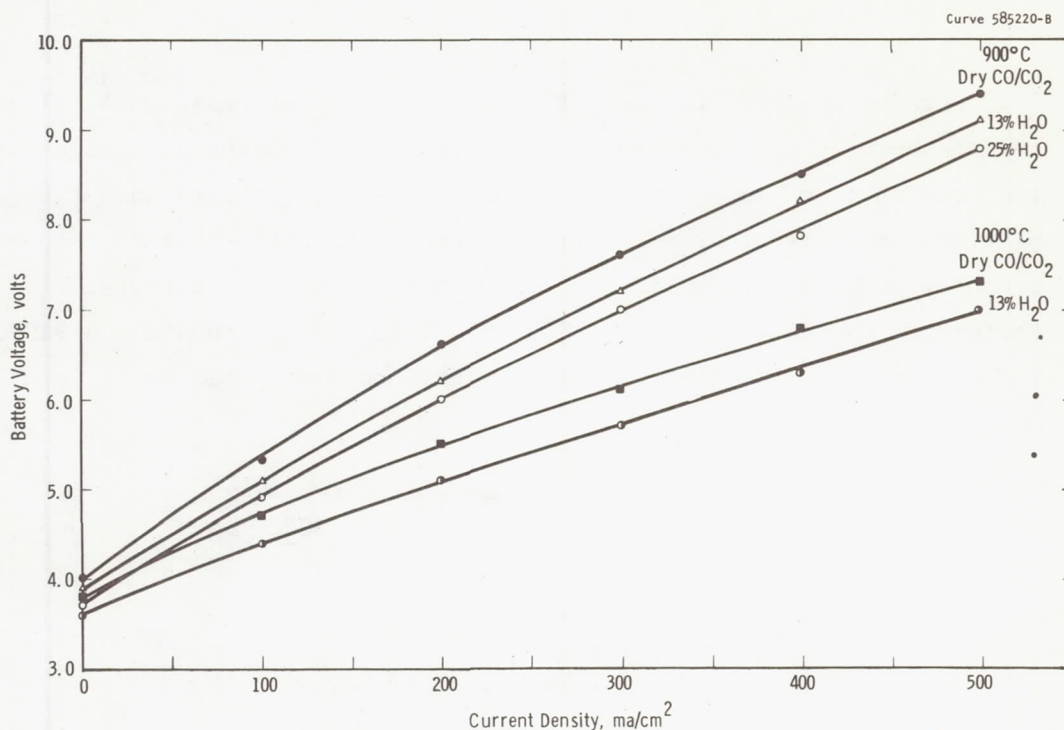


Fig. 14 - Total battery voltage vs current-density
OBS #9

2.4.1.3 Individual Cell Performance

The uniformity of cell performance achieved in OBS #8 is illustrated by the current interrupt photos in Fig. 16. At 1000°C the apparent individual cell resistances varied from 0.30 to 0.35 ohms and the polarizations at 0.4 amperes from 0.25 to 0.33 volts. At 920°C, the variation in polarization is from 0.18 to 0.34 volts while the resistances once again had a total spread of approximately 0.05 ohms.

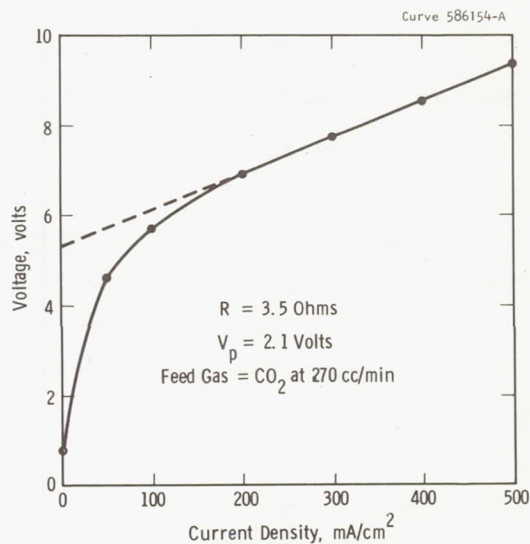


Fig. 15 - Total driving voltage vs current density for OBS #10 at 1000°C

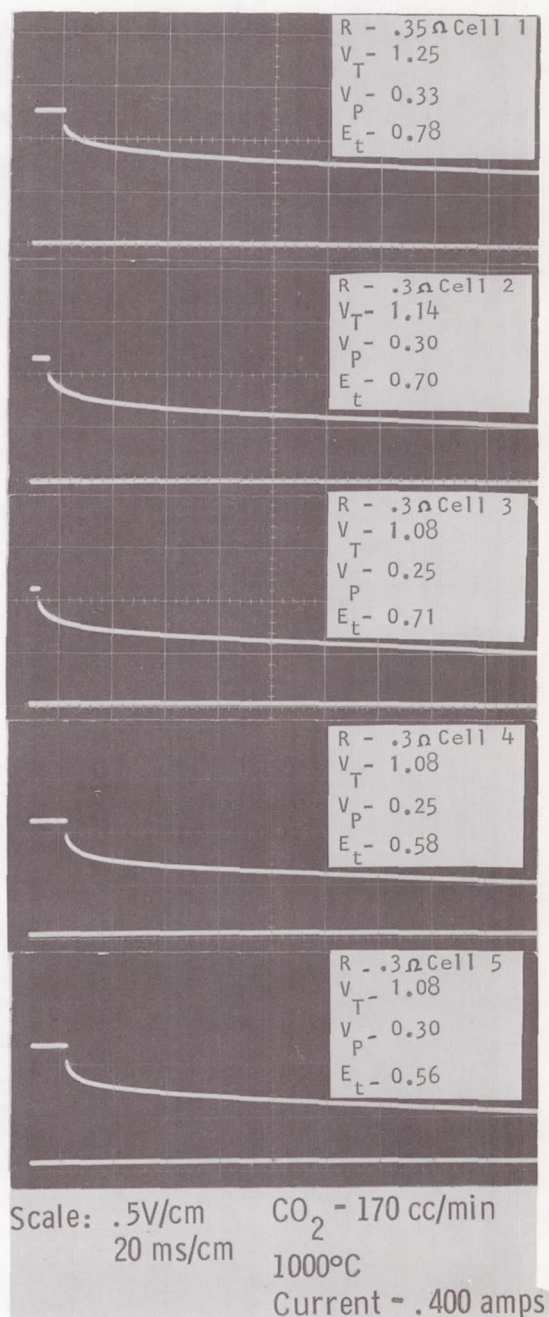
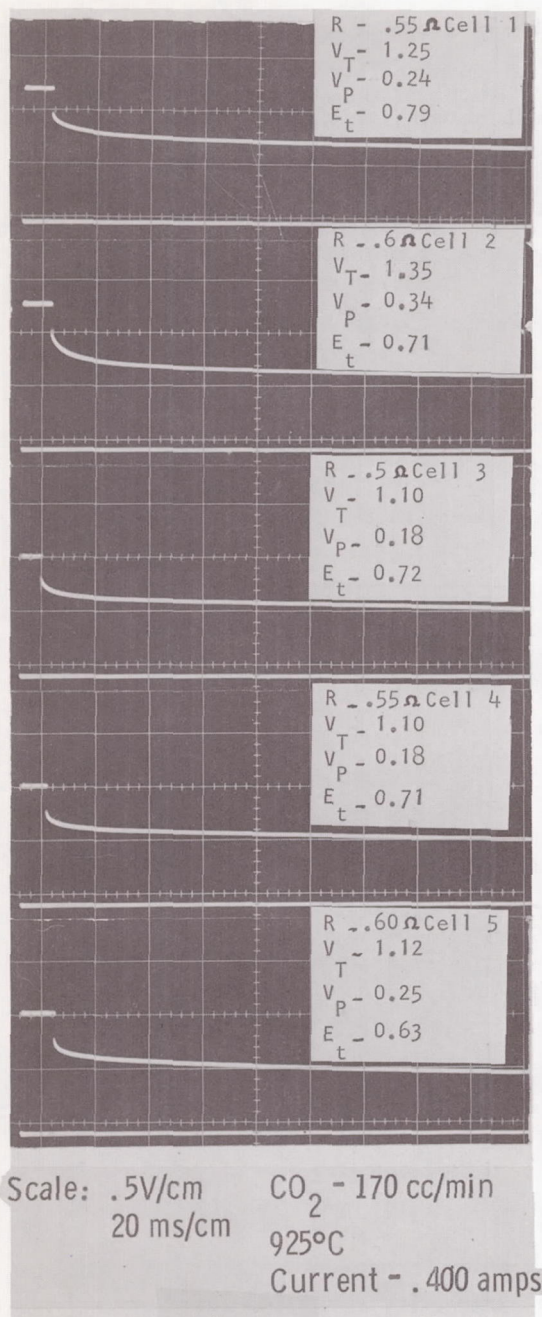


Fig. 16 - Current interrupt pictures of OBS #8

Similar uniformity was not achieved in OBS #10 (see Fig. 17). Wide variations in resistance were noted during the initial characterization and throughout its life test, although the polarizations from cell to cell varied only from 0.29 to 0.42 volts. The fact that cells #1 and 3, the two with the lowest % Pt in the anode, also have the highest resistances is further evidence that high ZrO_2 percentages cause poor cell performance.

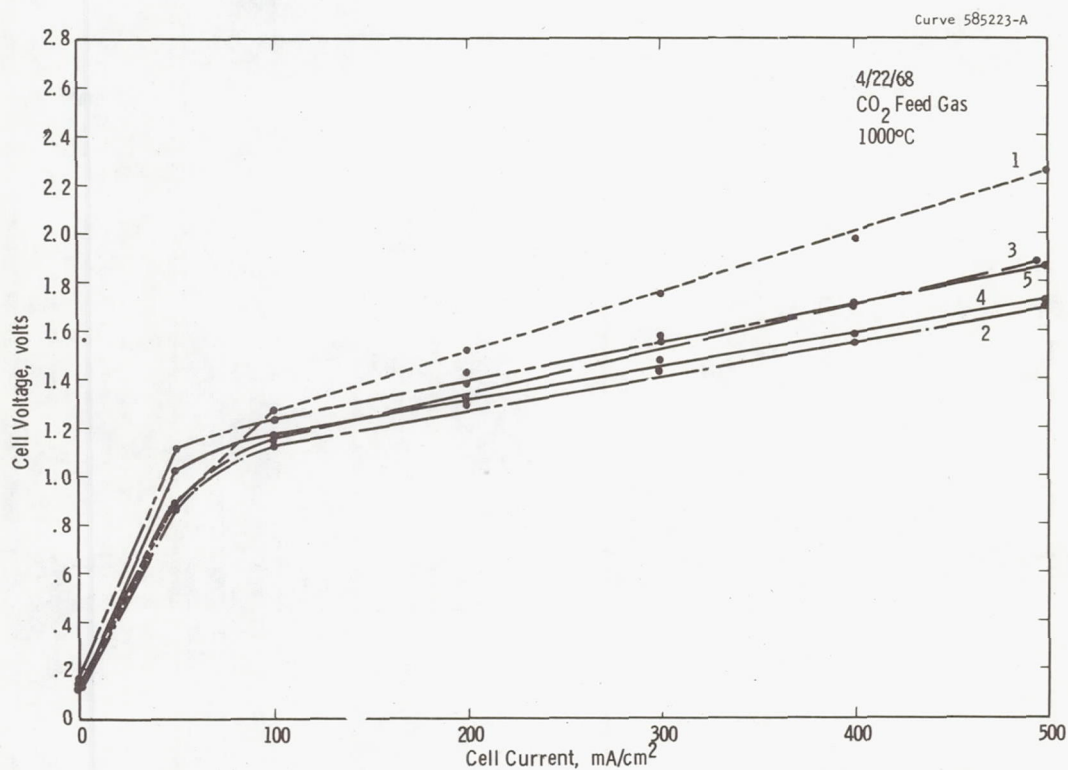


Fig. 17 - V-I curves for individual cells of OBS #10 during initial characterization

2.4.1.4 Power Efficiencies as a Function of Current Density

The power efficiency, defined by

$$E_p = E_t/V_T \quad (11)$$

can be determined readily as a function of current density from Figs. 12 and 13. The initial power efficiencies measured for the life-tested batteries are listed as a function of current density in Table VI.

TABLE VI

INITIAL POWER EFFICIENCY OF LIFE TESTED BATTERIES

Current Density	Power Efficiency (E_t/V_T)			
ma/cm ²	OBS #8		OBS #9*	OBS #10
	@ 920°C	@ 1000°C	@ 1000°C	@ 1000°C
200	0.616	0.616	0.635	0.550
300	0.608	0.582	0.585	0.507
400	0.571	0.556	0.545	0.475
500	0.540	0.536	0.520	0.445

*Dry CO/CO₂ (20/80)

2.4.1.5 Effect of Feed Gas Composition

The addition of water vapor to the CO₂ feed was found to reduce the driving voltages substantially at both 900°C and 1000°C. The addition of 13% H₂O lowered the average driving voltage by 0.08 volts/cell while the addition of 25% lowered it by 0.13 volts/cell (as illustrated in Fig. 14, page 34).

2.4.2 Life Test Results

2.4.2.1 OBS #8

OBS #8 was operated 24 hours a day, seven days a week for 152 days. The life test was continuous except for a 5-1/2 hour maintenance shutdown, during which time a new oxygen collection tube was installed to permit the measurement of current efficiencies. The cells were examined during this shutdown, and all electrodes were found to be tightly adherent.

The driving voltage required to maintain a current density of 200 ma/cm^2 at 920°C through each of the battery's five cells is shown as a function of time in Fig. 18. During the first 30 days of the test, very little change occurred, although a slight decrease in the driving voltage for the first cell can be noted from days 12-19 and a gradual increase in the voltage for cell #3 began on the 16th day. Over the weekend between the 30th and 33rd days the driving voltage for cell #3 increased above 2.5 volts. Because the increased voltage was found to be due to increased resistance rather than increased polarization, cell #3 was allowed to continue operation until the 41st day at which time the maintenance shutdown occurred. Cell #3 was shunted externally after examination during the shutdown showed a discontinuity developing at the electrode joint interface.

Cell #2 was shunted after the 70th day when its voltage reached 2.97 volts. Cell #4 showed a rapid decay in performance after the 90th day, but was allowed to remain in the circuit. When its performance stabilized after four days at 2.88 volts, the shunts on cells #2 and #3 were removed, and all five of the battery's cells were functioning on the 100th day. The power efficiency, however, had dropped from 0.616 to 0.37 at this time.

A massive leak was found in the system on 152nd day, and the life test was terminated. The power efficiency at just prior to shutdown had fallen to 0.275.

The cause of increased driving force requirements for cells #2, #3, and #4 was increased cell resistance, as is clearly shown by

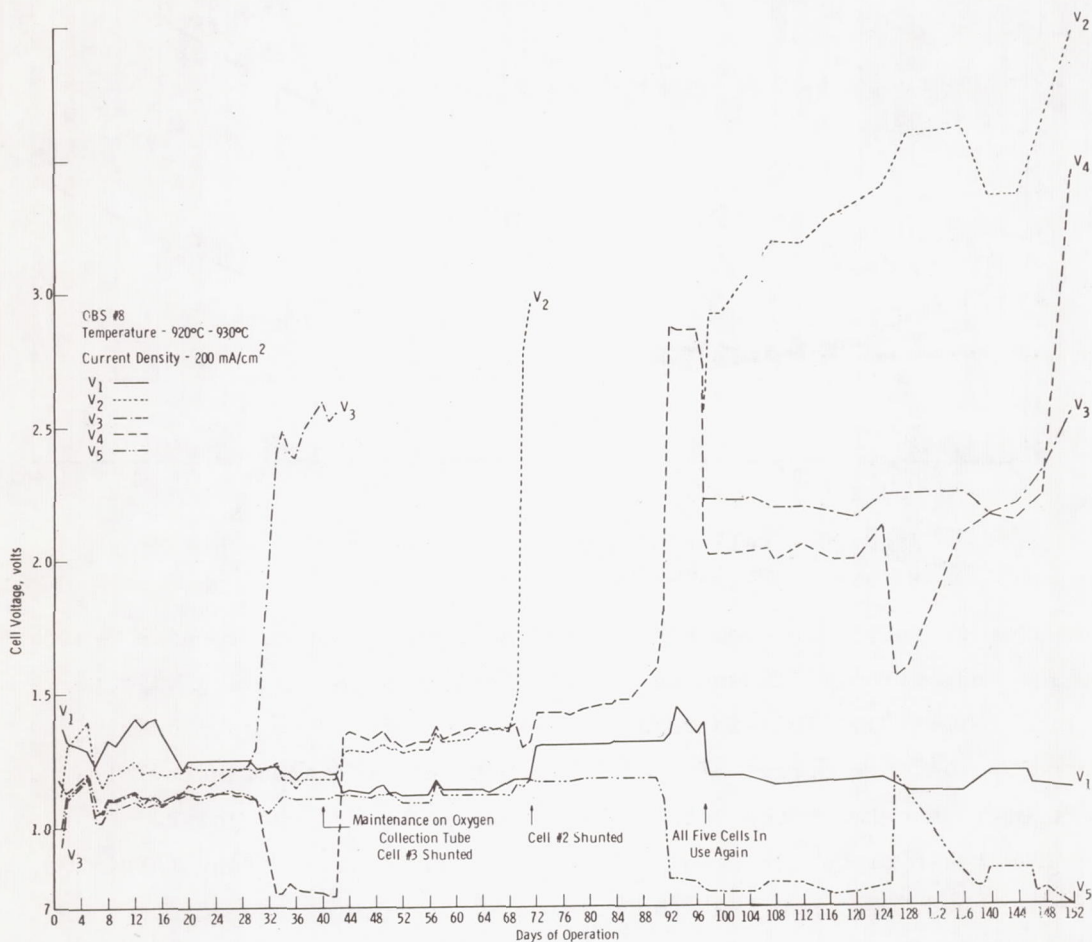


Fig. 18—Performance of the five cells of OBS #8 during life tests

Fig. 18 - Performance of the five cells of OBS #8 during life tests

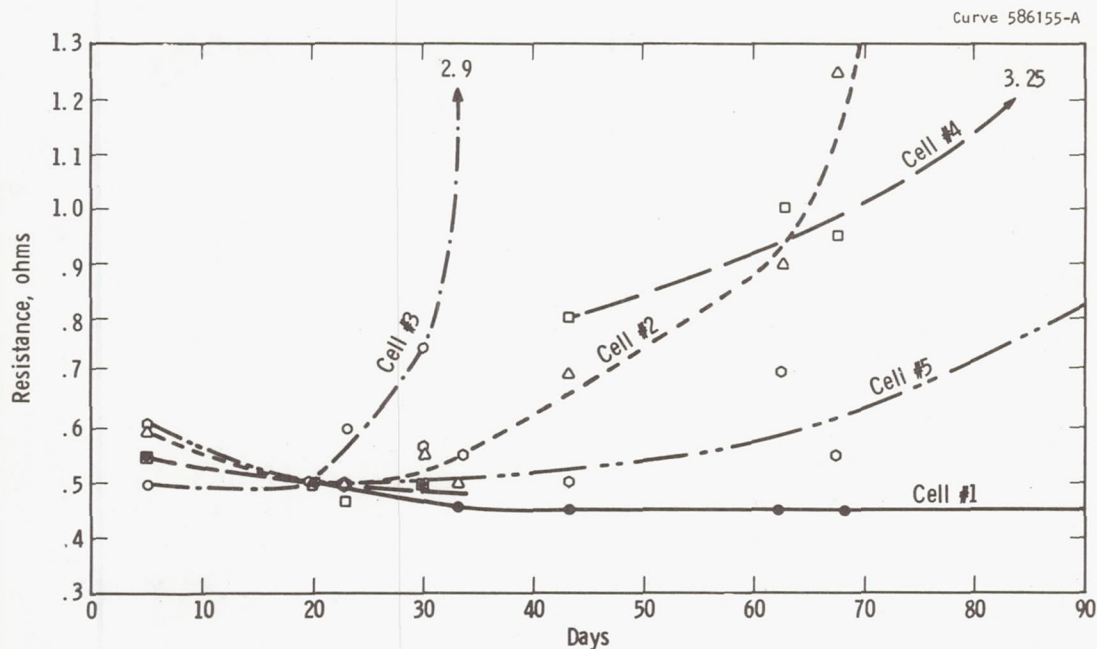
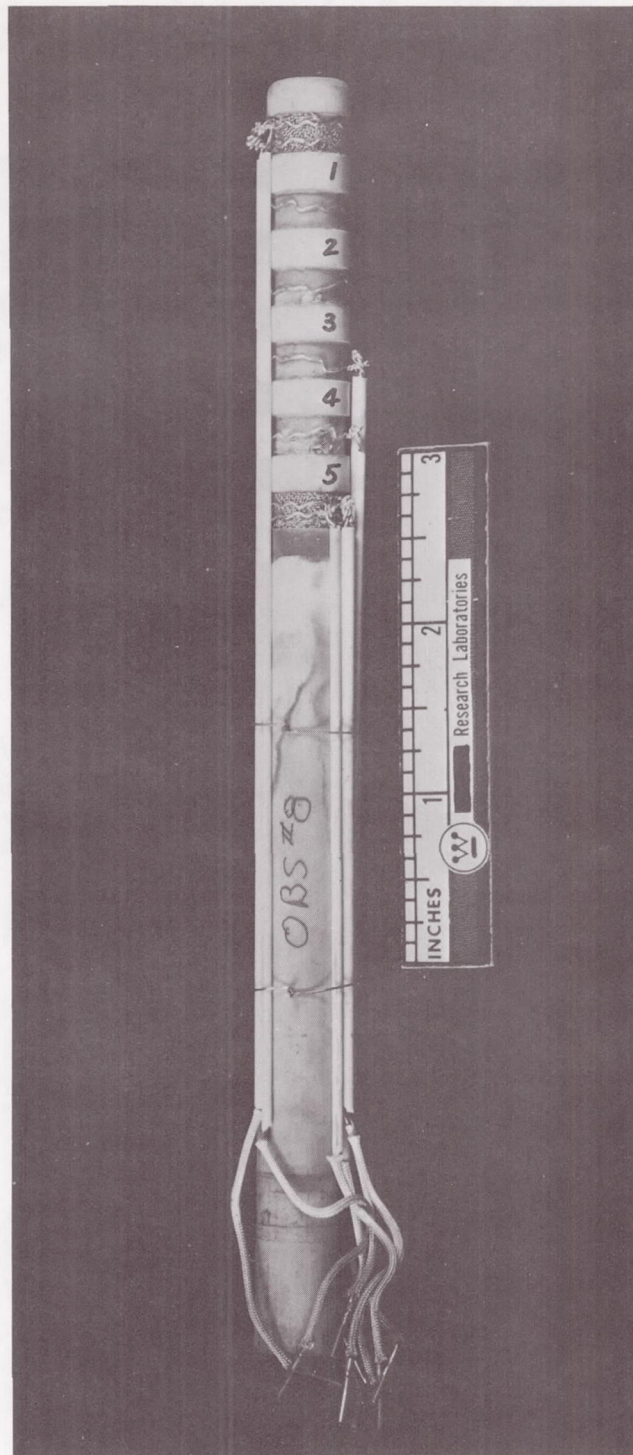


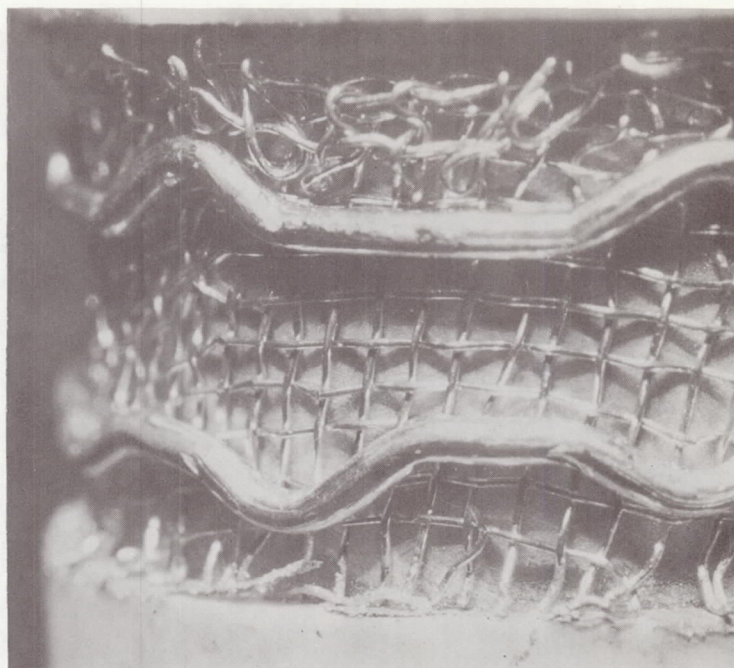
Fig. 19 - Cell resistance of OBS #8 at 920° vs time

Fig. 19. In fact, measurements of cell resistance appear to give a much earlier indication of impending failure than does the driving voltage vs time (Fig. 18). This increased resistance appears to have been caused by the development of a high resistance (or discontinuity) in the electrode between the outside electrode probe and the joint. Pictures taken of OBS #8 after 152 days of continuous testing (Fig. 20a, 20b, 20c, and 20d) show that the outside electrodes at the joints between cell #1, and #2, #2 and #3, #3 and #4 have been partially removed by evaporation of Pt. Close examination reveals cracked electrolyte between cell #1 and cell #2, and under the screen on the bottom cell #5 which caused the total failure of battery. The outside electrode of cell #4 was peeled off very badly at the time of failure, and this was most likely the cause of the trend of increasing cell resistance of cell #5 in Fig. 19.

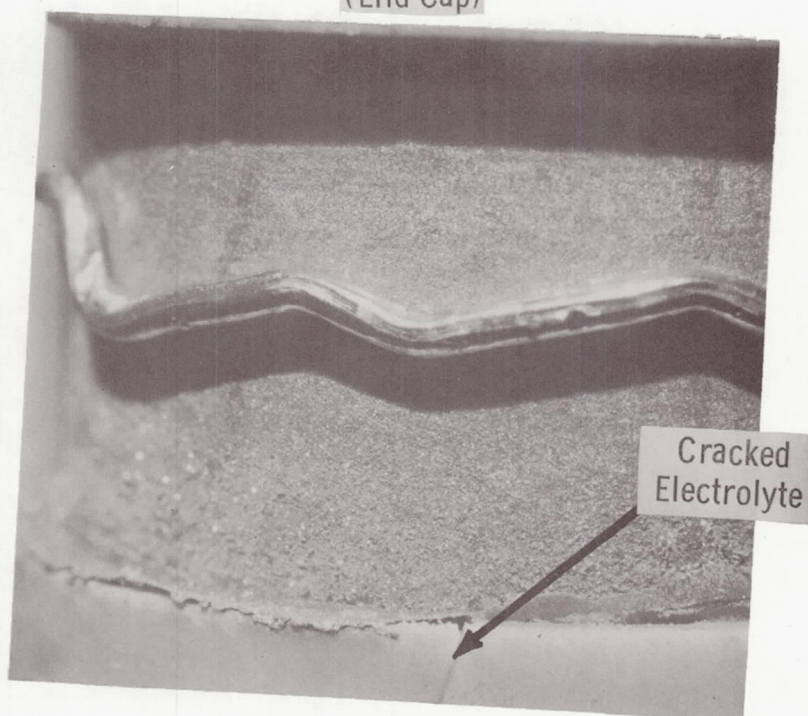


60163 5 CELL BATTERY ZrO_2 ELECTRODE OBS #8

Fig. 20a - Picture of OBS #8 after failure

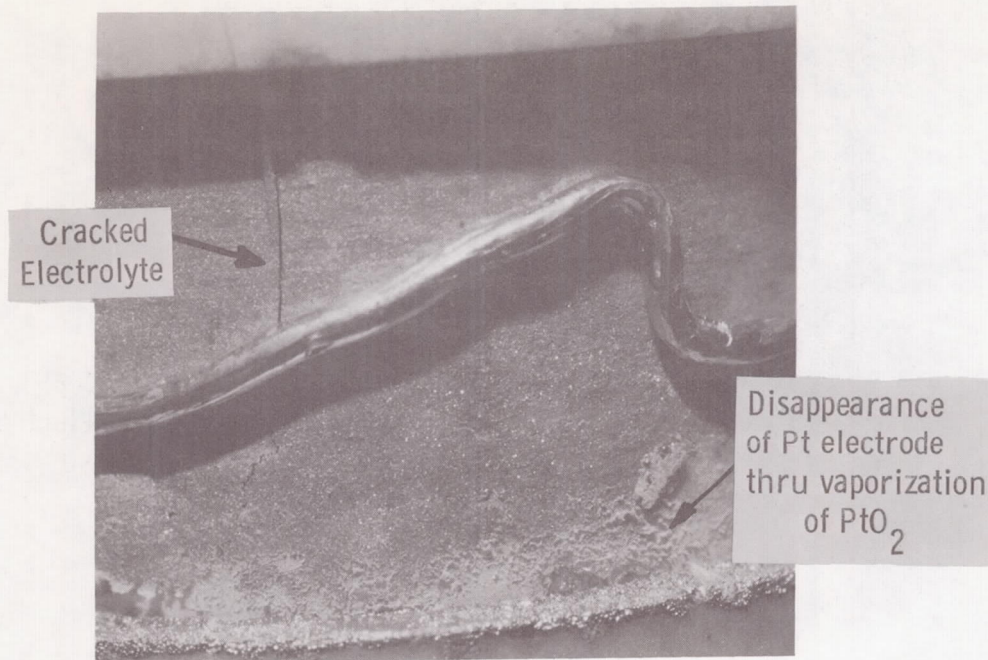


(End Cap)

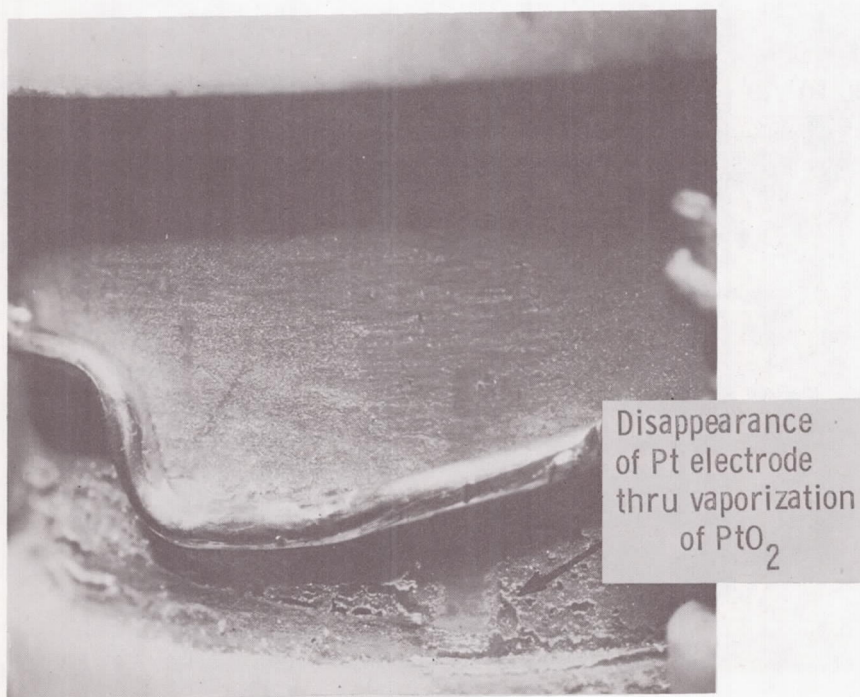


(Cell #1)

Fig. 20b - Pictures of individual cells of OBS #8 after failure



(Cell #2)



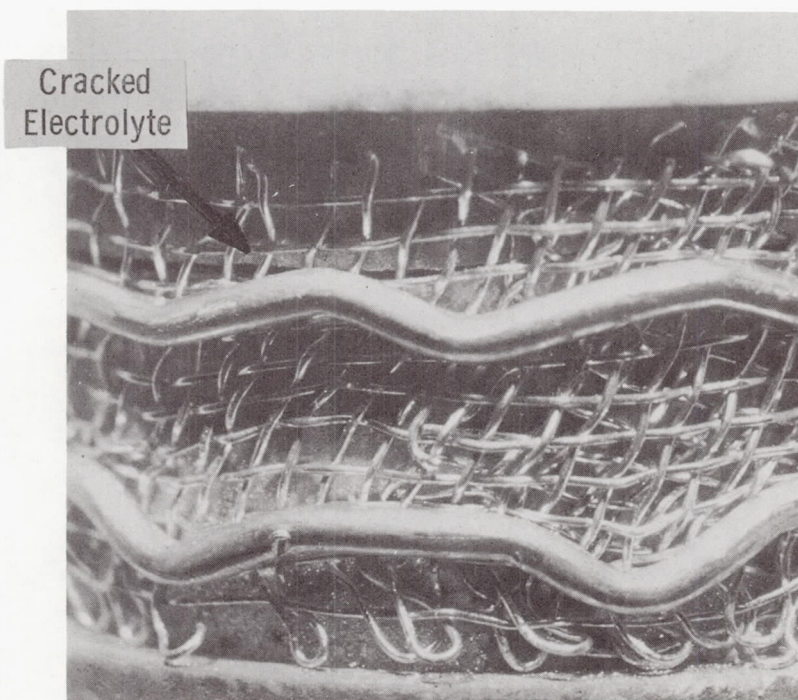
(Cell #3)

Fig.20c - Pictures of individual cells of OBS #8 after failure



Pt electrode
peeling, electrolyte
exposed

(Cell #4)



Cracked
Electrolyte

(Cell #5)

Fig. 20d - Pictures of individual cells of OBS #8 after failure

To understand the electrical effects of a partial loss of electrode consider Fig. 21. When a high resistance R_h develops in the outside electrode of cell #3, parts of the cell current will pass through the main body of cell #3 (resistance of 0.4Ω) but the remainder will go to the small cell near the joint (resistance equals R_s) and through the shunt path (7Ω). The current efficiency will be decreased markedly if R_s is not much smaller than 7Ω . If R_h is large compared to

$$\frac{1}{1/R_s + 1/7}$$

then the flow of current through it will be small and the potential at Probe 6 can approach the potential at point A plus E_t . This explains the apparent decrease in voltage of cell #3 after cell #4 failed and in cell #2 after cell #3 failed. Based on observed cell characteristics R_h approached 100 ohms. However, current efficiency measurements indicate that R_s is small compared to 7 ohms so that the current efficiency does not suffer greatly (compare days 96 and 103 in Table VII). Thus, it appears that even complete failure of the outside electrode will not have a catastrophic effect on battery performance

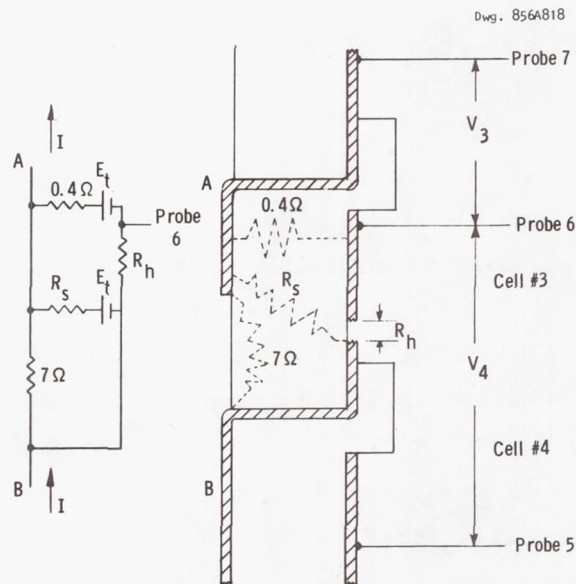


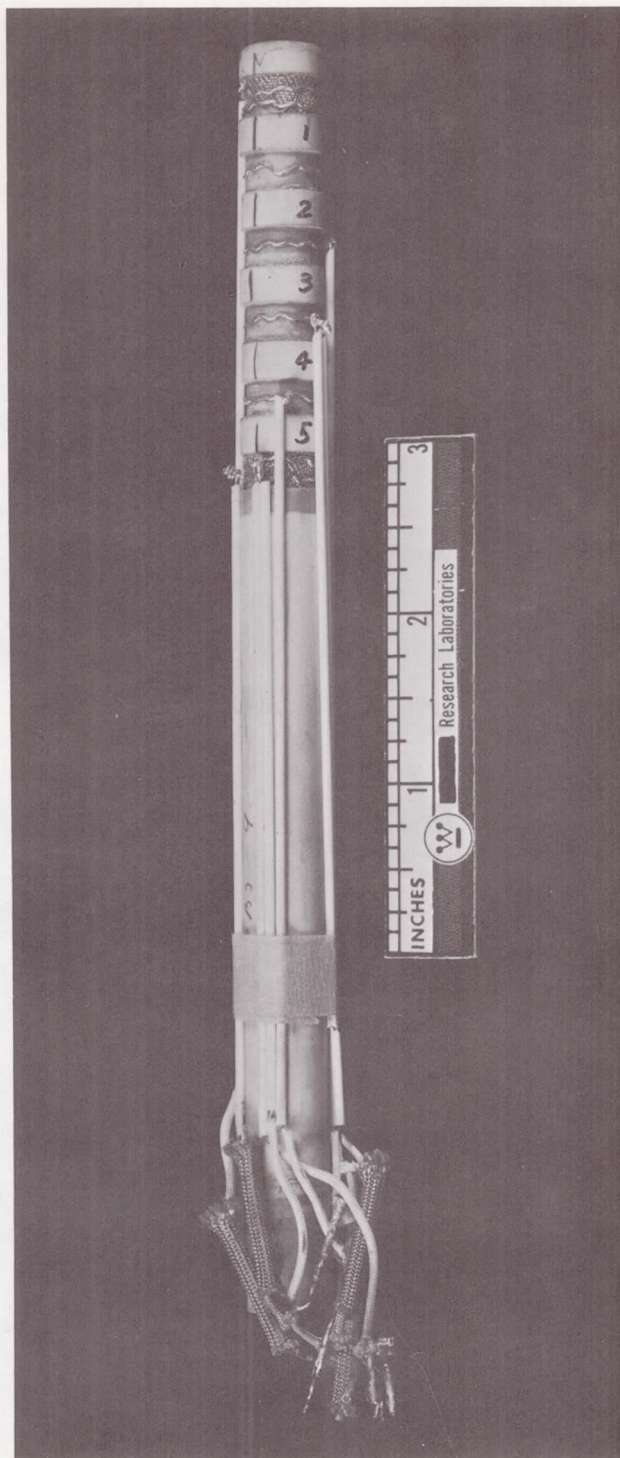
Fig. 21 - Current flow in cell after high resistance develops in outside electrode

and considerable time can pass between the time an electrode fails and that battery is replaced in the circuit.

2.4.2.2 OBS #9

OBS #9 was operated over a period of 112 days. The life test was continuous without any shut down for maintenance. The battery was examined at the end of the test, and the deterioration of the outside electrodes appears to be similar to OBS #8. Figure 22a, 22b, 22c, and 22d show the pictures of OBS #9 after failure at the end of 112 days. The test was terminated because all voltages were unsteady and the oxygen production rate was sharply decreased.

The temperature was maintained at 1000°C throughout the entire test period. The gas composition was dry CO₂ except for the 5th and 6th days when the inlet gas was saturated with water at 50°C (13% H₂O, 87% CO₂) and 65°C (25% H₂O, 75% CO₂) respectively (See Fig. 14). Three different current densities--400, 300, and 200 ma/cm²--were maintained at different times. The driving voltages required to maintain the selected current densities through each of the battery's five cells are shown as a functions of time in Fig. 23. During the first 11 days of the test, very little change occurred. As expected, decreased driving voltages were required when the current density was decreased from 400 ma/cm² to 200 ma/cm² on the eleventh test day. A sharp increase in voltage for cell #5 began on the 20th day. After the current density was increased back to 400 ma/cm² on the 24th day, the driving voltage for cell #5 increased above 3.2 volts. Based on appearance of cells after test, this increase was due to the development of a high resistance on the outside electrode of cell #4 (see Fig. 22d). Almost half of the platinum electrode was removed, the electrolyte above the joint are was exposed. The voltages of cell #2, #3, and #4 were also increased above 2.0 volts, which were much higher than those at 400 ma/cm² on the 11th day. However, their performance was relatively stable throughout the remaining test period.

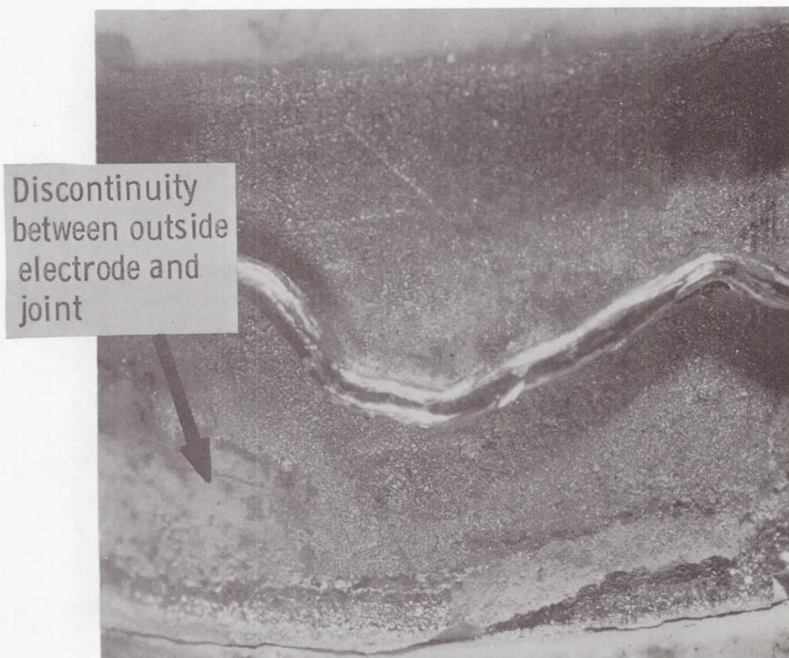


60169 5 CELL BATTERY ZR0₂ ELECTRODE CBS#9

Fig. 22a - Pictures of OBS #9 after failure



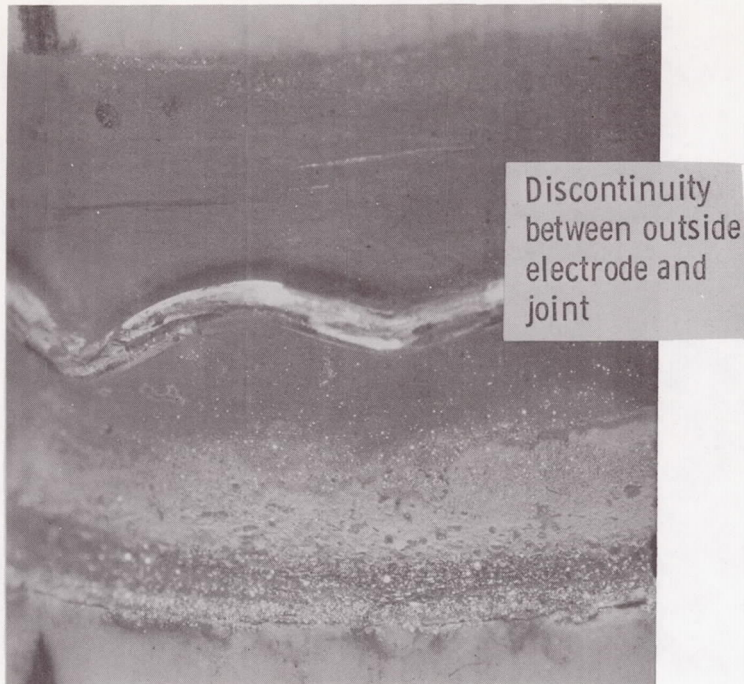
(End Cap)



Discontinuity
between outside
electrode and
joint

(Cell #1)

Fig. 22b - Pictures of individual cells of
OBS #9 after failure



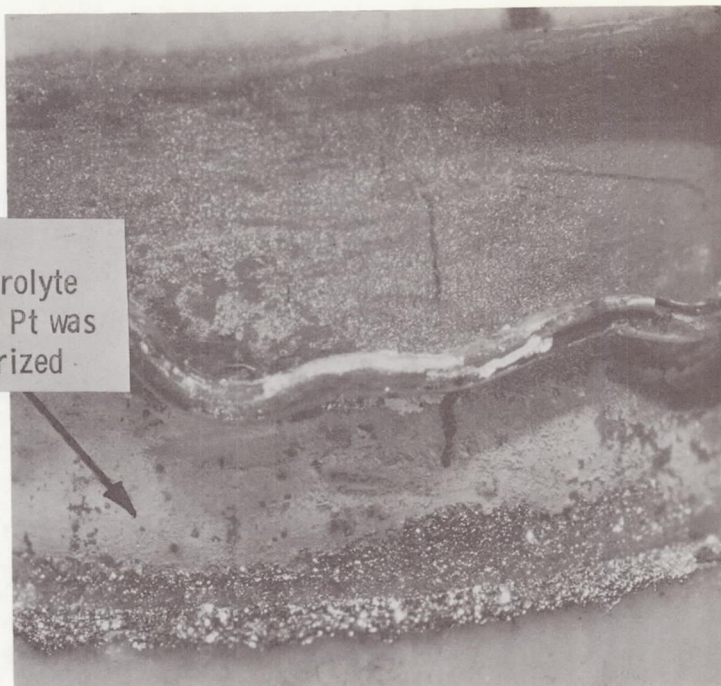
(Cell #2)



(Cell #3)

Fig. 22c - Pictures of individual cells of OBS
#9 after failure

Bare
electrolyte
after Pt was
vaporized



(Cell #4)



(Cell #5)

Fig. 22d - Pictures of individual cells of OBS #9
after failure

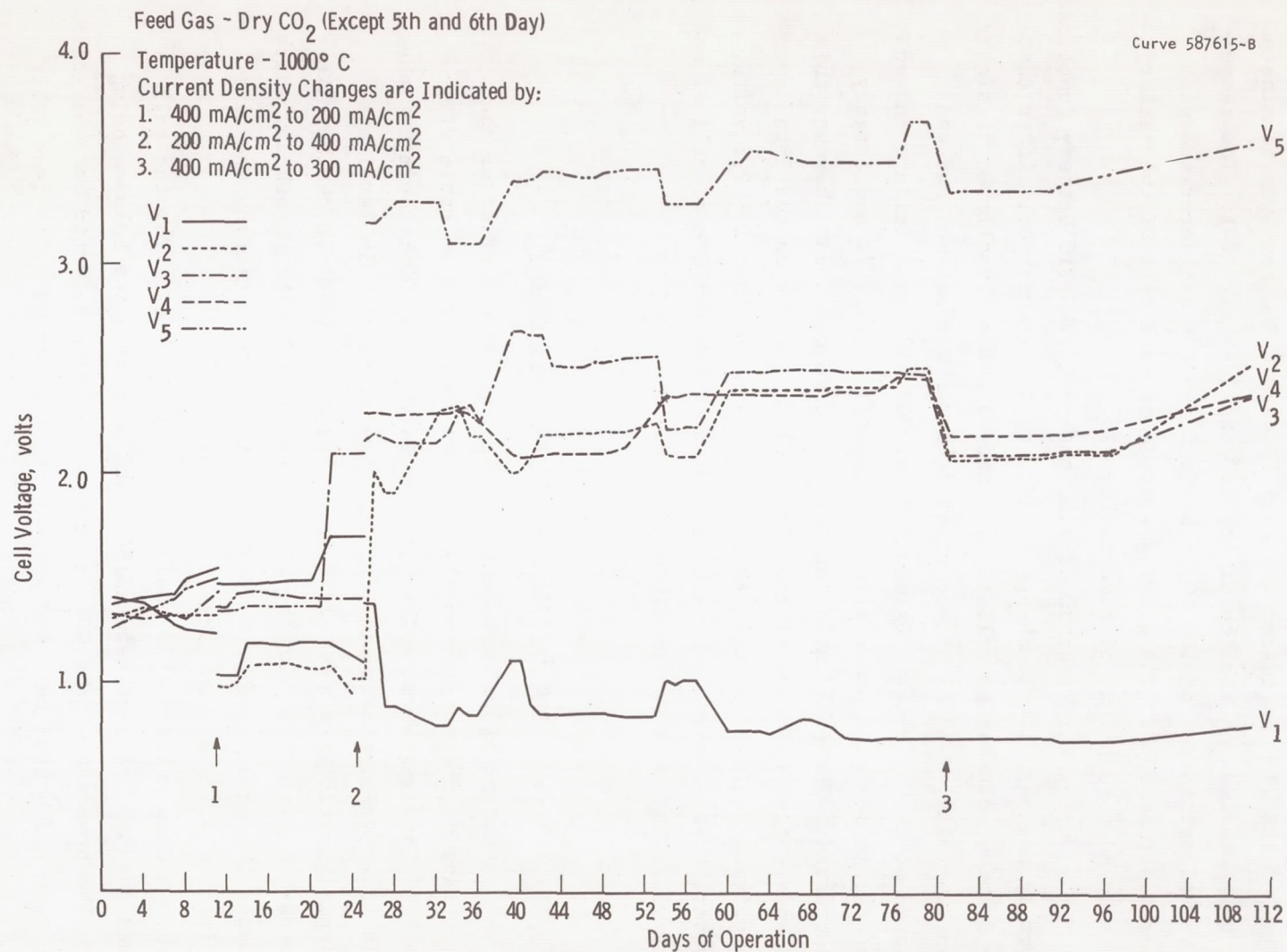


Fig. 23 - Performance of the five cells of OBS #9 during life test

2.4.2.3 OBS #10

OBS #10 was tested for only 77 days. The test was terminated due to a bad leak on the top of the end cap (see Fig. 24). The temperature was maintained at 1000°C. The feed gas CO₂ was saturated with water vapor at 50°C. The driving voltage of each cell of the battery is shown as a function of time in Fig. 25.

During the first 30 days of the test, OBS #10 battery functioned smoothly and very little change in driving force occurred. After that the driving voltages of cell #1, #3, and #5 gradually climbed to higher than 2.5 volts. Cell #1 showed rapid decay in performance and was shunted at the 58th day. Examination of OBS #10 after failure showed that the inside platinum electrode (cathode) of cell #1 had largely disappeared. The explanation at this point is not clear; however this was apparently the cause of the first cell's failure on the 58th day. The driving voltages of cell #2 and #4 remained within 1 ± 0.2 volts, however, this appears to have been caused by the failure of cell #3 and cell #5 as has been previously discussed.

2.4.2.4 Time Variation of Current Efficiency

Current efficiency measurements made on OBS #8 after the replacement of the cracked muffle tube are summarized in Table VII.

The oxygen was collected over water in a 100 cc burette tube as is shown schematically in Fig. 26. The leveling bulb level was ordinarily maintained about 1/2" below the water level in the burette in order to compensate for the 1/2" water level in the O₂ bubbler which precedes the burette. The rate was determined by measuring the time required to collect a specific amount of O₂.

Mass spectrometric analysis of the O₂ stream from the cell showed the % O₂ to vary between 84.4 and 85.6 with the balance being CO₂. The presence of the CO₂ is due to the leaks detected between the base tube and bottom cell and between the two bottom cells (see Table

60973 2X FAILURE ANALYSIS OF CELL

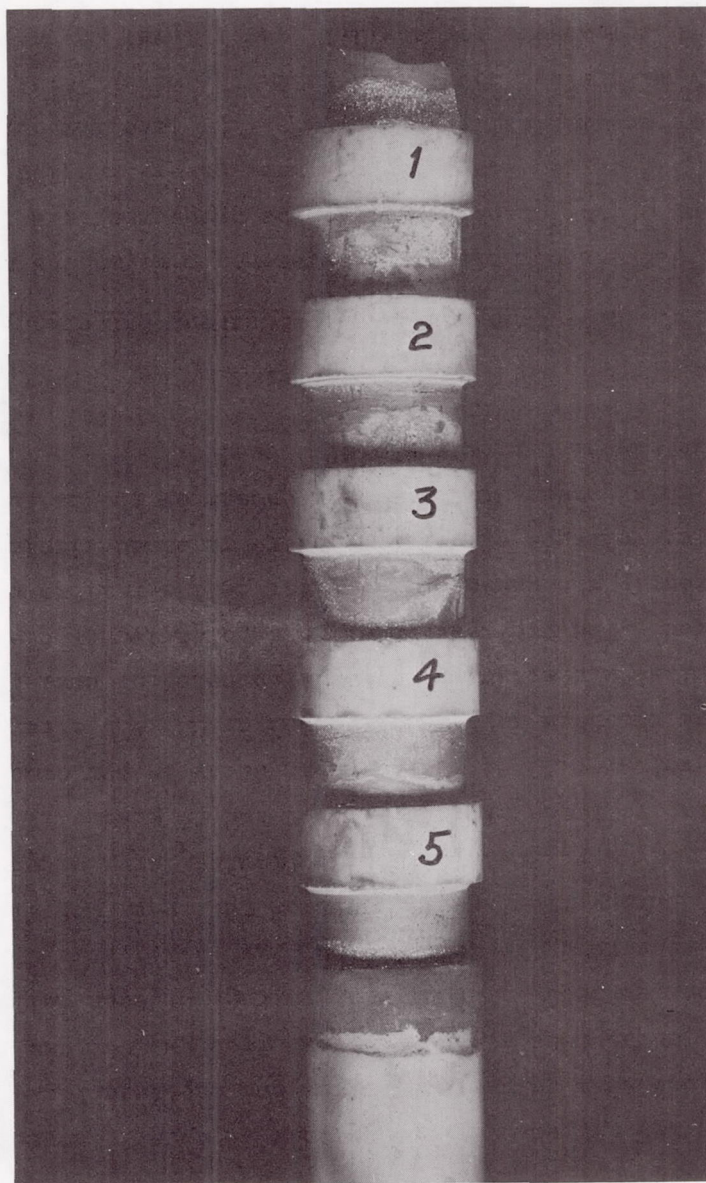


Fig. 24 - Picture of OBS #10 after failure

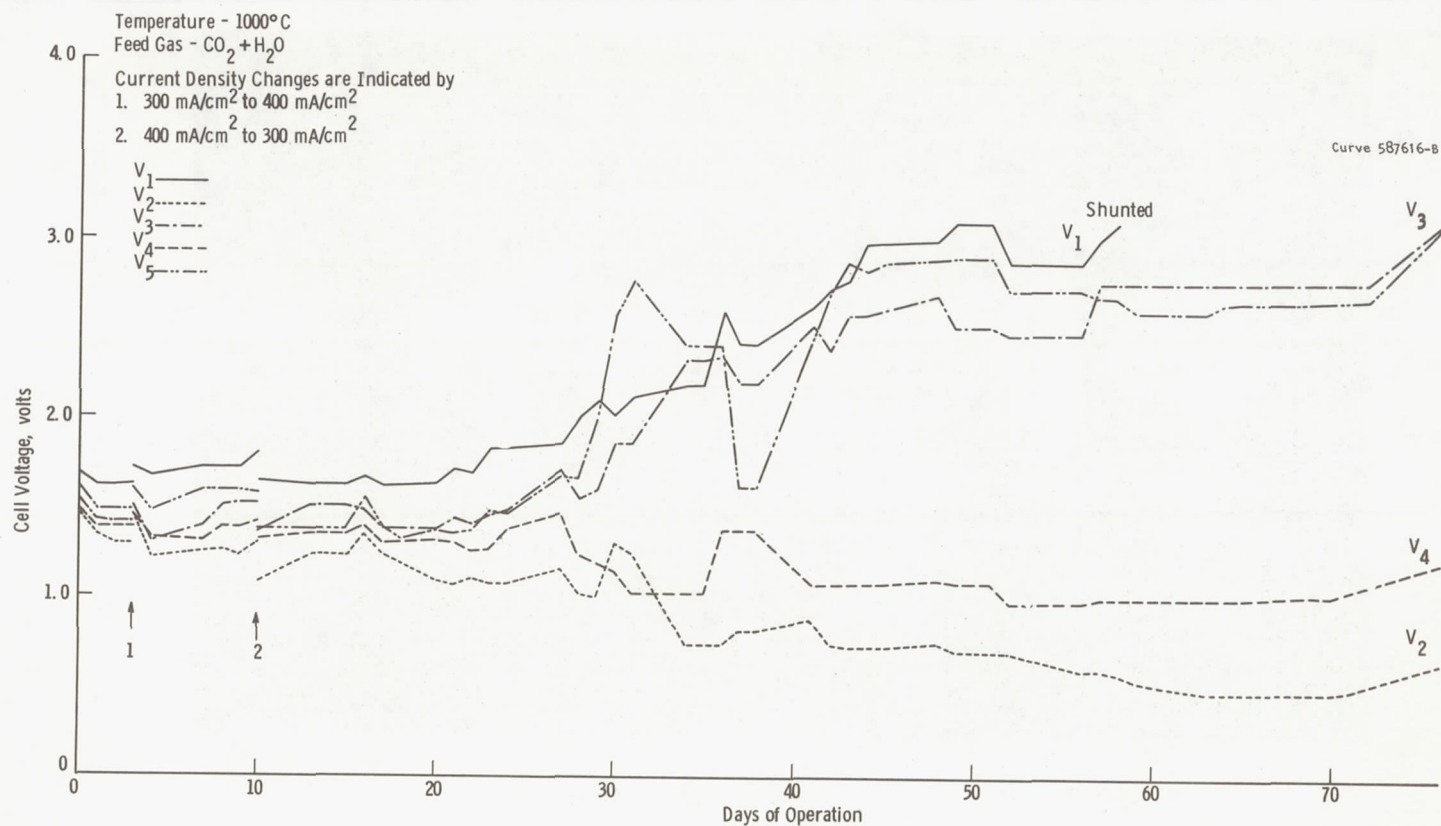


Fig. 25 - Performance of the five cells of OBS #10 during life test

TABLE VII

CURRENT EFFICIENCY MEASUREMENTS OBS #8

T ^a	Cells Oper.	Current, amps	T _c ^b	Rate, cc/min	% O ₂ in Sample	Theor. ^c	Eff.
43	4	0.80	2.10	11.9	-	12.3	0.89 ^d
	4	0.40	2.58	7.0	-	6.15	0.95 ^e
47	4	0.40	3.90	6.41	-	6.15	0.88 ^e
50	4	0.40	3.03	6.20	85.6	6.15	0.86
62	4	0.40	4.00	6.23	84.4	6.15	0.86
69	4	0.40	4.00	6.25	-	6.15	0.87 ^e
71	3	0.40	6.41	3.88	84.8	4.62	0.71
83	3	0.40	6.43	3.86	-	4.62	0.71 ^e
96	3	0.40	6.25	4.00	-	4.62	0.74 ^e
103	5	0.40	4.06	6.15	85.0	7.70	0.68
111	5	0.40	4.10	6.10	85.0	7.70	0.67
121	5	0.40	4.13	6.06	85.0	7.70	0.67
138	5	0.40	4.18	5.98	-	7.70	0.66 ^e
149	5	0.40	5.17	4.83	-	7.70	0.53 ^e

^a T = days since start of test

^b T_c = time to collect 25 cc sample (min)

$$\begin{aligned}
 \text{Theoretical O}_2 \text{ Production} &= \left(I \text{ amps} / 4 \tau \frac{\text{amp sec}}{\text{Mole of O}_2} \right) \times 22,500 \times \frac{298}{273} \\
 &\times \frac{700}{740} \frac{\text{cc}}{\text{min}} \times 60 \text{ sec/min} \\
 &= \left(\frac{22,500 \times 60 \times 298 \times 700}{4 \times 96,500 \times 273 \times 740} \right) I = 3.85 I \left(\frac{\text{cc}}{\text{min}} \right)
 \end{aligned}$$

^d Assume 92% O₂ because of higher O₂ production rate

^e Assume 85% O₂

VIII prior to testing. The fact that the measured rates are higher than theoretical implies that the rate of CO₂ leakage into the oxygen chamber was slightly higher than the rate of oxygen leakage out, probably due to the presence of a slightly higher pressure on the feed side during the current efficiency measurements.

The gradual decrease in current efficiency with time is readily understood in terms of changes in cell driving voltages and resistances with time. The ratio of shunt current to cell current can be approximated by:

$$\frac{I_{\text{shunt}}}{I_{\text{cell}}} = \frac{V/R_{\text{shunt}}}{(V-E_t)/R_{\text{cell}}} \quad (12)$$

The ratio of $R_{\text{shunt}}/R_{\text{cell}}$ can be computed from cell dimensions, and is approximately 20 for the bell and spigot segments used in these experiments. Thus, at the outset when the average V was 1.2 volts/cell

$$\frac{I_{\text{shunt}}}{I_{\text{cell}}} = \frac{1.2 \text{ volts}}{20 (1.2 - 0.71) \text{ volts}} = 0.122$$

$$E_{\text{theoretical}} = \frac{1}{1 + 0.122} = 0.89$$

Thus, it is concluded that the losses in efficiency are due to the increased shunt currents which result from the volatilization of the outside electrode.

2.4.2.5 Time Variation of Power Efficiency

The power efficiency of OBS #8, #9, and #10 were determined during the life test from Figs. 12, 13, 18, 23, and 25. Fig. 27 shows the power efficiency of each battery against the days of operation. The

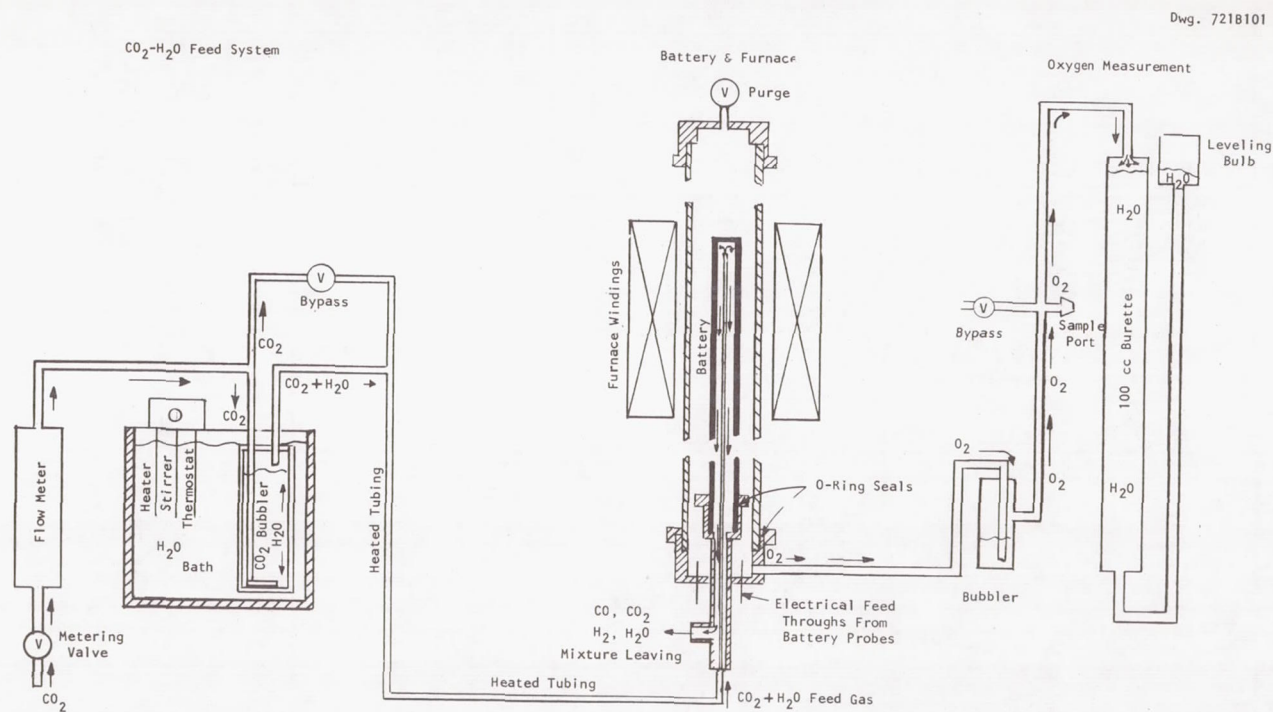


Fig. 26 - Battery test apparatus including feed system and oxygen flow rate measurement

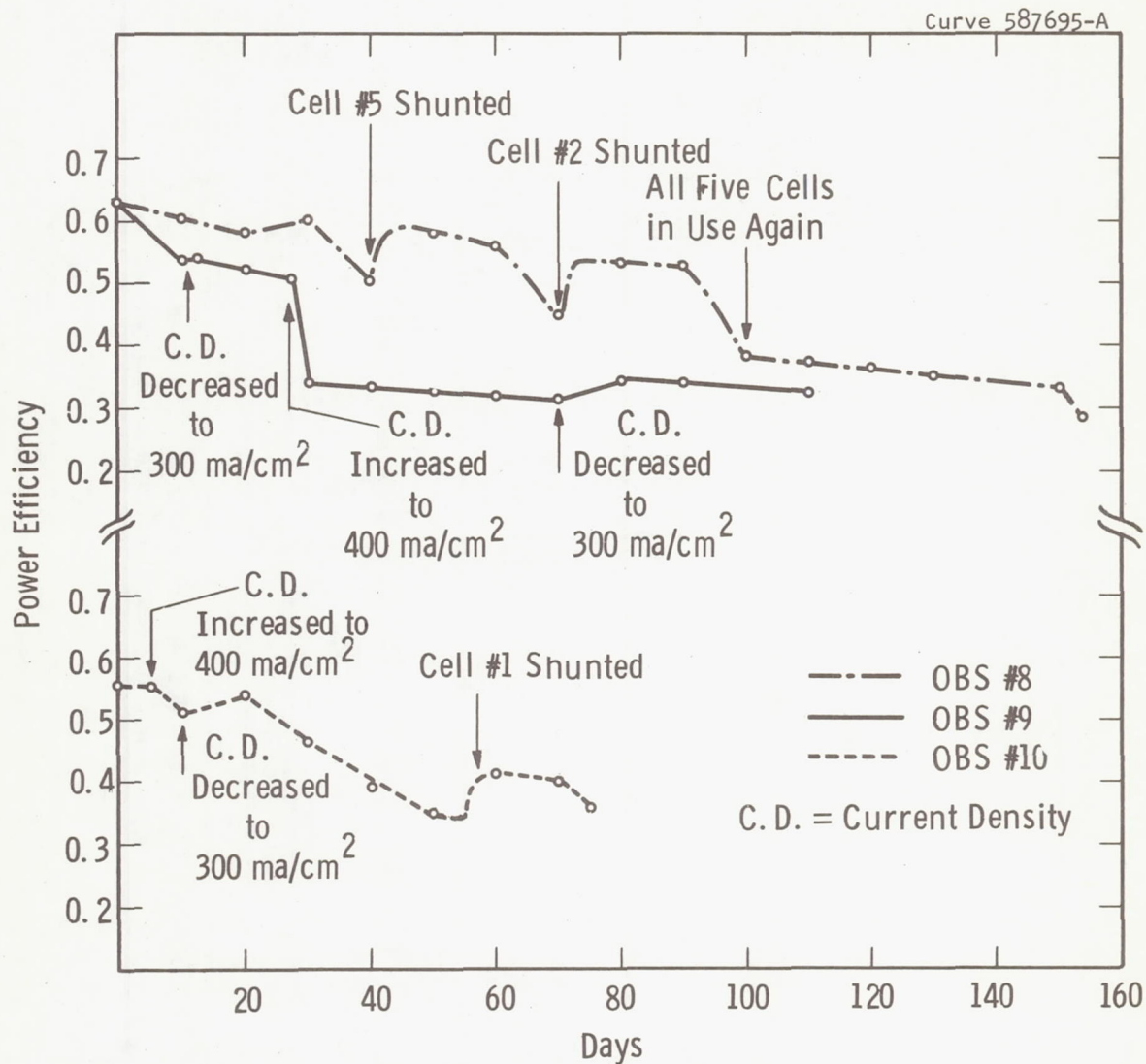


Fig. 27 - Power efficiency of the batteries during life test

gradual decrease in power efficiency with time resulted from the increase in driving voltages with time which in turn resulted from the evaporation and peeling of the outside electrode described previously.

2.4.2.6 Effects of Fabrication Variables and Operating Conditions

This section considers the effect of fabrication variables--anode electrode type, electrode weight, electrode composition, and percent gold in the joint--and the effect of operating current density and temperature on the life of the bell-and-spigot batteries tested.

Two different types of anodes were used in the life-tested batteries: The sputtered Pt-ZrO₂ electrode and a composite electrode in which a heavy layer of sintered Pt was applied on top of a thin sputtered layer. OBS #10 was fabricated with sputtered anodes while OBS #8 and OBS #9 had composite electrodes (see Table VIII). The major difference in performance appears to be that OBS #10 with sputtered anodes had a lower power efficiency initially (see Fig. 27). However, the rate of deterioration in power efficiency appears to be the same for the two electrode types considering the accuracy of the data collected and the variations in current density and temperature superimposed on the runs. An additional difficulty in comparing the results obtained with sputtered and composite electrodes is the fact that the ZrO₂ in the sputtered electrode was higher than desired (31-40%) and the total weight density (7.3 to 9.8 mg/cm²) was lower than desired; the combined effect was an increase in electrode resistance. Thus, the need for improved sputtering control is emphasized as a prerequisite to selecting the electroding technique.

Theoretical considerations indicate that a high percentage of gold in the joint will lead to faster sintering and ultimately to faster failure of the anode (see p.10). A plot of the time to failure as a function of the % gold in the joint, Fig. 28, gives little statistical evidence for assuming a strong correlation between the two. (The apparent correlation in Fig. 28 is strongly dependent upon a

TABLE VIII
FABRICATION SUMMARY FOR LIFE TESTED BATTERIES

Segment No.	Cell No.	Anode W_S , mg/cm ²			% Pt of Sputtered Anode	Cathode W_S , mg/cm ²	W_{Au} ,mg	W_{Pt} ,mg	% Au	Tightness*	R_m	R_{ohms}
		Sputtered	Sintered	Total								
OBS #8												
54	1	2.2	10.8	13.0	87	8.5	15.5	29.5	34	T	0.3	0.35
64	2	2.5	6.7	9.2	83	8.8	15.5	35.0	31	T	0.4	0.35
63	3	2.6	7.0	9.6	83	9.4	15.5	29.5	34	T	0.3	0.30
61	4	2.5	7.0	9.5	85	8.9	24.0	29.5	45	T	0.2	0.30
56	5	2.1	8.3	10.4	80	7.9	24.0	28.0	46	L	0.1	0.30
Base	-	-	-	-	-	-	24.0	32.5	42	S	0.4	-
OBS #9												
55	1	2.5	6.7	9.2	80	9.3	63.5	31.0	67	LLL	0.4	-
57	2	2.3	7.7	10.0	72	7.3	15.5	26.5	37	TTT	0.3	-
51	3	2.4	5.7	8.1	87	9.6	15.5	31.5	33	TTT	0.4	-
60	4	2.0	6.5	8.5	85	8.3	15.5	28.6	35	TTT	2.5	-
58	5	2.6	5.7	8.3	72	7.6	15.5	25.2	38	TTT	0.3	-
Base	-	-	-	-	-	-	39.5	30.0	57	STT	0.4	-
OBS #10												
42	1	7.3	0	7.3	60	6.2	24.0	22.5	52	S	0.25	0.725
40	2	9.4	0	9.4	69	8.9	24.0	26.0	48	T	0.25	0.2
45	3	6.8	0	6.8	60	8.2	15.5	28.0	36	T	0.50	0.5
41	4	8.6	0	8.6	69	10.0	15.5	27.0	37	T	0.40	0.3
50	5	9.8	0	9.8	67	6.6	24.0	24.0	50	S	0.25	0.425
Base	-	-	-	-	-	-	24.0	30.0	45	T	0.25	-

* T = Tight Joint, S = Small Leak, L = Large Leak; Three Letters for OBS #9 Indicate Joint Tightness After Each of Three Firings.

single point at 70 days.) However, the fact that the slope of the curve is in the anticipated direction indicates that further work on improving life by this method is justified. It should be noted that the most important variable may not be the total gold applied to the joint, but the amount of gold which does not flow into the joint but remains on the rim where it can diffuse readily into the adjacent electrode.

One of the most important effects to be noted in Fig. 27 is the fact that OBS #8 had a much longer life and higher power efficiency (after initial testing) than OBS #9 despite the fact that their

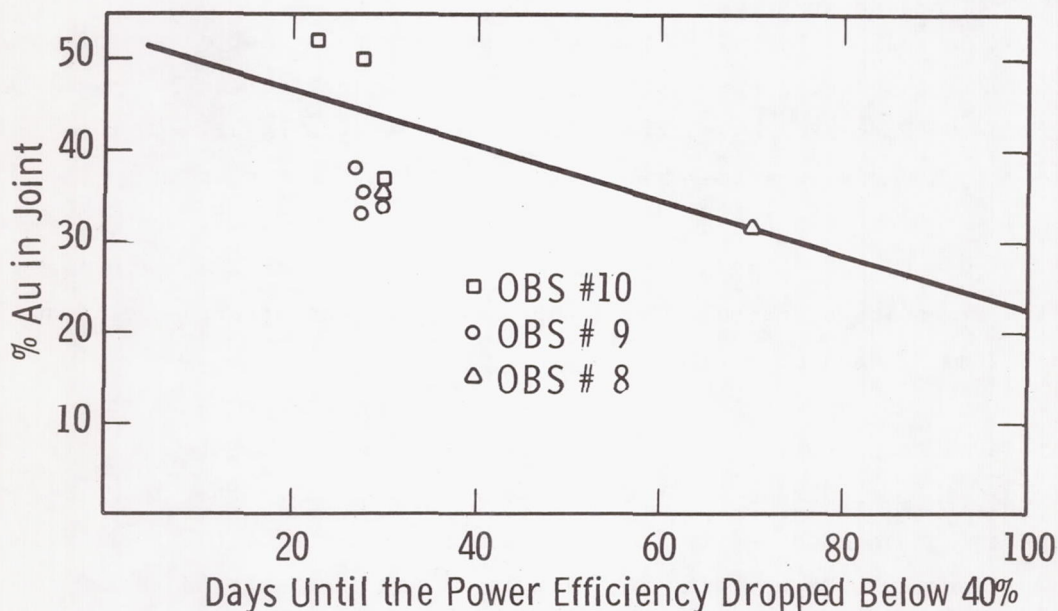


Fig. 28 - Time to failure as a function of joint composition

fabrication (anode fabrication, weight, % gold in joints) was essentially identical (see Table VIII). This is believed to be due to the combined effects of operating temperature and current density. OBS #8 was operated at 920°C (vs 1000°C) and at a current density of 200 ma/cm²

for most of its life (vs 300 to 400 ma/cm²). Thus, it appears that high current densities and temperatures lead to shorter life, although it is not possible to tell which has the greater effect from the data collected as a part of this work.

2.4.3 Battery Performance Summary

The performance of the life-tested batteries demonstrated that initial overall efficiencies greater than 50% can be obtained and that battery operating lives of 100 days can be readily exceeded.

The batteries with composite anodes exhibited power efficiencies of 58 to 61% at 300 ma/cm² and 1000°C, and current efficiencies approaching 90% during initial tests; this corresponds to an overall efficiency of 52 to 55%. Cell resistance and polarization contributed approximately equal amounts to the electrical inefficiencies. Somewhat poorer performance was obtained from the battery with all-sputtered anodes; however, this may be the result of high ZrO₂ content in the anodes rather than the fact that sputtering was employed.

Lives of 152 and 112 days were achieved for the batteries with composite electrodes while the battery with sputtered electrodes achieved 77 days of life.

An important observation was the fact that loss of the outside electrode continuity does not lead to catastrophic failure, only to losses in current and power efficiency. This implies that in an operating system batteries can be allowed to run until their efficiency decreases below a certain specified level and then changed at the convenience of the astronauts.

Analysis of the operating data, as well as visual examination of the batteries after failure, leads to the conclusion that the decreases in current and power efficiency with time (from greater than 50% initially to less than 20% just prior to failure) are both caused by the volatilization of the anode. In the case of the power efficiency, the effect is a direct of the increase in anode resistance. In the case of current efficiency, the higher resistance causes increases in shunt currents which in turn reduce the efficiency.

The results of this work confirm that solid electrolyte electrolysis is a promising method of oxygen regeneration and at the same time emphasize the need for concentrated efforts to improve anode life. Possible methods of improving battery performance and life which should be investigated in future research include:

1. Closer tolerance of joints should be maintained so that a better fit can be obtained. In this manner, it is hoped that better distribution of gold into the joint (and loss at the collar) can be achieved. Also, lower leakages should result in higher current efficiencies.
2. A thicker outside Pt electrode is suggested in the vicinity of the joint so that a low percent of gold in the joint can be established.
3. Better control over sputtering must be achieved so that the effect of percent of ZrO_2 in both sputtered and composite electrodes can be evaluated. Investigation should include direct measurements of effect on performance and life as well as metallographic investigation to determine distribution of the ZrO_2 in the Pt. matrix.
4. Effect of lower operating temperature (800-900°C) on performance and life should be investigated.

3. CARBON PRECIPITATION FROM CO-CO₂-H₂ MIXTURES

The objective of this part of the investigation was to develop a reactor for continuously converting CO to CO₂ and solid C by the catalyzed reaction



using a gas feed similar in composition to the effluent of the electrolysis battery. The main requirements to be met by the reactor were: 1) efficient conversion of CO, 2) low catalyst consumption, 3) easy removal of carbon, and 4) production of a gas free of catalyst or carbon particles.

The first phase of the investigation covered the selection of a suitable catalyst and the acquisition of data showing the effects on the reaction rate of reactor geometry, temperature, gas composition and flow rate. The second phase covered the fabrication of a reactor meeting the above requirements and continuous operation of the reactor for a period of 100 days.

A literature survey revealed the following information: The most effective catalysts for the carbon precipitation reaction are Fe, Co, and Ni, and the most suitable temperature lies between 450 and 600°C.⁹⁻¹⁵ Hydrogen enhances the reaction rate but the mechanism is unknown.¹⁰ The catalyst is slowly consumed during the reaction and appears as metal carbide in the carbon product. Because the catalyst is consumed, the quantity of carbon that can be produced by a given quantity of catalyst is limited. With powdered Fe catalysts, carbon loadings as high as 60 to 1 were reported.⁹

3.1 Catalyst Evaluation Study with Packed-Bed Reactor

The catalyst evaluation experiments were conducted with a small packed-bed reactor. The plan of investigation was to measure carbon deposition rates with various commercial catalysts, using gas feeds consisting of either pure CO or mixtures of CO with H_2 and CO_2 .

The experimental reactor is illustrated in Figure 29. It was constructed of 304 stainless steel and was 1.5 in. ID by 10.5 in. long. The lower half of the reactor was uniformly heated and comprised the reaction zone. Auxiliary equipment included individual flowmeters for CO, CO_2 , and H_2 ; a manometer for measuring pressure drop; and a wet test meter for monitoring the flow of exhaust gas.

The major problem expected in the experiments was plugging of the reactor before a satisfactory carbon loading could be achieved. To provide sufficient free space for

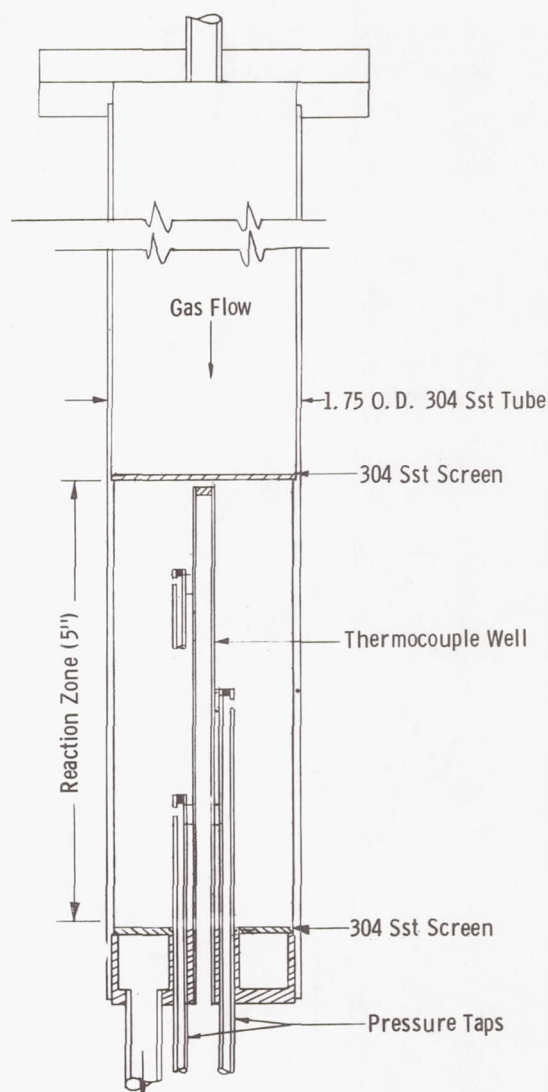


Fig. 29 - Packed bed carbon-deposition reactor

the solid carbon, powdered catalysts were dispersed in loose Fiberfrax wool and granular catalysts were supported on wire screens in one or more thin beds. Pressure taps were located at three levels within the reaction zone so that variations in pressure drop with bed depth could be followed during an experiment.

In conducting the experiments the catalysts were pretreated with H_2 at temperature for several hours before introducing the actual feed gas. The rate of carbon deposition was followed by observing the difference in volume between the input and output gas. (One mole of gas disappears for each mole of carbon deposited.) The total weight of carbon product was found by weighing the reactor. All gases were technical grade.

The operating conditions and the results of the tests run with the packed-bed reactor are presented in Table IX. A summary of the results follows: In all tests in which CO alone was used as the feed gas (tests 1-14), the rate of CO conversion gradually declined with time similar to the results shown in Figure 30. On the addition of 3 percent

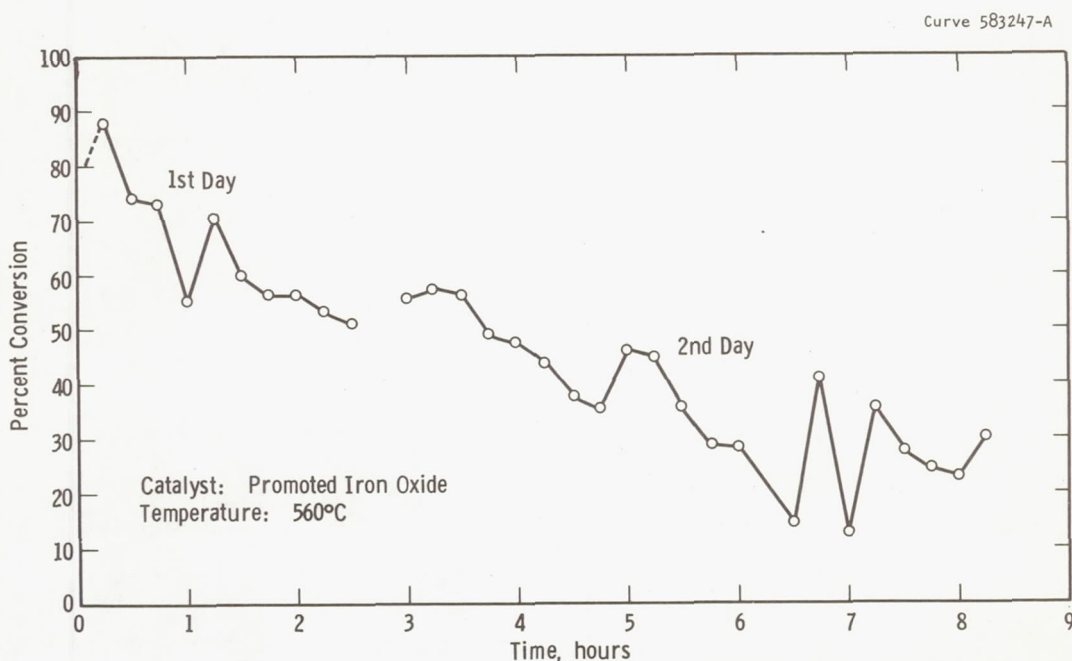


Fig. 30 - Typical conversion of CO as a function of time when H_2 was not included in feed

TABLE IX
RESULTS OF CARBON DEPOSITION TESTS WITH PACKED BED REACTOR

Test No.	Catalyst	Temp, °C	Gas Flow, std cc/min	Input Gas Composition, %			Weight of Catalyst, g	Test Hours	Avg Conv of CO, %	Carbon WT, g	Carbon/Cat. Ratio	Carbon Rate, g/hr
				CO	CO ₂	H ₂						
1	Girdler H219 Nickel Oxide Powder on Fiber Frax Wool	560	988	99.5	--	--	1.0	2.75	0	0	0	0
2	Girdler H219 Nickel Oxide Powder on Fiber Frax Wool	520	262	99.5	--	--	2.0	2.66	14.0	1.4	0.7	0.53
3	D-3001 Synthetic NH ₃ Catalyst, 4/20 Mesh, Single Bed	560	583	99.5	--	--	20.0	4.50	69.0	18.2	0.91	4.03
4	D-3001 Catalyst, 4 Thin Beds, 1" apart on Screen Supports	560	441	99.5	--	--	20.0	8.00	46.0	23.5	1.17	2.94
5	D-3001 Catalyst Supported in Steel Wool	560	136	99.5	--	--	10.0	4.70	49.0	7.5	.75	1.595
6	Fused Promoted Iron Oxide, 14/28 Mesh	570	400	99.5	--	--	10.0	5.08	52.0	14.5	1.45	2.85
7	Pelletized Promoted Iron Oxide, 9/20 Mesh	570	400	99.5	--	--	10.0	7.50	47.0	21.0	2.10	2.80
8	H219 Nickel Oxide Granules, Unsintered, 9/20 Mesh	570	400	99.5	--	--	5.0	6.83	29.0	11.0	2.20	1.61
9	H219 Nickel Oxide Granules, Sintered, 9/20 Mesh	550	400	99.5	--	--	2.0	7.25	9.7	3.90	1.95	.27
10	H219 Nickel Oxide Powder on Fiber Frax Wool	520	135	99.5	--	--	5.0	8.08	9.6	1.89	0.38	.234
11	678 Nickel Oxide Pellets, 1/4" x 1/4"	540	400	99.5	--	--	5.47	26.0	21.2	13.5	2.47	.520
12	H219 Nickel Oxide Granules, Sintered, 9/14 Mesh	475	135	99.5	--	--	10.0	31.5	34.0	20.4	2.04	.647
13	H219 Nickel Oxide Powder on Fiber Frax Wool	470	200	99.5	--	--	5.0	29.3	16.8	14.1	2.82	.472
14	678 Nickel Oxide Granules, 6/9 Mesh	645	200	99.5	--	--	5.0	28.0	21.5	17.3	3.46	.618

TABLE IX - CONTINUED
RESULTS OF CARBON DEPOSITION TESTS WITH PACKED BED REACTOR

Test No.	Catalyst	Temp, °C	Gas Flow, std cc/min	Input Gas Composition, %			Weight of Catalyst, g	Test Hours	Avg Conv of CO %	Carbon Wt, g	Carbon/Cat. Ratio	Carbon Rate, g/hr
				CO	CO ₂	H ₂						
15	Carbonyl Iron Powder on Fiber Frax Wool	575	222	93.3	--	6.2	5.0	28.0	76.0	63.0	12.6	2.25
16	000 Grade Steel Wool	575	215	96.0	--	3.5	2.0	51.7	60.0	92.0	46.0	1.78
17	Carbon Granules from Test 16	575	213	93.5	--	6.1	5.3	23.6	62.0	42.0	7.93	1.78
18	Reactor Wall	570	209	95.2	--	4.3	--	21.0	65.0	39.0	--	1.86
19	Reactor Wall	575	203	97.9	--	1.6	--	17.5	9.8	5.0	--	.285
20	Reactor Wall	580	435	91.5	--	8.0	--	23.5	65.0	88.0	--	3.74
21	Reactor Wall	580	203	72.6	--	3.6	--	21.3	49.0	22.2	--	1.04
			209	70.5	--	6.3	--	4.3	47.0	4.3	--	1.0
22	Reactor Wall	580	215	67.2	--	10.5	--	25.3	43.0	22.7	--	.897
			432	67.1	--	10.6	--	5.5	42.0	9.6	--	1.74
23	Reactor Wall	580	810	72.6	23.5	3.6	--	4.50	43.5	16.7	--	3.71
24	Reactor Wall	585	857	70.8	22.8	6.3	--	5.25	27.7	13.2	--	2.40
25	Reactor Wall	580	207	96.2	--	3.3	--	19.0	71.4	39.2	--	2.06
			417	96.2	--	3.3	--	2.50	69.6	10.1	--	4.04
			833	96.3	--	3.2	--	2.00	50.9	11.8	--	5.9
26	Carbon Steel Liner	580	229	95.6	--	3.9	--	2.83	70.3	6.1	--	2.05
			429	95.0	--	4.5	--	.83	65.3	3.2	--	3.85
			857	95.0	--	4.5	--	.50	64.6	3.8	--	7.61
27	Stainless Steel Liner	580	207	96.2	--	3.3	--	5.50	43.0	6.8	--	1.24

or more of H_2 , however, the rate of conversion remained virtually constant at a high level. Carbon dioxide addition to a $CO-H_2$ feed caused a drop in the conversion rate, but the rate was constant with time.

The most important observation was that hydrogen activated not only the catalyst charge but also the dense stainless steel shell of the reactor itself. In fact, much of the carbon produced in tests 15-17 apparently precipitated directly on the reactor wall rather than on the catalyst charge. This conclusion was confirmed by tests 18-27, in which no catalyst other than the reactor wall was used.

Because deposition of carbon on the reactor wall rather than within a catalyst bed seemed to be more readily adaptable to continuous operation, the experiments with granular and powdered catalysts were discontinued so that the work could be concentrated on developing a reactor in which the wall acted as the catalyst. With the latter type of reactor, the need for replacing spent catalyst would be eliminated and the reactor would be less subject to plugging.

3.2 Continuous Reactor Experiments

The first continuous reactor was constructed from a 1.5-inch diameter stainless steel tube and had a 12-inch long reaction zone. Gas input was at the top; the bottom end was connected by rubber hose to a large glass flask which served as a storage compartment for carbon. No special means was provided for dislodging carbon. It was hoped that the deposit would flake off naturally, aided perhaps by temperature cycling or by mechanical vibration.

The results of the experiments are given in Table X. The reactor was not immediately effective in converting CO. At the end of the first test (test 28), which lasted 19 hours, conversion of CO had reached only 59 percent. Operation at $665^{\circ}C$ in test 29 apparently activated the reactor wall because a very high conversion rate (84 percent) was achieved in test 30. (The need for an activation period with stainless steel was indicated also by test 27 in which a new stainless steel liner was placed inside the packed bed reactor. At the end of this 5.5-hour test, conversion of CO had reached only 45 percent.)

TABLE X
RESULTS OF CARBON DEPOSITION TESTS WITH STAINLESS STEEL CONTINUOUS REACTOR

Test No.	Temp, °C	Gas Flow, std cc/min	Input Gas Composition, %			Test Hours	Average Conversion of CO, %	Carbon Weight, g	Carbon Rate, g/hr
			CO	CO ₂	H ₂				
28	580	214	95.3	--	4.2	19.00	51.6	29.1	1.53
		418	95.2	--	4.3	2.40	43.5	6.0	2.48
29	665	211	95.3	--	4.2	3.00	68.2	5.5	1.84
	550	205	95.3	--	4.2	2.25	43.5	3.1	1.38
	665	208	95.3	--	4.2	19.00	54.5	29.8	1.57
30	575	208	95.3	--	4.2	76.60	83.8	185.5	2.42
31	575	202	48.4	48.4	2.8	25.00	33.0	11.6	0.46
		211	63.6	31.8	4.2	18.00	43.2	14.9	0.82
		105	64.0	31.4	4.2	2.00	20.7	0.4	0.20
		210	76.3	19.1	4.2	22.50	54.2	27.9	1.24
		462	76.3	19.1	4.2	4.00	36.2	6.5	1.62

Test 30 demonstrated that a constant rate of carbon deposition over a long period (77 hours) can be achieved if the reactor does not become plugged with carbon. In this test, tapping the top of the reactor sharply with a hammer was successful in dislodging the carbon deposit. Conversion of 84 percent of the carbon monoxide feed over the 77-hour test period approached the limit set by equilibrium (90 percent at 575°C).

In test 31 CO_2 was added to the feed gas and caused a marked decrease in the rate of conversion. Also, the carbon deposits were tighter and could no longer be dislodged by tapping or vibrating the reactor. Temperature cycling was also without effect, and it was concluded that a more positive means for freeing the carbon was needed.

Accordingly, a new continuous reactor was constructed, similar to the first but provided with a scraper for removing carbon. A second modification was the installation of a tight-fitting carbon steel (SAE 1015 grade) liner inside the stainless steel reactor shell. Only one previous test (test 26) had been conducted with a carbon steel catalyst. In test 26 the carbon steel required no activation but gave high conversion of CO from the start. Carbon steel appeared to be superior in this respect to stainless steel.

The scraping device consisted of a hollow stainless steel shaft with stiff vanes attached at 1-inch intervals. The upper end of the shaft passed out of the reactor through a brass bushing with an O-ring gas seal. A cross bar was provided for turning. Carbon was allowed to build up to a considerable thickness before scraping so that coarse chips of carbon would be produced rather than fine powder. No difficulty was encountered in scraping off the deposits.

Three experiments (tests 32-34) were run with this reactor. Total operating time was 12.5 days and carbon production was 1,100 grams. The experiments ran smoothly and achieved high conversions of CO over a wide range of operating conditions. The results are given in Table XI.

On completion of test 34, the reactor was cut open and the steel liner inspected. Attack on the liner seemed uniform. No pitting had occurred and the surface had a smooth matte-finish appearance. Analysis of the carbon deposit showed that it contained about 2 percent Fe.

TABLE XI
RESULTS OF CARBON DEPOSITION TESTS WITH CARBON STEEL-LINED CONTINUOUS REACTOR

Test No.	Temp, °C	Gas Flow, std cc/min	Input Gas Composition, %			Test Hours	Average Conversion of CO, %	Carbon Weight, g	Carbon Rate, g/hr
			CO	CO ₂	H ₂				
32	585	208	96.3	--	3.6	3.0	69.8	6.0	2.0
	585	208	76.9	19.4	3.6	25.0	69.5	40.0	1.60
33	585	208	76.9	19.9	3.6	34.6	68.3	54.0	1.56
	585	416	76.9	19.9	3.6	2.3	67.4	7.2	3.11
	585	832	76.9	19.9	3.6	25.0	65.5	153.0	6.13
	585	1140	76.7	19.3	4.0	24.0	54.0	163.0	6.80
	525	1140	76.7	19.3	4.0	19.0	37.0	88.5	4.66
	640	1140	76.7	19.3	4.0	71.0	46.0	410.0	5.77
34	525	416	76.9	19.4	3.6	24.0	68.5	75.6	3.15
	640	416	76.9	19.4	3.6	24.0	63.0	69.6	2.90
	640	105	76.2	19.1	4.7	20.0	59.0	13.5	0.56
	585	105	76.2	19.1	4.7	27.0	54.0	17.4	0.64

(Carbon deposited on a stainless steel catalyst contained 1 to 2 percent Fe together with smaller proportions of Ni and Cr.) The total iron loss was 22 grams, which is equivalent to 3 mils of liner thickness, assuming uniform attack. The thickness of the liner at the start was 60 mils. On the basis of these tests, it was concluded that a 60-mil liner should easily last 100 days at the same average gas flow. Because of the low catalyst consumption and the high conversion of CO achieved in tests 32-34, a similar reactor design was chosen for the 100 day life test.

3.3 100-Day Life Test of Continuous Carbon Deposition Reactor

The objectives of the 100-day life test were as follows:

1. Demonstrate that the design and construction of the reactor were adequate for continuous operation for 100 days at a one-eighth man rate (34.5 g of carbon per day).
2. Demonstrate the ability of the reactor to produce carbon at high efficiency under conditions compatible with the oxygen electrolysis battery. These conditions were: (a) the feed gas was to consist of approximately 75 percent CO, 21 percent CO₂, and 4 percent H₂ and (b) conversion of CO in the feed to CO₂ and solid C was to exceed 60 percent.
3. Demonstrate that carbon could be readily removed from the reactor without interrupting operation and that the product gas could be kept free of carbon dust.
4. Obtain data needed to optimize the reactor design.

3.3.1 Description of Reactor

A schematic diagram of the 100-day test reactor is shown in Figure 31. The main reactor tube was made of 304 stainless steel and was lined throughout the heated zone with a tight-fitting carbon steel tube (SAE 1015 grade). The inner tube, which served as the catalyst, was 1.495 in. ID and had a .059 in. wall. The length of the heated zone was 12 in.

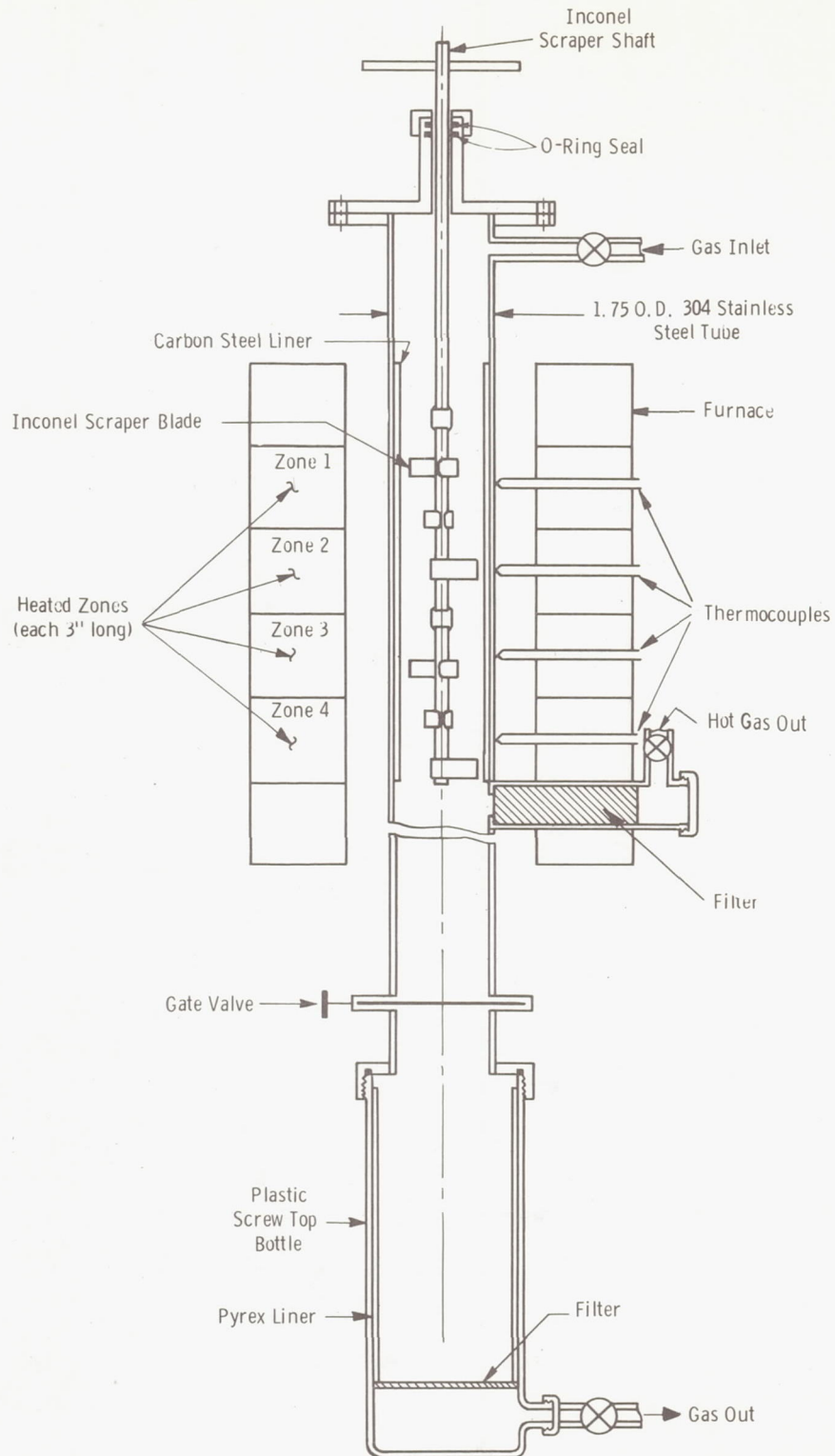


Fig. 31 - Schematic diagram of 100-day carbon deposition reactor

A rotary scraper constructed entirely of Inconel was provided to dislodge the carbon deposit. The shaft of the scraper was made from a 0.375 in. OD tube closed at the lower end. Eight scraper blades, formed from 16-gage sheet, were welded to the shaft. The blades were 0.5 in. wide and were spaced 1.563 in. apart, center to center. Clearance between the leading edges of the blades and the wall of the catalyst liner was one-sixteenth inch.

The carbon scraper was operated manually by means of a cross-bar at the top end. Two O-rings in the brass cap of the reactor prevented leakage of gas. One O-ring provided a dynamic seal; the other a static seal.

The carbon dislodged by scraping was collected in a removable plastic jar at the bottom of the reactor. A Pyrex glass tube in the jar prevented direct contact between the jar and the hot carbon. The filter near the bottom of the jar consisted of a Fiberfrax pad supported on a perforated aluminum disc and held in place by the Pyrex tube. A gate valve above the collection jar permitted sealing off the reactor while the jar was being emptied.

Gas was normally discharged from the reactor through the filter located immediately below the catalyst liner. This filter simulated the hot-gas filter that would be required in an integrated oxygen regeneration system. The filter medium was a plug of stainless steel wool backed up by a plug of Fiberfrax wool.

Auxiliary equipment included individual flowmeters for the three gases, a manometer for measuring the pressure drop across the reactor, and a wet test meter for the exhaust gas. The reactor was heated in a 4-zone split-tube furnace. The power to each zone was controlled manually by means of an ammeter and a variable transformer. Temperature was measured with chromel-alumel thermocouples welded to the shell of the reactor at the center of each zone. A fifth thermocouple was placed inside the scraper shaft. Temperature variation at a particular transformer setting was usually less than $\pm 3^{\circ}\text{C}$. A photograph of the assembled apparatus is shown in Fig. 32.

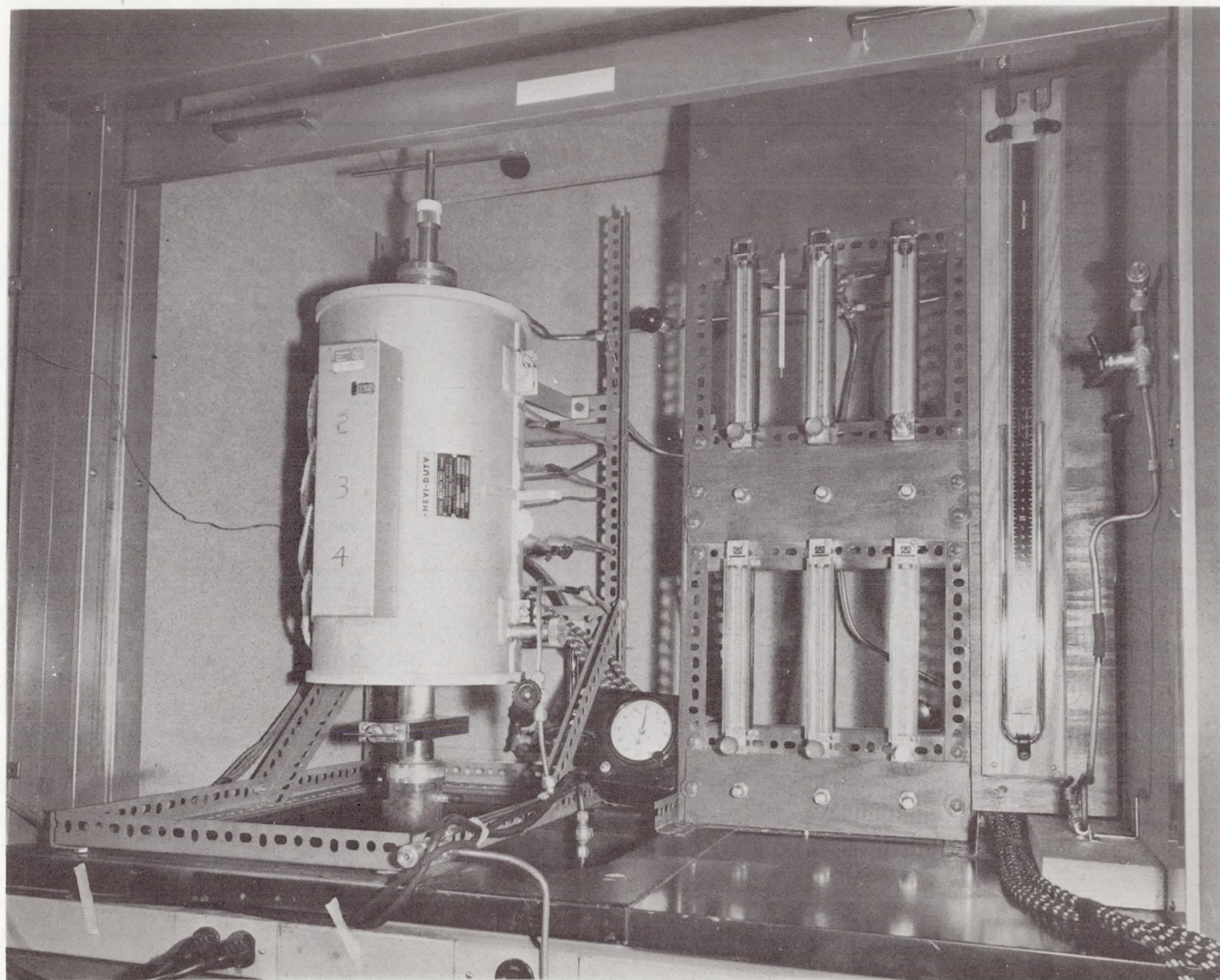


Fig. 32 - Carbon deposition reactor and
auxiliary equipment used in continuous
100-day test

3.3.2 Start Up and Procedure

The 100-day life test was started at noon on March 12, 1968. The reactor had been heated overnight at 585°C with pure CO flowing and then treated with CO and H₂ for 4 hours before adding CO₂ to the feed. The addition of CO₂ marked the starting time of the test.

After 2 days of operation conversion of CO had not reached the desired level of 60 percent, and an attempt was made to improve the activity of the catalyst by eliminating CO₂ from the feed. During the next 3 days only CO and H₂ were fed to the reactor and the conversion rate rose gradually to 78 percent. At the start of the 6th day CO₂ was again added to the feed, and during the next 50 days the operating conditions were maintained fairly constant except for one brief period when trouble was encountered. During the second half of the test, wider variations were permitted in temperature, feed rate, and gas composition.

During the greater part of the test, the gas feed consisted of 150 std cc/min of CO, 41 std cc/min of CO₂, and 6-9 std cc/min of H₂. At this input rate, carbon scraping was required only once per day. In two 4-day periods the feed rate was doubled, and in one 3-day period it was quadrupled. In these periods the scraping frequency was increased to two and three times per day to prevent plugging of the reactor.

Carbon scraping required only 2 to 3 minutes, the routine being as follows:

1. Close gas exit valve at hot gas filter and open gas exit valve at collection jar.
2. Release static seal around scraper shaft.
3. Rotate scraper five or six turns and, at the same time, screw it downward 1.5 inches to cover the spaces between the scraper blades.
4. Return scraper to starting position.
5. Tighten nut of static seal.
6. Open valve at hot gas filter and close valve at collection jar.

The scraper was normally kept in the "up" position so that the vertical movement during scraping was always downward.

Before emptying the collection jar, the carbon was allowed to cool. The gate valve above the jar was then closed and the jar removed by unscrewing the cap and the O-ring gland in the gas exit line. Only 1 to 2 minutes were needed to remove and empty the jar and replace it in the system. The gate valve was then reopened.

During each regular working day, the CO conversion rate was followed by comparing the exhaust gas rate with the input rate. Occasionally, samples of the feed gas and the exhaust gas were analyzed with a mass spectrograph. Also, occasional gravimetric determinations were made of CO₂ in the feed gas and of CO₂ and H₂O in the exhaust gas. The carbon weight was recorded for every day of operation.

3.3.3 Results of 100-Day Test

The 100-day test was successfully completed without major difficulty except for a short period in which the catalyst became temporarily deactivated. Total carbon production in the 101 test days was 4,200 grams (equivalent to a 0.155-man rate), and overall conversion of CO was 62 percent. Both carbon production and CO conversion exceeded the minimum goals that had been set for the test. Catalyst consumption was 155 g. and the carbon to catalyst-consumption ratio was 27 to 1.

The test can be divided into 23 distinct periods in which the operating conditions were essentially constant for 3 or more consecutive days. The conditions of operation and the results for the 23 periods are shown in Table XII and Fig. 33. The daily log of the test is given in Appendix F.

Carbon deposits from 36 test days were analyzed for Fe. The Fe contents ranged from 2.34 to 9.71 percent, the weighted average being 3.73 percent. The average Fe content estimated from the weight of catalyst consumed and the total carbon product was 3.47 percent.

Carbon and hydrogen contents of deposits from three test days were determined by combustion analysis. The results, together with those for Fe, were as follows:

TABLE XII
RESULTS OF 100-DAY LIFE TEST OF CARBON DEPOSITION REACTOR

Test Days	Temp., °C	Average Gas Flow Rate, cc/min ^a	Input Gas Composition, %			Average Conversion of CO, %	Carbon Rate, g/day
			CO	CO ₂	H ₂		
1-2	585	209	76.5	18.6	4.8	53.3	29.42
3-5	574	203	96.1	--	3.9	67.3	45.40
6-8	572	212	77.2	19.0	3.8	59.2	32.60
9-13	572	219	75.0	21.2	3.8	60.1	33.53
14-17	572	226	75.2	20.5	4.3	58.0	33.46
18-24	573	230	74.0	20.2	5.8	62.1	35.83
25-30	575	224	75.9	20.8	3.4	61.0	35.24
31-35	592	224	75.9	20.8	3.4	58.7	33.75
36-42	550	224	75.9	20.8	3.4	62.7	36.20
43-45	571	213	79.8	14.5	5.7	39.1	22.56
46-50	572	226	75.3	20.4	4.3	59.4	33.37
51-58	558	226	75.3	20.4	4.3	63.4	36.64
59-62	538	227	74.8	20.4	4.8	69.1	39.84
63-66	534	448	75.8	19.8	4.4	61.3	70.75
67-70	505	226	75.2	20.6	4.3	66.5	38.36
71-73	495	448	75.8	19.8	4.4	62.5	72.10
74-77	540	226	74.8	20.4	4.8	63.4	36.59
78-83	598	228	74.5	20.4	5.1	59.9	33.55
84-86	541	230	73.9	20.2	5.9	70.8	40.85
87-90	539	223	76.4	20.8	2.8	67.7	39.10
91-93	540	242	70.3	25.6	4.1	61.5	35.45
94-98	539	214	79.6	15.7	4.7	69.1	39.80
99-101	543	912	74.6	21.0	4.4	58.9	138.5

^a Flow rate at 25°C, 730 mm of Hg

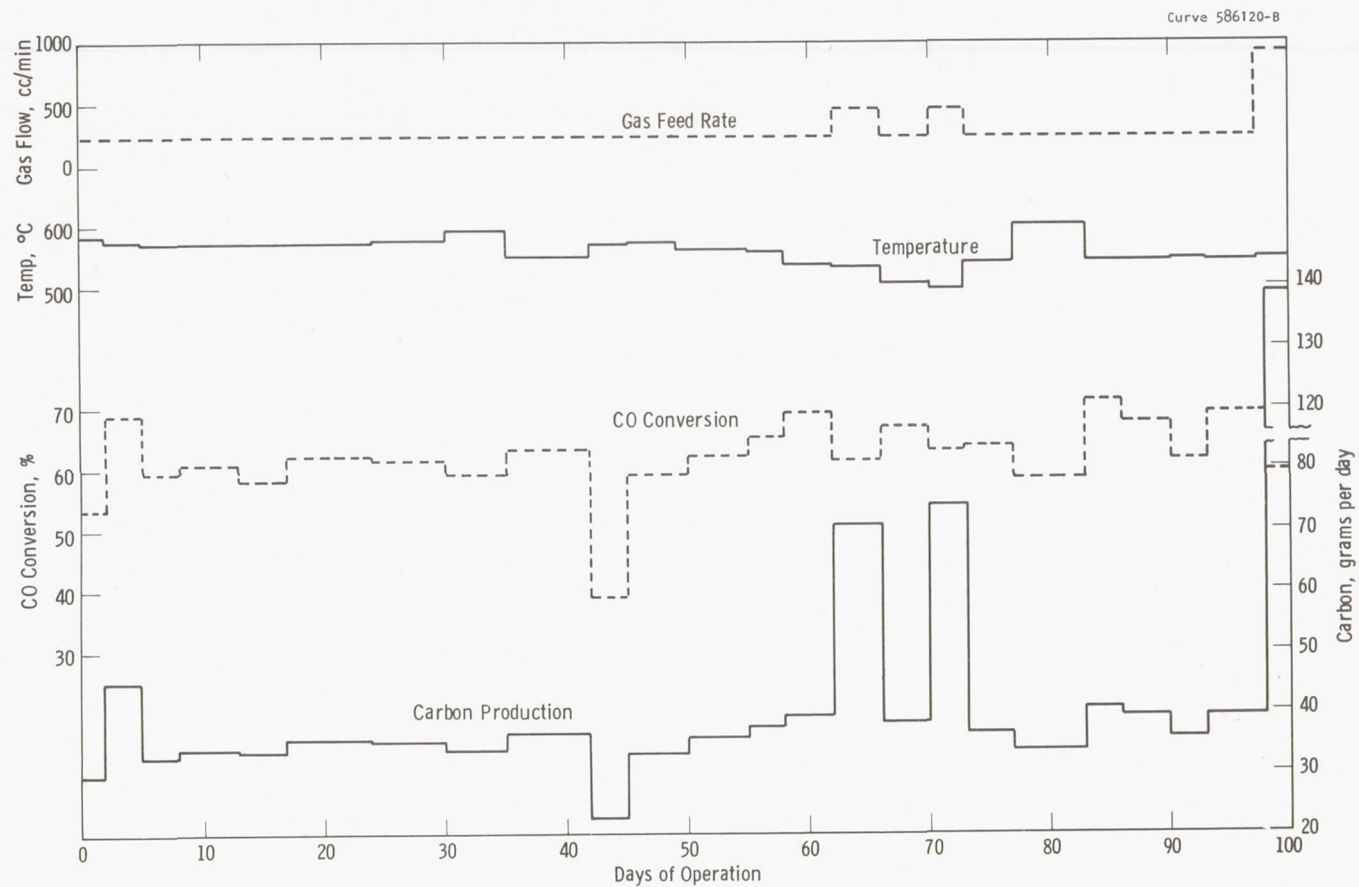


Fig. 33 - Log of 100-day life test of carbon deposition reactor

<u>Test Day</u>	<u>55</u>	<u>67</u>	<u>70</u>
Carbon, percent	93.1	95.0	94.0
Hydrogen, percent	0.60	0.77	0.52
Iron, percent	<u>4.71</u>	<u>3.37</u>	<u>2.64</u>
Total	98.41	99.14	97.16

None of the analyses add to 100 percent. The missing constituent is probably oxygen, which may have been present as adsorbed water. Ash determinations that were made as part of the analytical procedure for Fe indicated that no inert constituent other than Fe was present.

On the basis of the above analyses, a rounded value of 94 percent was taken as the carbon content of the reactor deposits. This value was used in calculating the daily carbon production and the average conversion of CO. Spot checks of CO conversion by gravimetric analysis of the input and output gases for CO₂ agreed well with the value based on carbon production. However, conversion rates calculated from the change in gas volume were almost always on the high side, even after correcting for the conversion of H₂ to H₂O, probably because of adsorption of gas by the carbon deposit.

The only difficulty of any consequence in the test occurred on days 43-45. On the 43rd day, the conversion rate of CO began to fall and reached virtually zero at the end of the 44th day. At this point, corrective action was taken, which consisted of eliminating CO₂ in the feed and increasing the H₂ concentration to 15 percent.

Almost immediately the conversion rate began to rise slowly, and the improvement accelerated with time. The treatment with the high-H₂, CO₂-free feed was continued for 24 hours, at which time the conversion had reached 73 percent. At the start of the 46th day, CO₂ was again added to the feed, and the H₂ input was returned to its normal value. No further trouble was encountered thereafter.

The loss of conversion was apparently caused by accidental poisoning of the catalyst while sampling the input gas for mass spectrographic analysis. An 80 cc gas sample bottle had been placed in the

gas feed line (in a bypass provided for this purpose) without prior purging of the bottle. It could not be determined what gas had been present in the bottle, but analysis of the sample showed the presence of a trace of SO_2 . It was concluded, therefore, that sulfur poisoning of the catalyst had occurred and that reactivation was achieved by the action taken.

3.3.3.1 Description of Carbon

The carbon product of the reactor was completely dry and contained very little dust. Thirty-five to 40 percent of its particles were larger than 9 mesh; about 90 percent were larger than 48 mesh, and only 3 percent or less were finer than 100 mesh. When the carbon fell into the receiving jar, the fine particles settled almost immediately.

No difficulty in filtering the carbon was encountered, and only a few grams of carbon in the entire test passed through the filter and settled in the gas discharge line. The stainless steel wool plug in the hot gas outlet became filled with carbon, and the carbon itself apparently served as the filter medium. Replacement of the filter plug was not necessary during the test.

There was no evidence of gas-borne carbon at the outlet of the gas discharge line. The water in the wet test meter stayed free of carbon dust, and no carbon dust was observed in the absorption bottles used for gas analysis.

The bulk density of the carbon product varied between 0.3 and 0.4 g/cm^3 . X-ray diffraction analysis revealed that the carbon was graphitic and that the iron was present as Fe_3C .

A photograph of a typical deposit as discharged from the reactor is shown in Figure 34.

3.3.3.2 Condition of Catalyst Liner at End of Test

Approximately 1.2 cu. in. of the catalyst liner was consumed during the test. Maximum attack occurred at the center of the first furnace zone where the reactor reached full temperature. The liner was



Fig. 34 - Carbon produced on 74th day of continuous 100-day test.

completely eaten away at this point and a short section of the stainless steel shell was exposed. Over the next six inches catalyst consumption gradually diminished, and the liner returned almost to its original thickness. For two inches beyond this point, very little catalyst was consumed. However, near the end of the liner, a new zone of attack appeared which closely corresponded to the zone of decreasing temperature. This second reaction appeared to reach its maximum rate at a temperature about 50°C below that of the main reaction zone. Profiles of the liner thickness and of temperature within the reactor (taken inside the scraper shaft) are shown in Fig. 35. Photographs of the reactor after being cut in half lengthwise are presented in Figs. 36, 37, and 38.

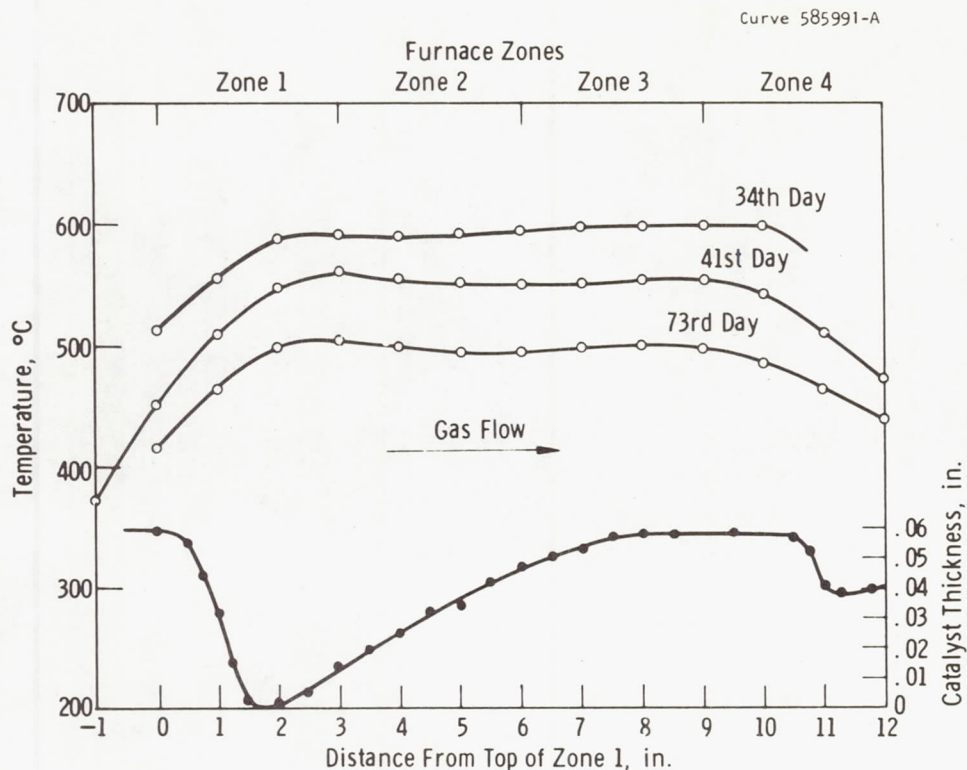


Fig. 35 - Temperature profiles in carbon deposition reactor and variation of catalyst wall thickness with length at end of test

In the second reaction zone at the end of the catalyst liner, carbon formed behind the liner, forcing it inward and producing the distortion that is visible in Fig. 38. Distortion of the liner prevented full rotation of the carbon scraper when the scraper was in its lowest position. It did not prevent discharge of the carbon, however, and was never a serious problem. Interference with the scraper was first noticed about midway of the test.

The most probable explanation of the second carbon producing zone at the outlet end of the reactor is the following: During most of the test the operating temperature (temperature of the uniformly heated zone of the reactor) was above the optimum temperature for the

reaction, and carbon precipitation at this temperature had virtually ceased by the time the gas stream reached the center of zone 3. However, when the gas passed into the lower temperature zone at the end of the reactor, further reaction occurred.

3.3.3.3 Condition of Carbon Scraper

Practically no chemical attack occurred on the carbon scraper, the weight loss being only 0.3 gram out of a total weight of 395 gram. The scraper catalyzed carbon precipitation, however. Flakes from the lower end of the scraper were observed several times in the carbon product and the scraper was heavily coated with carbon at the end of the test. Furthermore, carbon had formed between the blades and the shaft (the blades were welded to the shaft on only three sides), causing partial rupture of the welds of two blades.

Rupturing of the blade welds caused no difficulty in the 100-day test. The problem can be avoided, however, by welding the blades on all sides so that no

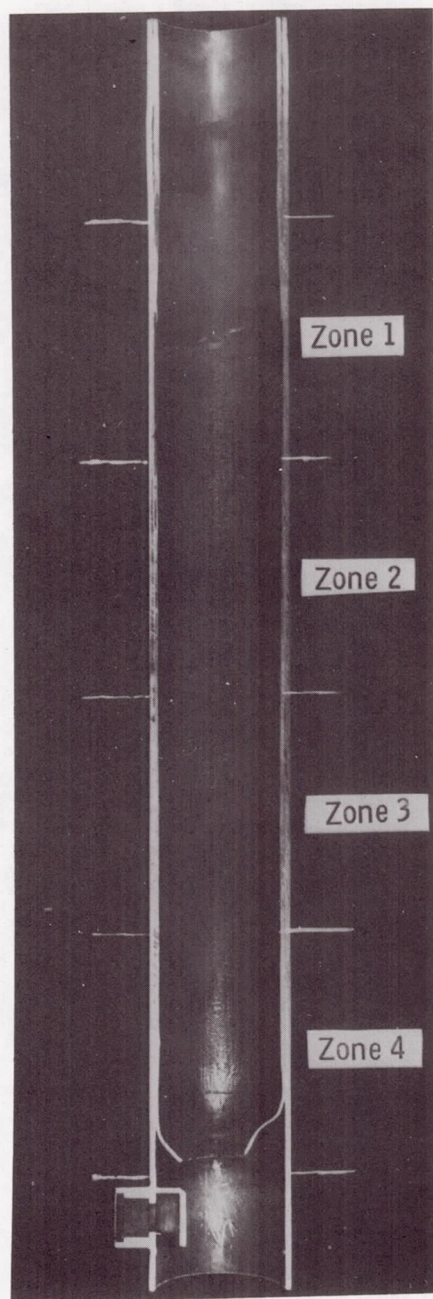


Fig. 36 - Section through carbon deposition reactor at end of 100-day test.

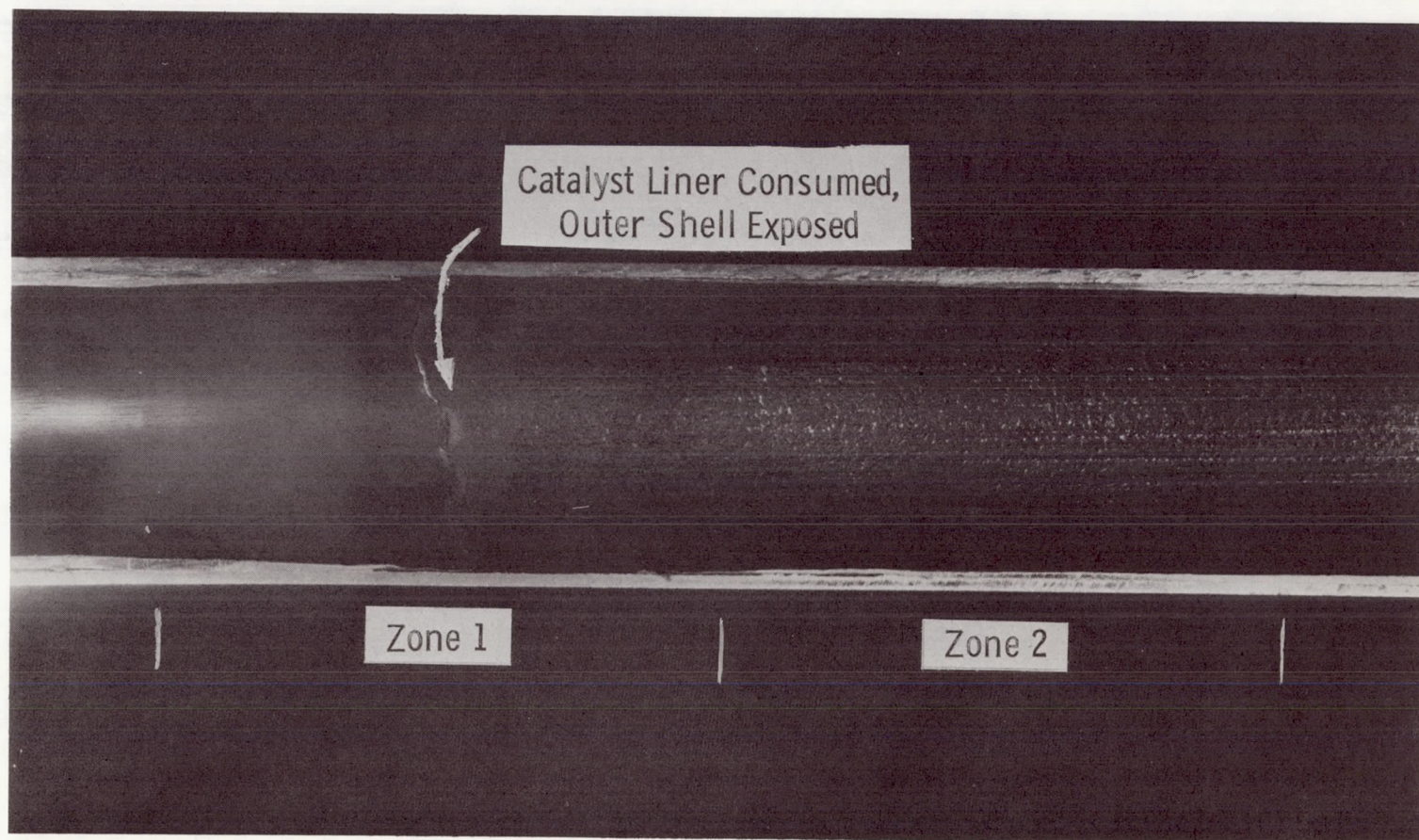


Fig. 37 - View of inlet end of carbon deposition reactor,
showing region of maximum corrosion of catalyst liner

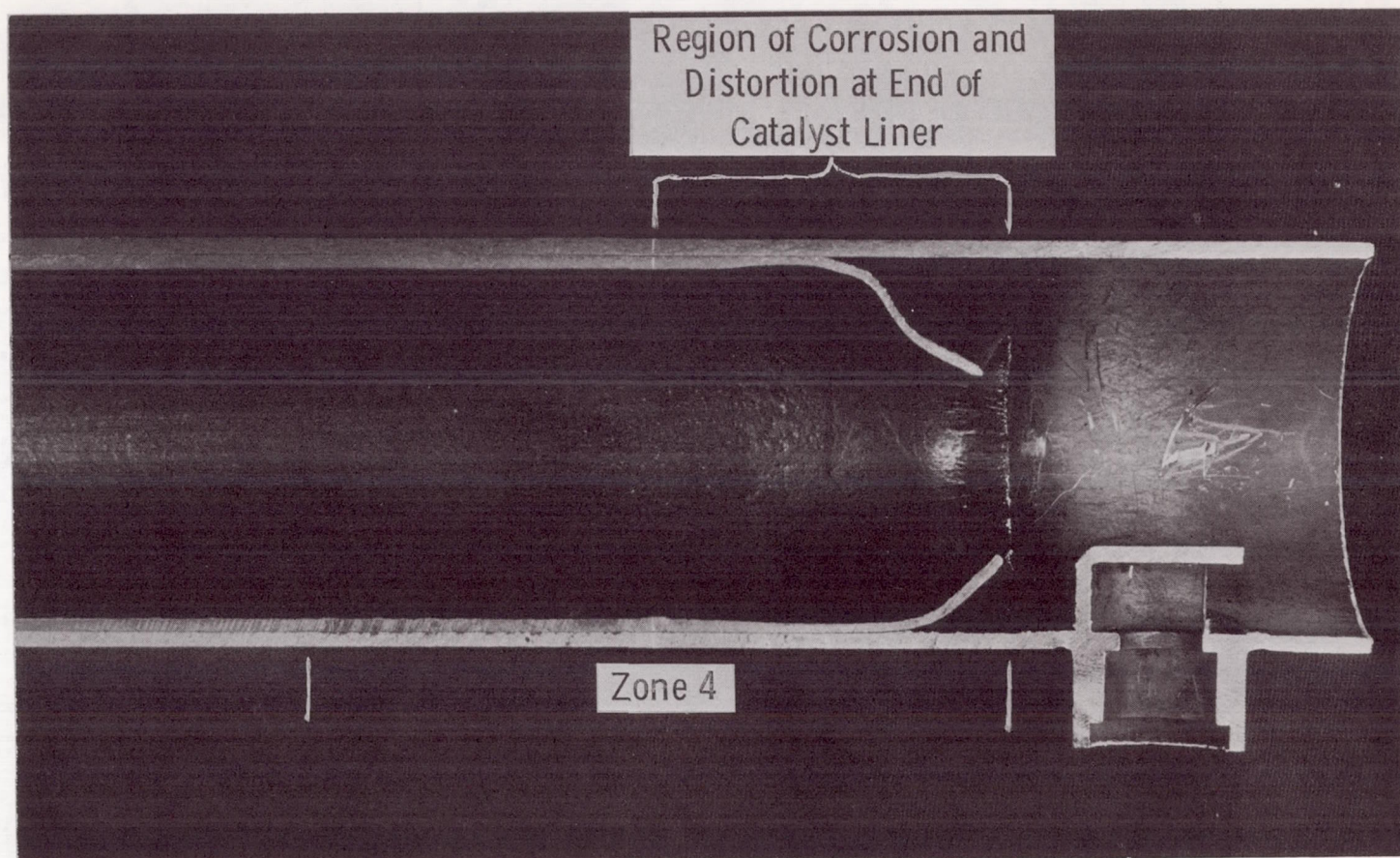


Fig. 38 - View of gas outlet end of carbon deposition reactor

narrow spaces are available for carbon buildup. A second solution is one piece construction.

3.3.3.4 Conversion of H₂ to H₂O

The extent of conversion of H₂ to H₂O in the reactor was determined gravimetrically by means of a water absorption bottle in the exhaust gas line. A 30-minute sampling time was used. The proportion of the H₂ input that was converted to H₂O ranged from 18 to 26 percent and was temperature dependent.

The results of 14 analyses made on different days are summarized in Table XIII and compared with conversions predicted from the water gas shift reaction:

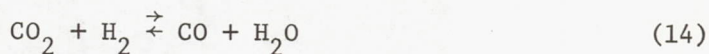


TABLE XIII
CONVERSION OF H₂ TO H₂O IN CARBON
DEPOSITION REACTOR AND COMPARISON
WITH PREDICTED CONVERSION

Temperature, °C	No. of Determinations	Range of Conversion, %	Average Conversion, %	Predicted Conversion, %
492 - 499	2	17.8 - 19.0	18.4	25.4
539 - 547	8	22.0 - 25.5	23.5	31.2
595 - 601	4	24.5 - 26.1	25.5	35.8

The observed conversions of H₂ were about 25 percent lower than the predicted values, indicating that either the reaction did not reach the equilibrium corresponding to the reactor temperature or it shifted to equilibrium at some lower temperature as the gas passed through the temperature gradient at the end of the reactor.

3.3.3.5 Hydrocarbon Formation in Reactor

Metals that catalyze carbon precipitation also catalyze the formation of methane and other hydrocarbons from CO and H₂. The presence of hydrocarbons in the product gas of the carbon deposition reactor is undesirable because of the danger of cracking of the hydrocarbons to form carbon deposits in the heat exchanger or the electrolysis battery where the temperature is higher. Hydrocarbons could also react with CO₂ and lower the concentration of CO₂ in the battery feed. Because of these possible detrimental effects, the hydrocarbon concentration should be low, although the maximum concentration that can be tolerated is not known. In general, hydrocarbon formation is favored by high H₂ concentration and low temperature.

Hydrocarbon formation during the 100-day test was checked by mass spectrographic analysis. Six samples of the effluent gas from different days were analyzed. Methane was the only hydrocarbon detected. The results are shown in Table XIV.

TABLE XIV
METHANE FORMATION IN CARBON DEPOSITION REACTOR

Test Day	Temp, °C	H ₂ in Feed, percent	Composition of Product Gas, percent			
			CO	CO ₂	H ₂	CH ₄
20	571	5.9	37.6	55.7	6.2	0.20
34	595	3.2	38.0	55.5	2.8	0.05
42	545	3.6	35.9	59.6	4.4	0.10
53	564	4.4	36.5	58.7	4.6	0.13
73	499	4.4	33.9	62.6	3.5	0.05
93	540	4.4	33.4	61.8	4.6	0.14

The average of the six determinations of CH₄ was 0.11 percent. The highest CH₄ concentration corresponded to the highest H₂ input rate and one of the two lowest concentrations corresponded to the lowest H₂ input rate (test day 34). The other low value occurred on test day 73 when the gas feed rate to the reactor was double the normal rate. There was no obvious correlation with temperature.

3.3.3.6 Effect of H₂ on Carbon Deposition Rate

The H₂ concentration in the feed gas in the 100-day test ranged from 2.7 to 5.9 percent. Analysis of the data shows that the rate of carbon deposition increased with increasing H₂ concentration. Plots of conversion of CO versus H₂ concentration at constant CO and CO₂ input and at two levels of temperature are shown in Fig. 39. The slopes of the two plots indicate that CO conversion increased by about 1 percent of each 1 percent increase in the H₂ concentration.

3.3.4 Development of Mathematical Model for Carbon Deposition

Although the 100-day test was not intended to be a kinetic study, the geometry of the reactor suggested that the reaction might be gas diffusion controlled and a reaction model was developed on this premise. The model was based on the assumptions that the reaction

of CO at the catalyst surface was rapid compared to the rate of diffusion in the gas phase and that the gas composition at the surface closely approached equilibrium. Haas and co-workers¹⁰ reported that thermodynamic equilibrium was reached almost instantaneously with a packed bed reactor and iron catalyst when H₂ was present in the feed.

A material balance for CO over a differential reactor element of length dZ gave the following relationship.

$$\bar{F} \frac{dX}{dZ} = -k_m \pi D (X - X_e) \quad (15)$$

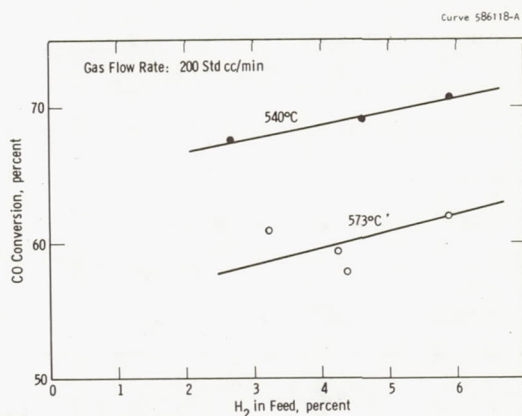


Fig. 39 - Variation of CO conversion with H₂ content of feed gas

where X = bulk mole fraction of CO

X_e = equilibrium mole fraction of CO

D = diameter of catalyst tube, cm

\bar{F} = average flow rate of gas at reactor temperature and pressure, cc/sec

Z = distance along reaction zone, cm

k_m = mass transfer coefficient, $\frac{\text{cc}}{\text{cm}^2 \text{ sec}}$

On integration the relationship becomes

$$\ln \frac{X - X_e}{X_o - X_e} = - \frac{k_m \pi D}{\bar{F}} Z \quad (16)$$

Where X_o is the initial concentration of CO.

The profile of the catalyst tube (see Fig. 35) was used to evaluate k_m , the assumption being made that the weight of carbon deposited, or moles of CO reacted, in a length ΔZ was proportional to the weight of Fe consumed in that length. By integrating the area above the curve, the fraction of CO that reacted in each 0.5-in. segment along the uniform temperature zone was calculated. Making the further assumption that the reaction was only 95 percent complete at the exit of the reactor, each fraction was multiplied by 0.95 and the result subtracted from

unity to give the corresponding value for $\frac{X - X_e}{X_o - X_e}$. The logarithms of

these values were then plotted against Z , as shown in Fig. 40.

The plot was not a straight line probably because the flow rate decreased with length, as CO was consumed, and because the build-up of the carbon layer tended to move the main reaction zone down the tube. Both factors would cause a greater reaction at the lower end of the reactor than predicted by the model which assumes constant F and k_m along the length. The slope of the curve was read at the point

where the flow was equal to \bar{F} , that is, where half of the total conversion of CO had occurred. Placing the slope equal to

$$\frac{-k_m \pi D}{\bar{F}} \text{ and using the average}$$

flow for the entire test for \bar{F} (10.6 cc/sec at 554°C, 730 mmHg), k_m was found to be 0.14 cc/cm²-sec.

Data from the low flow rate periods cannot be used to test the model because the gas left the reactor at nearly equilibrium composition and the full length of the reactor was not utilized. (This is well illustrated by the results of test

days 91-93, when X_0 was 0.70, and of test days 94-98 when X_0 was 0.80. The conversions of CO in the two periods were 61.5 percent and 69.1 percent respectively. Both conversions correspond to $X = 0.34$ in the exit gas). However, the data acquired during test days 99-101, when the flow rate was four times the usual rate, should be suitable. The value of X from the test and $X_e = 0.34$ from the low flow rate periods were used together with the reactor length and diameter to calculate k_m . To allow for the fact that a substantial part of the reaction occurred in the nonuniform temperature zone at the entrance end of the reactor, an equivalent length of this zone was calculated, using the information supplied by the catalyst profile. The equivalent length was 1.9 cm, and the corrected length of the reaction zone was 27.3 cm.

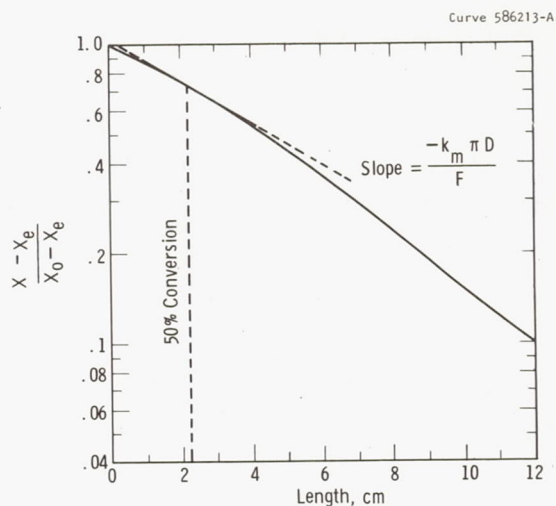


Fig. 40 - Plot of $\frac{X - X_e}{X_0 - X_e}$ versus distance along reactor in uniform temperature zone

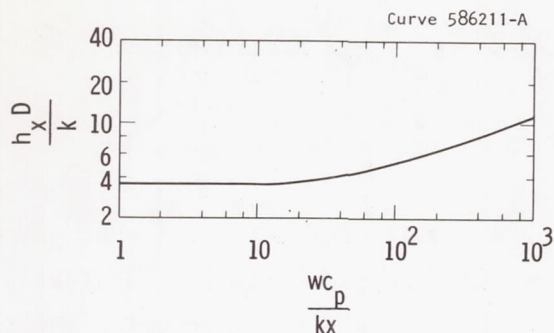


Fig. 41 - Predicted local Nusselt numbers plotted vs local Graetz numbers for parabolic velocity profile and uniform wall temperature after McAdams¹⁶ p 233

The Graetz number, along the horizontal axis, can be transformed into the group

$$\frac{F}{D_{12}L}, \text{ where}$$

L = length of reaction zone, cm

D_{12} = diffusivity, cm^2/sec

The diffusivity for CO-CO_2 mixtures at 0°C , and 760 mm Hg is $0.136 \text{ cm}^2/\text{sec}$ and the temperature dependence is given by the relation¹⁷

$$D_T = D_{12} \left(\frac{T}{288.2} \right)^{1.75} = 0.858 \text{ cm}^2/\text{sec at } 554^\circ\text{C}. \quad (18)$$

The flow conditions in the carbon deposition test corresponded to

$$\frac{F}{D_{12}L} = \frac{10.6}{0.858 \times 27.3} = 0.45$$

The results of the calculation of k_m were as follows:

$$\ln \frac{.392 - .340}{.745 - .340} = -k_m \times \frac{\pi \times 3.81 \times 27.3}{37.1}$$

$$k_m = 0.23 \text{ cc/cm}^2 - \text{sec}$$

The lower value for k_m ($0.14 \text{ cc/cm}^2 - \text{sec}$) that was estimated from catalyst consumption reflects the fact that the catalyst profile was representative mainly of low flow rate tests in which the full reactor length was not utilized and the buildup of the carbon layer was very nonuniform. At higher flows, on the other hand, more of the reactor was used and the carbon layer was distributed more uniformly with length.

To better understand the influence of the carbon layer, the total resistance to mass transfer in the gas phase can be separated into two resistances in series, as follows:

$$\frac{1}{k_m} = \frac{1}{k_g} + \frac{1}{k_c} \quad (17)$$

where k_g = mass transfer coefficient for gas phase diffusion to the carbon surface

and k_c = mass transfer coefficient for diffusion through the carbon layer

The coefficient k_g can be calculated by analogy with heat transfer theory for fluid flow in tubes, the "Graetz Problem", assuming a parabolic velocity profile.¹⁶ The method makes use of two dimensionless groups which have the relationship shown in Fig. 41. The Nusselt number, on the vertical axis, can be transformed into the equivalent

group $\frac{k D}{D_{12}}$, where D_{12} is the diffusivity of CO in the flowing gas mixture.

This point lies far into the asymptotic region on the left hand side of the plot in Fig. 41 where the value for $\frac{k_g D}{D_{12}}$ is 3.5.

Solving for k_g

$$k_g = \frac{3.5 D_{12}}{D} = \frac{3.5 \times 0.858}{3.81} = 0.79 \text{ cc/cm}^2 - \text{sec}$$

The coefficient for mass transfer through the carbon layer is related to diffusivity in the following way:

$$k_c = \frac{D_{12} \text{ POR}}{X_c \tau} \quad (19)$$

where POR = porosity of the carbon deposit

X_c = thickness of the deposit, cm

τ = tortuosity of the pore structure

The average carbon thickness, assuming uniform distribution, was of the order of 0.32 cm and the porosity of the deposit was about 0.6. Tortuosity factors usually fall in the range of 1.5 to 5. Using a value of 2.0, k_c is found to be $1.07 \text{ cc/cm}^2 - \text{sec}$. Combining the two resistances and solving for k_m gives $0.49 \text{ cc/cm}^2 - \text{sec}$ for the mass transfer coefficient.

The results of this calculation show that the rate of mass transfer by gas phase diffusion is greater than that indicated by the experiment and suggests that some other resistance to reaction is controlling. Others¹⁰ have suggested that the rate controlling process is diffusion of iron atoms through an Fe_3C layer on the catalyst surface. The data in the present work are insufficient to evaluate this possibility.

3.3.4.1 Effect of Temperature on Carbon Deposition

The effect of temperature on conversion of CO in the low flow rate test periods is shown in Fig. 42. The temperature of maximum conversion was not defined exactly but, by interpolation, appears to be in the vicinity of 520°C.

Although only one test period was run at a temperature below 520°C, the general shape of the curve is confirmed by the fact that very little carbon deposition occurred below 450°C. Thus, in Fig. 35, the first evidence of attack on the catalyst tube corresponds to a temperature of about 450°C on the reactor temperature profile for the 41st day. The reactor temperature on this day was near the average temperature for the 100 days.

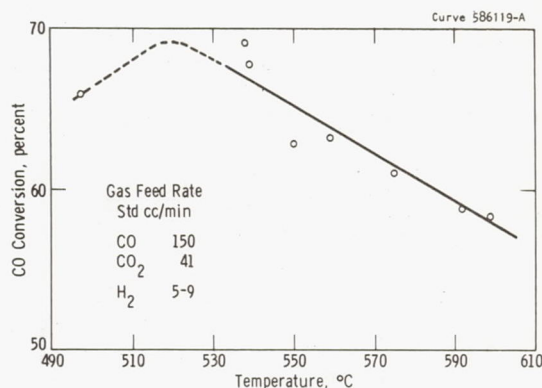


Fig. 42 - Effect of temperature on CO conversion

At temperatures below the peak of the curve, the rate of reaction was probably controlled by the kinetics at the surface, whereas at higher temperatures the conversion of CO was apparently limited by equilibrium. The temperature dependence of the equilibrium constant in the latter temperature range is shown in Fig. 43 by a plot of $\ln K_p$ vs $1/T$, where K_p is defined as follows:



$$K_p = \frac{P_{\text{CO}_2}}{(P_{\text{CO}})^2} \quad (20)$$

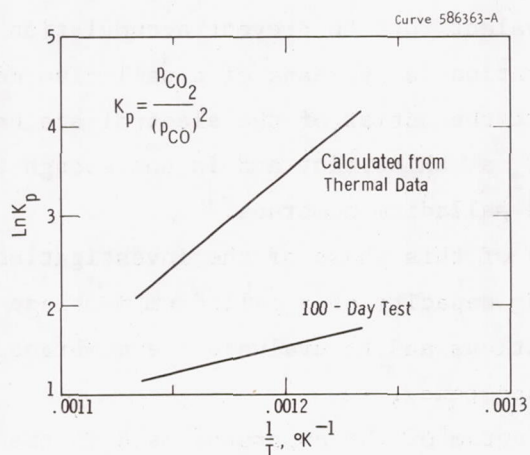


Fig. 43 - Temperature dependence of $p_{CO_2} / (p_{CO})^2$ in low flow rate tests compared with the reaction equilibrium constant

Also shown is the corresponding plot calculated from published thermal data. The fact that the two plots do not agree indicates that the observed equilibrium condition in the experiment was not that for the reaction represented by Equation 3. Additional experiments are needed to explain these results.

4. HYDROGEN SEPARATION STUDY

The H_2O input rate to an integrated oxygen regeneration system will be of the order of 0.2 mole per hour per man, and H_2 must be separated at an equivalent rate to prevent accumulation of H_2 . The proposed method of separation is by means of a palladium membrane in the recycle gas stream at the outlet of the electrolysis battery. The recycle gas is rich in H_2 at this point and is hot enough to prevent carbon deposition on the palladium membrane.

The objectives of this phase of the investigation were to measure the H_2 separating capacity of a palladium membrane at the proposed operating conditions and to evaluate the membrane in regard to stability and life expectancy.

A schematic diagram of the apparatus used in the study is shown in Figure 44. The palladium membrane was in the form of a closed-end tube 0.125 in. O.D. by 9 in. long. Its wall thickness was 0.005 in. The open end of the tube was copper brazed to a larger Inconel tube which served as a support and as an outlet to the vacuum line. The palladium tube was suspended in the center of a clear quartz tube, and the assembly was heated by means of a 4-zone split-tube furnace. The entire length of the palladium tube was located in the uniform temperature zone.

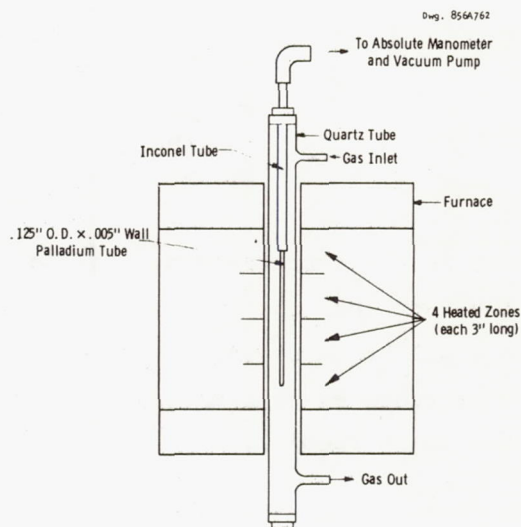


Fig. 44 - Schematic diagram of H_2 diffusion apparatus

Auxiliary equipment was similar to that used with the carbon deposition reactor. It included individual flowmeters for CO, CO₂ and H₂ and thermocouples outside the quartz tube at the center of each furnace zone. Uniformity of temperature within the reactor was checked with a probe thermocouple prior to conducting the H₂ diffusion measurements.

4.1 Experimental Procedure

The gas mixture containing H₂, CO, and CO₂ was passed into the quartz reactor at a constant rate and the exit gas flow was carefully measured with a wet test meter and stop watch. Measurements were made with and without vacuum in the palladium tube. The difference between these two rates, after correction for volume changes due to chemical reaction, represented the rate of H₂ loss to vacuum.

In some of the experiments a water absorption bottle was placed in the exit gas line to measure the net conversion of H₂ to H₂O resulting from the water gas shift reaction. Measurements of the exit gas rate with and without vacuum, but with no H₂ in the feed, showed that the palladium tube was gas tight to CO and CO₂.

4.2 Results

The H₂ diffusion experiments were conducted over a 20-day period during which the palladium tube was continuously heated and exposed to a flowing stream of CO, CO₂, and H₂ at temperatures ranging from 700 to 950°C. The ratio of CO to CO₂ in the feed gas was fixed at approximately 4 to 1. The H₂ concentration was varied in 3 percent steps from 3 to 12 percent. The total flow rate ranged from 200 to 1000 cc/min.

No structural change in the palladium tube was evident at the end of the 20-day period. The tube remained straight and free of distortion and was not discolored or otherwise affected in surface appearance. Furthermore, its permeability to H₂ did not vary with time.

At 700°C, carbon deposited on the tube but at a very low rate. The entire tube darkened in color and small filaments of carbon

formed at random on the surface. On increasing the temperature to 750°C, partial clearing of the surface occurred. On heating to 800°C, the carbon film completely disappeared, and the original appearance of the tube was restored.

Because the rate of H_2 removal was measured by a volumetric procedure, it was necessary that the rate of H_2 conversion to H_2O also be determined. It was expected that the water gas shift reaction would rapidly reach equilibrium near the feed end of the tube, and that the H_2O formed would be converted, in part, back to H_2 as the H_2 concentration decreased due to diffusion through the tube. Because of the shift reaction, it was predicted that less H_2O would be found in the effluent gas with vacuum on the palladium tube than without vacuum. This prediction proved to be incorrect, however, at least in tests run at 700 and 800°C, since the same amount of water was found in the two cases.

Conversion of H_2 to H_2O was less than 2 percent of the input at 700°C and reached 5.7 percent of the input at 800°C. Because conversion was the same both with and without vacuum, no correction to the wet test meter reading was needed in calculating the rate of H_2 removal. Water determinations were made at 700°C and 800°C but not at 950°C. because of lack of time. The accuracy of the results obtained at 950°C is therefore less certain than of those obtained at the lower temperatures. At the higher temperature the rate of reaction is faster and equilibrium has moved toward a higher conversion of H_2 to H_2O .

The results obtained for H_2 removal are shown in Figure 45 as a function of gas flow rate, H_2 concentration, and temperature. The expected effects of flow rate and concentration were observed, that is, the H_2 removal rate increased with H_2 concentration and with flow rate but leveled off as the flow was increased. The effect of temperature did not agree, however, with previously published data^{18,19,20}

which show that the permeation rate increases with temperature. In the present work, almost no temperature effect was observed. This anomalous behavior may be related to the occurrence of the water gas shift reaction at the surface of the palladium tube simultaneously with the absorption and diffusion of H_2 , especially at higher temperatures. Further investigation will be required before the nature of the interference can be ascertained.

Although the experiments were only preliminary in nature, they showed that palladium stands up well under the conditions of operation and that a tube of the size used (22 cm^2 in surface area) is capable of removing hydrogen at a one-half man rate. The results also suggest that the use of thinner tubes may be feasible, in which case, higher permeation rates can be achieved. At 800°C , the permeability of palladium to H_2

$$\text{was } 1.46 \frac{\text{cm}^3 \text{ mm}}{\text{cm}^2 \sqrt{\text{atm}}}.$$

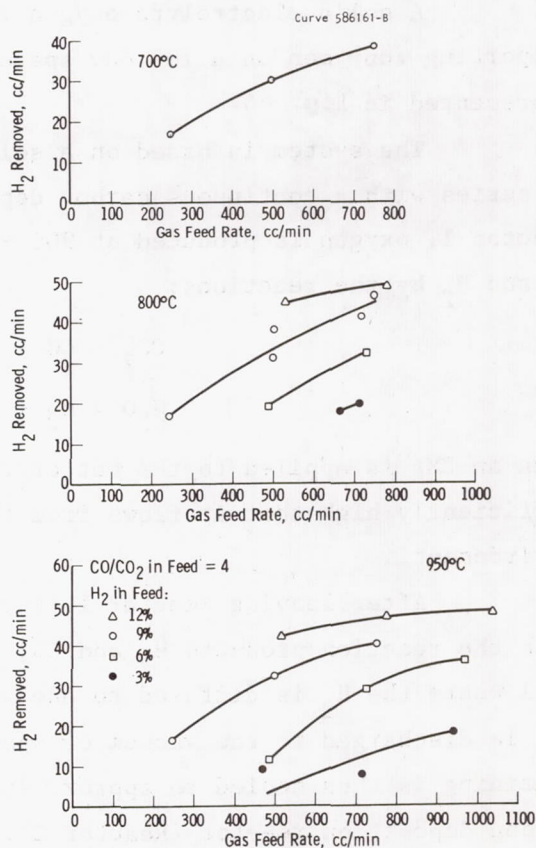
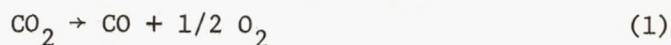


Fig. 45 - Results of H_2 diffusion study with palladium tube

5. SYSTEMS ANALYSIS - AN INTEGRATED OXYGEN REGENERATION SYSTEM

A solid electrolyte oxygen regeneration system capable of supporting four men on a 100 day space mission is schematically represented in Fig. 46.

The system is based on a solid electrolyte battery (Reactor 1) in series with a continuous carbon deposition reactor (Reactor 2). In Reactor 1, oxygen is produced at 900 - 1000°C from a mixture of CO₂, H₂O, CO and H₂ by the reactions:



when an EMF is applied to the battery. The O₂ is produced at a pressure sufficiently high that it flows from the reactor into the cabin environment.

After leaving Reactor 1, the unreacted CO₂ and H₂O, along with the reaction products H₂ and CO, pass through a palladium diffusion cell where the H₂ is diffused to one side of the palladium membrane and is discharged to the vacuum of space. The CO₂, H₂O, CO and H₂ remaining is then cooled to approximately 540°C and passed into the carbon deposition reactor (Reactor 2).

The reaction:



takes place in the presence of an iron catalyst (which forms the wall of Reactor 2). The solid carbon formed is periodically removed and the CO₂ is recycled to Reactor 1.

The feed stream to the system consists of a CO₂-H₂O mixture adsorbed in a concentrator from the cabin atmosphere. This stream is subsequently mixed with the recycle stream from Reactor 2 before it is fed to Reactor 1. Since the solid electrolyte cells can decompose

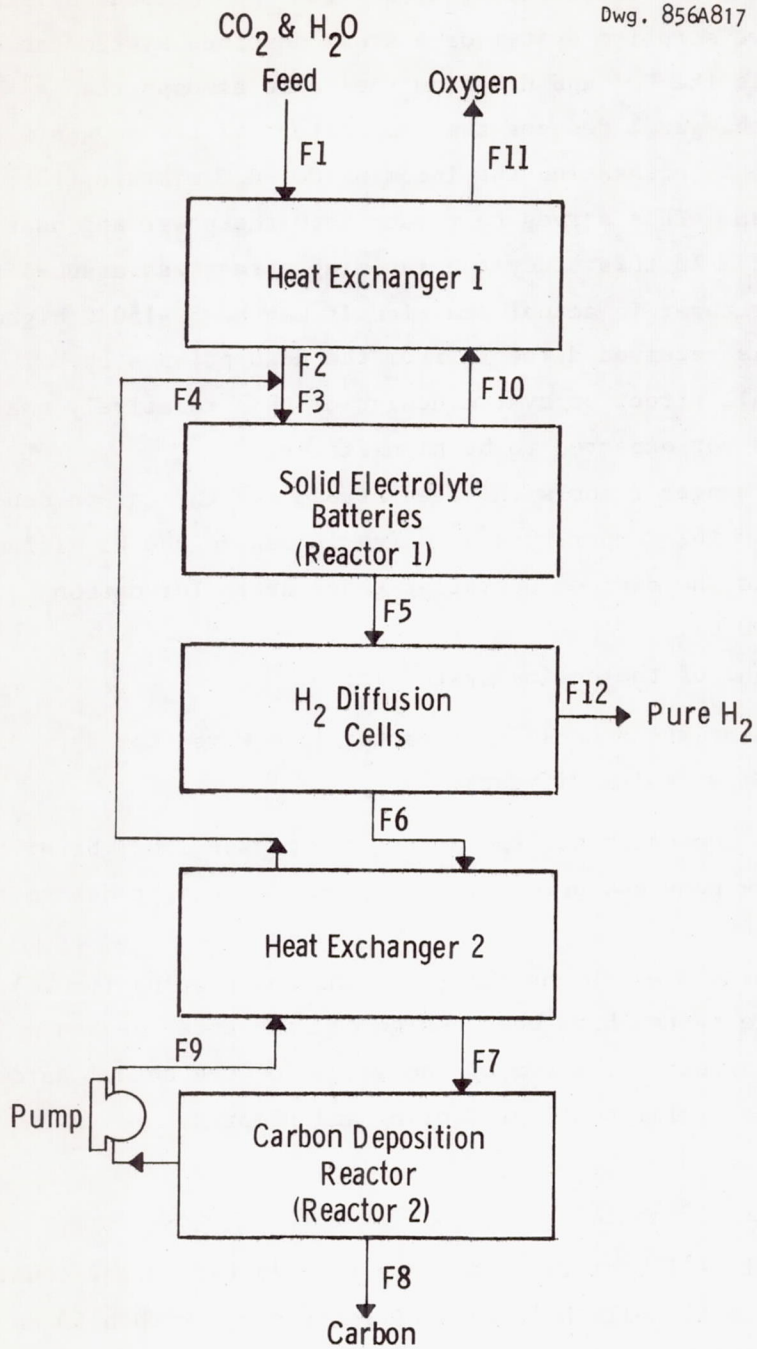


Fig. 46 - Flow diagram of oxygen regeneration system

a $\text{H}_2\text{O}-\text{CO}_2$ mixture of any composition, either the conventional silica gel-molecular sieve sorption system or a steam desorbed system can be used to concentrate the CO_2 and H_2O from the cabin atmosphere.

Heat Exchanger 1 reduces the temperature of the oxygen sent to the space cabin by preheating the incoming $\text{CO}_2-\text{H}_2\text{O}$ mixture from the sorption system. This serves to reduce both the power and heat transfer penalties. In this study the incoming stream was assumed to be at cabin temperature; in actual practice it may be 50-150°C higher than this, if it is received directly from the desorption step. However, the overall effect on system design of this relatively small enthalpy change is not expected to be significant.

Heat Exchanger 2 cools the feed stream for the carbon deposition reactor from the temperature at which it leaves the H_2 diffusion cell (850-950°C) to the desired operating temperature for carbon deposition (500-600°C).

The weight of the entire system is:

$$\begin{aligned} \text{WS} = & \text{W(heat exchangers)} + \text{W(reactor 1)} + \text{W(reactor 2)} \\ & + \text{W(palladium diffuser)} \end{aligned} \quad (21)$$

The weight of each component has two parts: the physical weight of the hardware, including pump and power supplies, and the weight due to penalties.

Weight penalties for heating, cooling and pumping (power) requirements of the system have been assigned. The total design weight of the system is therefore the sum of the weight of the actual hardware and the weight penalty for heating, cooling and pumping.

5.1 The Electrolysis Battery

The multi-cell battery design employed in this study consists of a number of tubes of cells held in position and fed with a $\text{CO}_2-\text{H}_2\text{O}$ mixture by a metallic base plate. Each tube consists of cells plus a

base tube and end cap. Each cell in each tube has a diameter D , an effective length L_e , and an overall length L . (See Figure 47.)

Dwg. 856A836

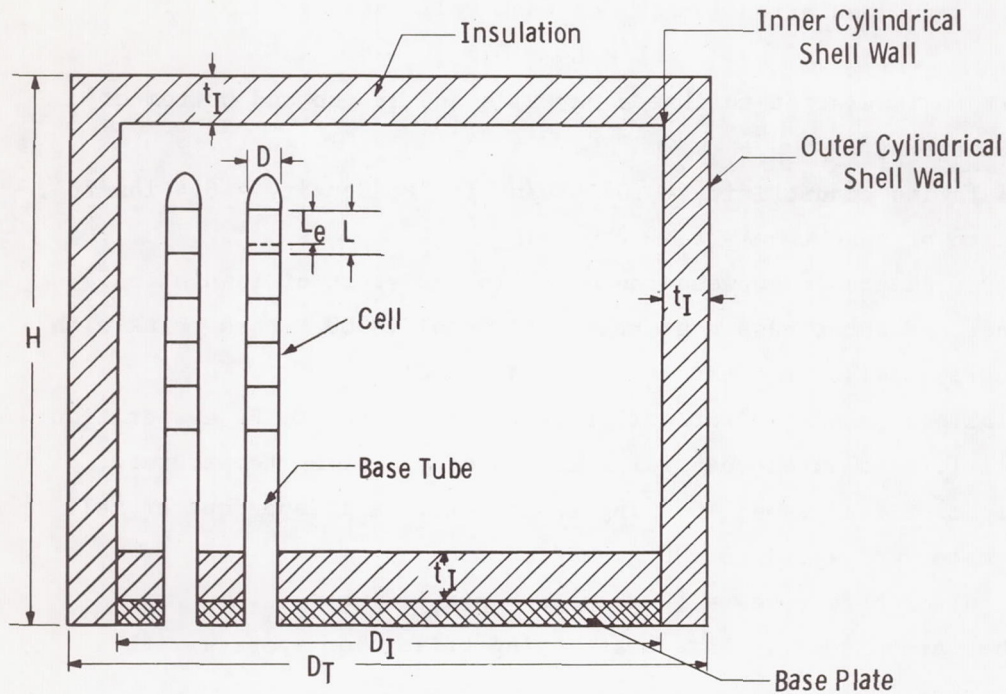


Fig. 47-Schematic cross section of electrolysis battery

The tubes of cells are enclosed in a cylindrical shell and insulated with a thickness of insulation t_I to prevent excessive heat loss.

The battery contains sufficient cells and tubes to obtain a reliability exceeding 0.99. When one tube of cells fails, it can be removed from the circuit by an external shunt and replaced by one of the spare tubes already inside the battery for this purpose. The number of cells required to provide 8 lbs of oxygen per day for the 4 astronauts is S ; the total number in the battery S_{TOT} . Similarly the number of tubes required to provide the oxygen at any one time is indicated by n_T , the number of spare tubes in the battery by n_S , and the total number by n_{TOT} .

To reduce the optimization problem to manageable size, a number of assumptions regarding cell geometry, insulation geometry, physical properties and electrical properties were made. These assumptions were:

1. Joint and insulation length for each cell equal to 0.5 cm:

$$L = L_e + 0.5$$

2. Uniform insulation thickness on walls and at top and bottom of battery, t_I .
3. Insulation conductivity = .05 BTU/hr ft °F; density = 6.4 lbs/ft³.
4. Length of base tube = $t_I + 2.0$ cm.
5. One cm clearance between top of cells and start of insulation.
6. Inner and outer case constructed of metal .0508 inches thick with density similar to that of stainless steel.
7. Principal mechanism for cell failure is related to Pt evaporation; cell life is an exponential function of operating temperature.
8. Weight of feed tube, "O"-ring seals, etc. is independent of cell diameter and equal to 100 grams/tube.
9. Weight of base tubes = $16 \text{ g/cm}^2 \times D \times (t_I + 2) \times n_{TOT}$.
10. Tubes are placed in base plate using triangular spacing with a distance center to center of $(D + 0.6)$ cm.
11. An automatic means of bypassing feed flow around broken tubes is provided so that the overall battery efficiency does not drop catastrophically if a tube breaks.
12. The ratio of cell length to cell diameter is limited to $L^{0.6}/D \leq 1$ so that spraying of inside electrode might be accomplished.

5.1.1 Computation of Battery Weight

The total equivalent weight of the electrolysis battery is equal to the sum of the weights of the cells, base tubes, base plate, insulation, outer shell, and accessories plus the weight penalties for power and cooling

$$W_B = W_c + W_{bt} + W_{bp} + W_I + W_S + W_P + W_{HT} \quad (22)$$

where

$$\begin{aligned}
 W_B &= \text{total equivalent battery weight, g} \\
 W_c &= 2.0 \left(\frac{g}{\text{cell}} \right) \times S_{TOT} \\
 W_{bt} &= 16 D (t_I + 2) n_{TOT} \\
 D &= \text{cell diameter, cm} \\
 t_I &= \text{thickness of insulation, cm} \\
 W_{bp} &= .855 (D^2 + 1.2 D + 0.36) \times n_{TOT} \times 13.7 \text{ g/cm}^2 \\
 &= 13.7 A_{bt} \\
 W_I &= 0.1 \text{ g/cc} [2A_{bp} t_I + \pi t_I (D_I + t_I) H] \\
 W_S &= 2.8 \text{ g/cc} \times .0508 \text{ cm} \times \pi [D_I (H-2) + D_T xH] \\
 W_P &= .330 \frac{\text{lb}}{\text{watt}} \times 454 \frac{\text{g}}{\text{lb}} \times P = 150 \frac{\text{g}}{\text{watt}} \times P \\
 &\text{where } P = \text{total power required for the electrolysis} \\
 W_{HT} &= 4.54 \frac{\text{g}}{\text{BTU/hr}} \times Q_L \\
 &\text{where } Q_L = \text{heat loss through the insulation of} \\
 &\quad \text{the battery}
 \end{aligned}$$

The power was computed from the Equation:

$$P = (\bar{E}_t + IR + \bar{V}_p) \frac{4FN_{O_2}}{E} \quad (23)$$

$$\mu = \sum_{j=1}^{n_T} \lambda_j \theta_j = n_T \lambda \theta$$

where

$$\begin{aligned}
 \bar{E}_t &= \text{average thermodynamic driving force/cell, volts} \\
 F &= \text{Faraday number} = 96,500 \text{ amp secs/g-mole} \\
 N_{O_2} &= \text{oxygen flow rate obtained from battery} = .00131 \text{ g moles/sec} \\
 &\quad \text{for 4 men}
 \end{aligned}$$

Cell polarizations, joint resistances, and current efficiencies were based upon the measured values obtained for OBS #8 (see Section 2.4.1); values of $V_p = 0.3$ volts, $(R_j + R_c) = 0.15$ ohms, and $\epsilon = 0.8$ were used.

A constraint on the amount of heat loss permitted was obtained from the first law of thermodynamics:

$$Q_L = P - N_{O_2} \Delta H_R \quad (24)$$

where

$$Q_L = \frac{k}{t_I} A_{HT} (T - T_{surf})$$

$$A_{HT} = \pi D_I^2 / 2 + \pi H \left(\frac{D_T - D_I}{\ln D_T / D_I} \right)$$

T = operating temperature of the battery

T_{surf} = surface temperature of outside shell, found by trial and error to be 60-80°C for all designs used

N_{O_2} = .00131 g moles/second for 4 men

ΔH_R = heat of reaction for: $2 CO_2 \rightarrow 2 CO + O_2$;

A battery reliability exceeding 0.99 for the 100-day mission was required. The reliability of the battery is a function of the average life of each cell, the number of cells per tube, the number of operating tubes required and the number of replacement tubes available:

$$R = e^{-\mu} \sum_{j=0}^n \frac{\mu^j}{j!} \quad (25)$$

where

$$\mu = \sum_{j=1}^{n_T} \lambda_j \theta_j = n_T \lambda \theta$$

if all tubes have similar characteristics

λ = 1/expected tube life, days

θ = mission length, days

Since valid statistics on battery life based on experimental data was not available, it was assumed that a tube failed when the first cell in it failed; that the distribution of cell life was exponential with a mean of 500 days at 900°C; and that the mean cell life is inversely proportional to the vapor pressure of PtO_2 at the operating temperature (see Section 2.2.3.2). Under these assumptions

$$\lambda_{\text{tube}} = \left(\frac{S}{n_T}\right) \lambda_c + \left(\frac{S}{n_T}\right) \left(\frac{1}{500}\right) \exp [\alpha/1173 - \alpha/T]$$

$$\alpha = \frac{\Delta G}{R} (\text{Pt} + \text{O}_2 \rightarrow \text{PtO}_2) = 19,000^\circ\text{K} \quad (26)$$

Computations showed that for large values of n_S and n_T , Equation 25 could be approximated by a slightly more demanding, but mathematically less complicated constraint:

$$n_S + 1 \geq n_T \lambda_{\text{tube}} \theta e \quad (27)$$

where e = base of natural logarithm

The optimization of electrolysis battery design consisted of determining the values of D , L_e , S , S_{TOT} , n_T , n_S , and operating temperature which yielded the minimum total weight penalty, W_B .

5.1.2 Method of Optimization-Geometric Programming

Geometric programming was chosen as the method for determining the optimum battery design. In order to do this, the objective function (Equation 22) and constraints had to be transformed into posynomial (a polynomial with all positive coefficients) form; i.e., the objective function had to be of the form:

$$W = \sum_{j=1}^N C_j \prod_{i=1}^M x_i^{a_{ij}} \quad (28)$$

where C_j = a positive number

N = the number of terms in the objective function

M = the number of variables being optimized

a_{ij} = a number, positive or negative

The constraints had to be of the form:

$$\sum_{j=N+1}^{N_k} C_j \prod_{i=1}^M x_i^{a_{ij}} \leq 1 \quad (29)$$

N_k = total number of terms in objective function plus constraints

With constraints and objective function in this form, a geometric programming solution can be obtained. Of particular advantage in this work is the fact that the effect of changes in various design parameters (C_j) upon the objective function can be readily determined.

$$\frac{W(\vec{C}_\alpha)}{W(\vec{C}_\beta)} = \prod_{j=1}^{N_k} \left(\frac{C_{\alpha j}}{C_{\beta j}} \right)^{\delta_j} \quad (30)$$

where δ_j is the optimal value the dual variable associated with the j th term.

A more detailed discussion and rigorous proofs of the validity of the above equations is given by Duffin, Peterson, and Zener²². The application of geometric programming to the problem of optimal battery design resulted in the following solution and sensitivity analysis.

5.1.3 The Optimal Design

The total equivalent weight of the optimally designed electrolysis battery was found to be essentially independent of the operating temperature chosen over the temperature range 850°C to 1000°C. For a four-man system, the optimal design yields a physical weight of 62 lb; a power requirement of 1140 watts, and a total weight penalty of 455 lb at 850°C. The corresponding values are 57 lb, 1160 watts, and 455 lb at 1000°C. While the total weight does not change, however, the optimal design does, as can be seen in Table XV. The cell dimensions increase, the number of cells per tube increases, the battery height increases, and the total number of cells and tubes in the battery decreases, as the operating temperature decreases. This corresponds to operating at a lower current density at lower temperatures.

TABLE XV

OPTIMAL BATTERY DESIGN AS A FUNCTION OF TEMPERATURE

	Temperature, °C		
	850	900	1000
Cell diameter, cm (D)	1.4	1.35	1.16
Effective cell length, cm (L_e)	1.9	1.73	1.16
No. of operating cells (S)	353	296	254
No. of operating tubes (n_T)	42	40	37
No. of spare tubes (n_S)	70	80	93
Total No. of tubes (n_{TOT})	112	120	130
Height of battery, cm (H)	33.7	30	25.1
Thickness of insulation, cm (t_I)	5.2	5.22	5.34
O.D. of insulated battery, cm (D_T)	32.5	32.8	31.6
Active area/cell, cm ²	8.35	7.35	4.2
Current density, ma/cm ²	220	370	600
Volts per stack	15	10.6	12.5
Power, watts	1140	1158	1160
Power penalty, lb	393	399	398
Physical weight, lb	62	63	57
Total weight penalty, lb	455	462	455

Major uncertainties exist in that the true effect of temperature upon cell life and upon current efficiency is not known. Better statistical data for both must be developed experimentally. Paliguev and Newmin²³ have developed data which shows that the ratio of ionic to electronic conductivity of calcia-stabilized zirconia remains about 98 for temperatures between 600 and 1000°C; however, other sources of current inefficiency such as the amount of leakage through the joint and through shunt paths may vary with temperature.

Sensitivity analysis shows that significant reductions in total battery weight can be expected from increasing current efficiency and cell life.

It was found that the total equivalent weight varied as $(1/\epsilon)$ to the 0.8 power: $W_B \sim (1/\epsilon)^{0.8}$

An increase in current efficiency from 80% to 90% would result in a weight penalty decrease of 9% or 40 lb, due primarily to a reduction in the power which would be required. An increase to 95% would further reduce the total weight to approximately 395 lb. Such an increase is considered achievable by increasing the length of the seal region from 0.5 cm to 1.2 cm and further perfection of the bell-and-spigot joining technique.

The battery weight varies according to:

$$W_B \sim \lambda_t^{0.130}$$

Thus, doubling the average tube life would decrease the total equivalent weight by 9.6%.

The effect of changing the inlet composition of the gas to the electrolysis battery or the degree of conversion of CO_2 to CO will have only a small effect on the total weight. Changing the conversion from 50% to 90% with a pure CO_2 feed will increase \bar{E}_t from 0.88 volts to 0.94 volts at 923°C. The polarization has been found to be essentially independent of CO/ CO_2 ratio until a conversion of 90% is approached. Furthermore, the systems study showed

$$W_B \sim (E_t + V_p)^\alpha$$

where

$$\alpha = .34 \text{ at } 1000^\circ\text{C}, .38 \text{ at } 900^\circ\text{C}, \\ \text{and } .41 \text{ at } 850^\circ\text{C}$$

so that even at 850°C an increase in conversion from 50 to 90% would increase the weight by a factor of only

$$[(.94 + .30)/(.88 + .30)]^{.41} = 1.021$$

or cause an increase of 2.1% in the overall weight penalty. Changing inlet gas composition from 0 to 20% CO has an effect on V_p comparable to that of changing conversion from 50 to 90%.

Reducing the allowable heat loss from the electrolysis battery (for example to compensate for inefficient heat exchangers or poorly insulated transfer lines) will result in an increase in system weight in the form of increased insulation. The sensitivity analysis showed

$$W_B \sim (Q_L)^{-0.084}$$

5.2 The Carbon Deposition Reactor

The carbon deposition reactor (Reactor 2) was assumed to consist of one or more manually scraped tubular chambers similar to the reactor used in the 100-day test and discussed in Section 3. (See Fig. 31.)

5.2.1 Design Equations

Equation 16 (page 91) relates the conversion achieved to the diameter, flow rate, and length of the reactor:

$$\ln \frac{X - X_e}{X_o - X_e} = \frac{-k_m \pi D z}{\bar{F}} \quad (16)$$

The experimentally determined value for the mass transfer coefficient, k_m , was 0.23 cc/cm²-sec or 0.000170 lb-mole CO reacted/in²-hr at 540°C.

The heat loss from the reactor can be equated to the heat generated:

$$Q_{LC} = \frac{2\pi k_I z (T_c - T_o)}{\ln \frac{D + 2t_L + 2t_{Ic}}{D + 2t_L}} \quad (31)$$

= heat generated

where k_I = thermal conductivity of insulation
 T_c = temperature of reactor
 T_o = ambient temperature
 t_{Ic} = thickness of insulation
 t_L = thickness of the catalyst tube
 D = inside diameter of catalyst tube

Defining F_o and F' as the gas flow rates into and out of the reactor, respectively, in lb-mole/day and \bar{F} as the average flow rate, and accounting for the fact that a four-man system will produce 3.0 lb of carbon (0.25 lb-mole) per day by converting 0.5 lb-mole of CO, then the following relations hold:

$$\bar{F} = F' + 1/8 \quad (32)$$

$$\text{Conv} = \frac{1}{2X_o F_o} = \frac{X_o - X}{X_o (1 - \frac{1}{2} X)} \quad (33)$$

where X_o = mole fraction of CO in gas entering Reactor 2

X = mole fraction of CO in gas leaving Reactor 2

Conv = fractional conversion of CO to CO_2 and C in Reactor 2

Appropriate values for X_o and Conv are 0.75 and 0.60, respectively. F_o then becomes 1.11 lb-mole/day and \bar{F} is 0.985 lb-mole/day. The heat generated by the carbon deposition reaction (Equation 3) in producing carbon at a rate of 3.0 lb/day is 770 Btu/hr. The value of k_I in Equation 31 is 0.05 Btu/ft-hr°F, and the temperature of Reactor 2 is 1004°F (540°C).

Two additional equations are required. First, the volume of the reactor must be sufficient to store the carbon buildup by the reaction without causing excessive pressure drop. If one designs so that the reactor is 25% full at the time of carbon removal, the density of the carbon is 30 lb/ft³, and the time between changes is CT hours, then the volume of the reactor is:

$$V = \pi \frac{D^2 z}{4} = \frac{(3.0 \frac{\text{lb}}{\text{day}}) (4 \frac{\text{ft}^3}{\text{ft}^3 \text{C}}) (CT)}{(30 \frac{\text{lb}}{\text{ft}^3 \text{C}}) (24 \frac{\text{hrs}}{\text{day}})} \quad (34)$$

or

$$\pi D^2 z = 0.0667 \text{ CT}$$

Secondly, enough iron catalyst must be provided in the liner so that all of the catalyst is not removed with the carbon. Initial studies showed that the carbon removed contained about 0.05 pound of Fe catalyst per pound of carbon. Thus if a safety factor of two is allowed, the weight and wall thickness of the catalyst liner are:

$$W_L = 2(0.05 \frac{1b}{1b \ C})(300 \ 1b \ C) = 30 \ 1b$$

$$t_L = \frac{30 \ 1b}{p_L \pi D_L} \quad (35)$$

The total weight of the reactor is then

$$W_{CD} = W_L + W_I + W_{SHELL} + W_{ACC} \quad (36)$$

$$W_L = 30 \ lbs$$

$$W_I = \frac{1}{4} \pi [(D + 2t_L + 2t_{IC})^2 - (D + 2t_L)^2] z \times \rho_I \quad (37)$$

$$W_{SHELL} = \pi (D + 2t_L) t_S z \rho_L \quad (38)$$

$$W_{AAC} = (3 \ 1b)(n_{ACC}) + (1.0 \ 1b/ft)(z) \quad (39)$$

= weight of carbon accumulators plus scrapers

n_{ACC} = number of accumulators used

t_S = thickness of shell = .020 in.

The preceding design equations have been used to calculate the weight, size, and carbon change time of a 1.5 in. diameter reactor for the 4-man, 100-day system. It was assumed that the total reactor length, Z, would be divided into three reactors of equal length, L, and that these would be insulated with a common tubular section of insulation with inside diameter equal to $2.15 (D + 2t_L)$ and thickness t_{IC} . Placing the reactor tubes together, rather than end to end, reduces heat loss without affecting conversion.

The results are given in the first column of Table XVI. The reactor is 1.1 ft in diameter and 3.08 ft long and weighs 68.5 lb. The carbon change time is 6.82 hr. The rate of carbon production of each of the three parallel reactor tubes is approximately three times that of the

TABLE XVI

DESCRIPTION OF 4-MAN, 100-DAY CARBON DEPOSITION REACTOR
AND POSTULATED EFFECTS OF VARYING DIAMETER

	1.5 in. Diameter Reactor	Effect of Varying Diameter			
		Constant kmD		Constant km	
		1 in. Diam.	2 in. Diam.	1 in. Diam.	2 in. Diam.
Length of catalyst tube (z), ft	9.27	9.27	9.27	13.9	6.95
Length of reactor (L), ft	3.09	3.09	3.09	4.64	2.32
Thickness of catalyst tube (T_L), in.	.203	.304	.152	.203	.394
Thickness of insulation (T_{IC}), in.	4.55	3.84	5.49	7.30	4.23
Overall diameter (D_{O3}), in.	13.2	11.1	15.9	17.6	14.5
Weight of insulation (W_I), lb	16.4	8.72	24.1	47.5	13.8
Weight of shell (W_{SHELL}), lb	3.78	3.30	4.55	5.03	4.23
Weight of accumulators (W_{ACC}), lb	18.3	18.3	18.3	25.7	16.0
Total weight (W_{CD}), lb	68.5	60.3	76.9	108	64.0
Carbon change time (CT), hr	6.82	3.03	12.1	4.54	9.10

experimental reactor during the final three days of the 100-day life test.

Since the reactor design is based on data obtained at one reactor diameter, it does not represent the optimal design. Optimization would require a more exactly defined reaction model, that is, a model derived from experiments covering a range of reactor diameters and gas flow rates.

Columns 2 through 5 of Table XVI illustrate how the design might be affected by diameter. Two cases are postulated; (1) the product $k_m D$ is a constant and (2) k_m is a constant independent of diameter. The table shows that the reactor weight would decrease with decreasing diameter in one case and would increase in the other. These examples emphasize the need for additional experimental data to better define the rate equation.

The optimal diameter of the reactor cannot be calculated without an accurate model. However, it seems likely that a carbon deposition reactor weight of 60 lbs or less can be used for a 4-man, 100-day mission. Further weight reductions might be achieved by placing the carbon deposition reactor tubes inside of the insulation for the electrolysis battery as is discussed in Section 5.4.

5.3 The Heat Exchangers

Both heat exchangers were designed as concentric-tube, counter-current heat exchangers with the hotter fluid on the inside to reduce heat losses.

The physical weight of a concentric tube heat exchanger is determined from the diameters, wall thicknesses, insulation thickness and length of the exchanger. Referring to Figure 48 and the nomenclature in Appendix E, it is clear that the physical weight of the exchanger is:

$$\text{Physical Weight} = W_1 + W_2 + W_3 \quad (40)$$

Dwg. 856A798

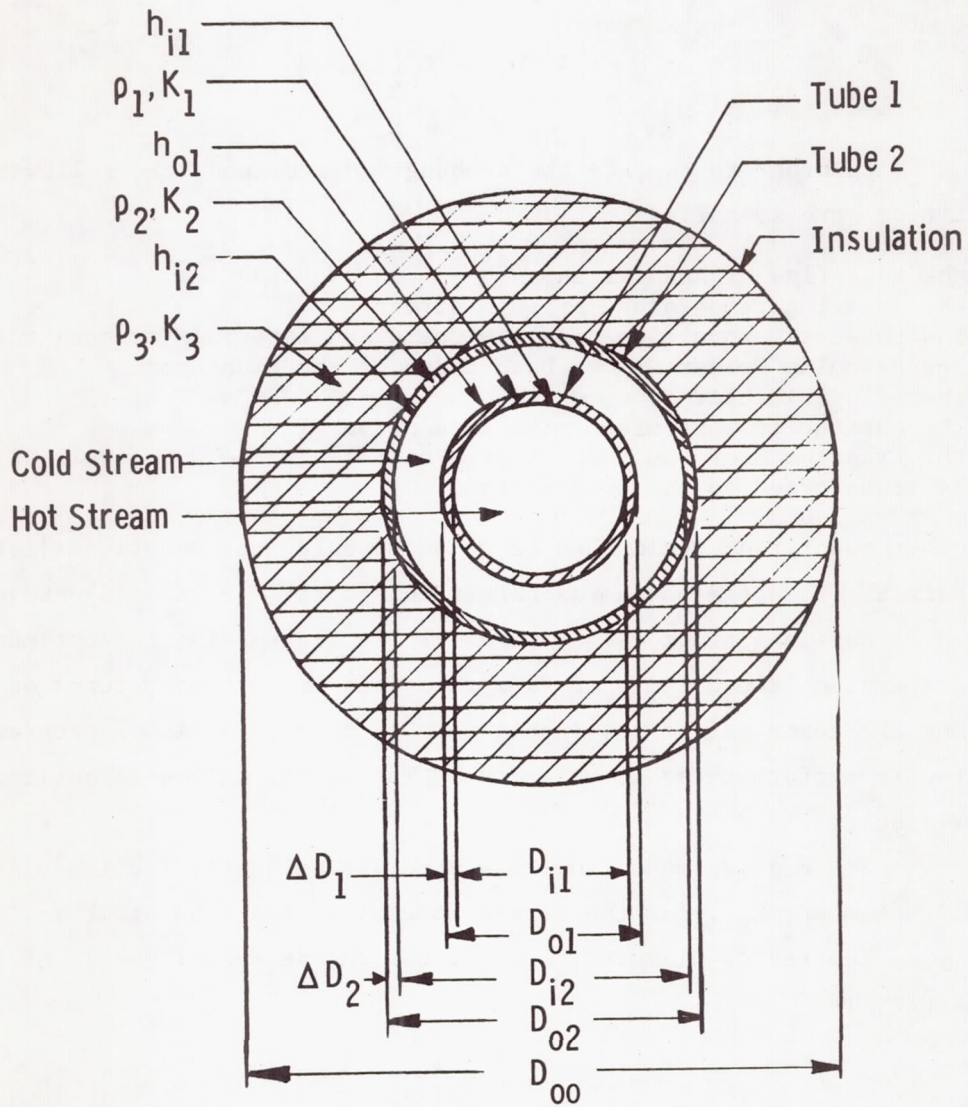


Fig. 48 - Heat exchanger design parameters

where W_1 , W_2 and W_3 are weights of the inside tube, outside tube and insulation, respectively. Referring to Fig. 48, it is seen that:

$$W_1 = \frac{\pi}{4} (D_{o1}^2 - D_{i1}^2) L \rho_1 \quad (41)$$

$$W_2 = \frac{\pi}{4} (D_{o2}^2 - D_{i2}^2) L \rho_2 \quad (42)$$

$$W_3 = \frac{\pi}{4} (D_{oo}^2 - D_{o2}^2) L \rho_3 \quad (43)$$

In order to compute the exchanger dimensions, the following quantities were specified:

1. the mass flow of both streams
2. the entering temperature of each stream
3. the physical properties of all streams and materials of construction
4. the Reynolds Number N_{Re} on both sides of the exchanger
5. the allowable heat loss, Q_L
6. the surface temperature of the insulation, T_o
7. the fraction Z of the total heat available in the hot stream which is transferred to the cold stream.

All other quantities could then be computed using the equations listed in Appendix E. To optimize the exchanger design (1), (2) and (3) above were varied to obtain minimum weight penalty. In determining the optimum overall system, the effects of flow rates and inlet temperatures on the minimum exchanger weight obtainable were required. An ALGOL program was written to perform these computations. The design method is outlined briefly below.

For a given mass flow rate of a stream, specification of the Reynolds Number, N_{Re} , for the stream determines the tube diameter.

The inside diameter, D_{i1} , of the inside tube (tube 1) of the exchanger, is:

$$D_{i1} = \frac{4 F(j)}{\pi \mu N_{Re}} \quad (44)$$

The outside diameter of tube 1 is:

$$D_{01} = D_{i1} + 2\Delta D_1 \quad (45)$$

where ΔD_1 is the wall thickness of tube 1. Similarly, for the annulus (See Appendix E, Equation E-2).

$$D_{i2} + [4 F(j)/\pi \mu N_{Re}] - D_{01} \quad (46)$$

and

$$D_{02} = D_{i2} + 2\Delta D_2 \quad (47)$$

In order to compute the outside diameter of the insulated exchanger, D_{00} , the heat exchanger length is required. If the overall heat transfer coefficient governing the heat exchange between the high temperature stream (in tube 1) and the low temperature stream (in the annulus) is based on the inside area of tube 1, A_{i1} , and if the amount of heat to be exchanged from this gas in tubes 1 to the gas in tube 2 is Q_x , then:

$$Q_x = U_{i1} A_{i1} \Delta T_{Lm} \quad (48)$$

where U_{i1} and ΔT_{Lm} are defined in Equations E-3 through E-7 in Appendix E. From Equation 44, noting that $A_{i1} = \Delta D_{i1} L$,

L = length of tube 1 = length of heat exchanger

$$L = [Q_x / (U_{i1}) (\Delta T_{Lm}) (\pi) (D_{i1})] \quad (49)$$

Note that the heat exchanger length is determined solely by Q_x and the dimensions of the inner tube of the exchanger; it is independent of the heat loss or any other dimensions. Since U_{i1} is itself of a function

length (Equations E-3 through E-7, Appendix E), an iterative procedure was employed to determine L.

For any desired heat loss, Q_L , from the gases in the annular part of the exchanger, the required insulation thickness, and hence the overall diameter of the exchanger, can be determined if the convective heat transfer coefficient between the insulation and cabin atmosphere is known. Since the circulation rates in the space cabin are not specifically known, the outside skin temperature of the insulation is assumed to be some temperature, T_0 , which implicitly assumes that the circulation in the cabin will be sufficient to transfer Q_L away over the temperature gradient present, $(T_0 - T_A)$. (T_0 is one of the variables that must be optimized.)

To transfer Q_L Btu/hr from the annular gas stream to the cabin atmosphere, another overall heat transfer coefficient, U_0 , is defined (Equation E-8 of Appendix E), based on the outside area of the insulation. Therefore:

$$Q_L = U_0 A_0 \Delta T \quad (50)$$

from which

$$D_{00} = \exp \left\{ K_3 \left[\frac{\pi L \left(\frac{t_L + t_L'}{2} - T_0 \right)}{Q_L} \right] - \frac{1}{D_{i2} h_{i2}} - \frac{\ln \left(\frac{D_{02}}{D_{i2}} \right)}{k_2} + \ln D_{02} \right\} \quad (51)$$

Note that D_{00} , and hence W_3 (Equation 43 is a strong exponential function of T_0 , Q_L and L.

Thus all the quantities needed to calculate the physical weight (Equation 40) of the heat exchanger are available. All that remains to be calculated are the weight penalties for heating, cooling and pumping requirements of the exchanger.

The specific weight penalties for heating (pH), cooling (PC), and pumping (PP) are defined to be fixed values with units of lb/BTU heat/hr, lb/BTU cool/hr and lb/watt; respectively. Referring to Fig. 49, the weight penalties for heating and cooling (WPEN) and for pumping (WAP) are:

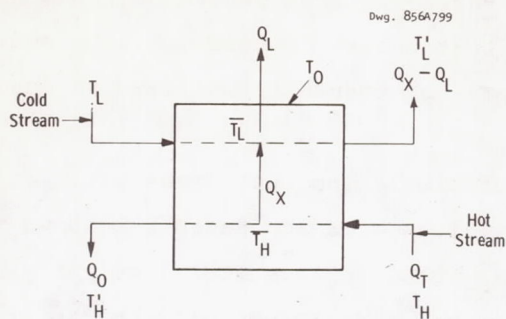


Fig. 49 - Heat flow for a generalized countercurrent heat exchanger

$$WPEN = (Q_L + Q_O) \times PC + (Q_A) \times PH \quad (52)$$

$$WAP = [(v_1 \Delta P_1 A_1 + v_2 \Delta P_2 A_2)] \times PP \quad (53)$$

where: Q_A = external heat input necessary to heat a stream if sufficient heat is not available to accomplish the heating in a heat exchanger, (may be zero).

Q_O = heat content of high temperature stream leaving an exchanger.

Q_L = heat loss through insulation of exchanger

$\Delta P_1, \Delta P_2$ = pressure losses due to flow in tube 1 and tube 2, respectively.

ΔP_1 and ΔP_2 are defined in Appendix E in equations E-9 and E-10. v_1 and v_2 are defined in equation E-11 and E-12. The general heat balances, based on Fig. 49, are found in Appendix E. These heat balances are general, but can be readily applied to both exchangers with few modifications.

The total equivalent weight of a heat exchanger is:

$$WT = W_1 + W_2 + W_3 + WPEN + WAP \quad (54)$$

It is evident that the variables that determine the magnitude of WT are N_{Re} for both the inner tube and the annulus, T_O , Q_L and Q_X .

The same general procedure is utilized to design both heat exchangers 1 and 2.

The results of simulation Heat Exchanger 1 at several Reynolds Numbers with different values of Z and Ratio are shown in Table XVII. It is clear that high N_{Re} lead to lower total weight penalties. However, Reynolds numbers much higher than 10,000 will not be practical since sonic flow is approached. Note that to achieve such N_{Re} , an annulus with outside diameter less than 0.15 inch is required.

Similar results were obtained for Heat Exchanger 2.

The principal weight penalty in the total weight is that for the heat required to raise the temperature of the CO_2-H_2O stream leaving the exchanger to that of Reactor 1. Most of this weight penalty can be eliminated by adding a few pounds of insulation to Reactor 1 rather than by using electrical heating as was assumed in the foregoing computation. More will be said about this in the section which follows.

TABLE XVII

PREDICTED DESCRIPTION OF HEAT EXCHANGER 1 AS A FUNCTION OF SYSTEM PARAMETERS

System Parameters				QX	L	DOO	WIN	WTUBE	WH	WC	WPUMP	WTOT
R_{ec}	R_{ea}	Z	Ratio									
4,000	1,000	.50	.43	75.9	4.9	.216	1.92	1.85	74.21	1.09	.61	79-66
4,000	1,000	.85	.43	124.9	14.5	133.8	2.4×10^6	4.8	63.05	.76	4	2.4×10^6
4,000	1,000	.94	.43	136.7	24.2	8.3×10^4	$>10^{20}$	7.88	60.4	.67	.73	$>10^{20}$
10,000	4,000	.935	.43	136.0	.69	.024	.002	.058	60.5	.68	1.66	62.9
10,000	4,000	.935	.55	136.0	.72	.021	.0008	.071	67.0	.84	1.66	69.8
10,000	4,000	.935	.65	136.0	.92	.0197	.0008	.086	72.5	.98	1.66	75.7
10,000	4,000	.935	.70	136.0	1.00	.0191	--	.097	75.2	1.05	1.66	78.7
1,000	250	.85	.43	124.9	25.2	3.7×10^5	$>10^{20}$	33.0	63.05	.76	.002	$>10^{20}$
1,000	250	.935	.43	136.0	40.9	1.4×10^4	$>10^{20}$	52.3	60.5	.68	.001	$>10^{20}$

 R_{ec} = Reynolds number in inner (circular) tube of heat exchanger R_{ea} = Reynolds number in outside (annular) tube of heat exchanger

Z = [QX/QT] a ratio of amount of heat exchanged compared to amount of heat available for exchanger efficiency

Ratio = [QL/QX] a measure of the amount of heat lost by the annular stream based on what is exchanged to it

QX = amount of heat exchanged between streams in heat exchanger, Btu/hr

L = length of the heat exchanger, ft

DOO = outside skin diameter of heat exchanger (overall diameter), ft

WIN = weight of insulation, lb

WTUBE = weight of tubes, lb

WH = heating penalty weight, lb

WC = cooling penalty weight, lb

WPUMP = pumping penalty weight, lb

WTOT = total system weight of heat exchanger, lb

5.4 Overall System Optimization

The computations described in Sections 5.1 through 5.3 indicate that the following total weight penalties would be obtained if each subsystem were optimized, considering the interaction between subsystems only insofar as low conversions were avoided:

	<u>Physical Wt.</u>	<u>Heat Loss and Power Penalty</u>
Heat Exchanger 1	0.1	~ 50 lb
Reactor 1	~60.0 lb	~395 lb
Heat Exchanger 2	0.1	~ 50 lb
Reactor 2	~60.0 lb	8 lb
Hydrogen Diffusion*	<u>0.5 lb</u>	<u> </u>
	121.0 lb	503 lb

These computations assume that each subsystem must be separately insulated. Considerable reduction in both heat losses and insulation weight can be achieved by burying the heat exchangers and hydrogen diffusion apparatus in the insulation surrounding the electrolysis reactor. This is certainly feasible in view of the fact that the heat exchanger diameters are less than 1/8 in. and the palladium diffusion tubes are manufactured commercially in 1/8 in. diameter. By appropriate location of the exchangers in the insulation, the average temperature of the annular section of the exchangers and that of the insulation can be matched. In this way, heat losses from the exchangers can be essentially cut to zero and the equation

$$Q_L = P - N_{O_2} (\Delta H_R) \quad (24)$$

can be applied to the Reactor 1 as was done in Section 5.1.

* Based upon an area requirement of 30 in², an area per unit length of 4.8 in²/ft, and a weight of .08 lbs/ft for the palladium tubing and vacuum jacket.

It would also be desirable to place the carbon deposition reactor inside of the insulation for Reactor 1 if the length of the two reactors could be made compatible.

If the heat exchangers and H₂ diffusion annuli are placed in the insulation and Reactor 2 is maintained separately, then the weight of the optimal system is as indicated in Table XVIII.

A clear definition of the optimum recycle ratio and the operating temperatures for Reactor 1 and Reactor 2 requires a more accurate model to describe the conversion in Reactor 2 and additional experimentation to determine the effect of temperature on conversion of CO₂ to CO, and of current density on cell life.

Major reductions in total system weight can be achieved primarily by increasing the current efficiency and life of the electrolysis batteries, and by finding insulation materials with lower ρ_I and k_I .

TABLE XVIII

WEIGHT OF THE OPTIMUM OVERALL SYSTEM

	Physical Wt, lb	Penalties, lb	Total, lb
Heat Exchanger 1	0.1	0	0.1
Reactor 1	60.	395	455.
Heat Exchanger 2	0.1	0	0.1
Reactor 2	60.	8	68.
Hydrogen Diffusion	0.5		0.5
System	121.	403	524.
Pounds/man	30	101	131

6. CONCLUSIONS AND RECOMMENDATIONS

6.1 Conclusions Concerning Overall System Operability

No major obstacles are foreseen in the construction of an efficient, long life solid electrolyte oxygen regeneration system as a result of the following conclusions based on the experimental work carried out under this contract:

1. Efficient regeneration of oxygen from $\text{CO}_2\text{-H}_2\text{O}$ mixtures can be carried out in multi-cell batteries employing $(\text{ZrO}_2)_{0.9}(\text{Y}_2\text{O}_3)_{0.1}$ as the electrolyte, platinum cathodes, sputtered Pt- ZrO_2 anodes, and bell-and-spigot joints. An overall power requirement of 0.34 watts/cc/minute or less can be anticipated when such batteries are constructed with sufficient control over existing fabrication techniques.
2. An operating life exceeding 100 days can be obtained from five-cell batteries of the above construction operating at 920°C and a current density of 200 ma/cm^2 .
3. If a feed stream including 3-8% H_2 is employed, a continuous carbon deposition reactor utilizing the reactor wall itself as a catalyst can be operated for periods exceeding 100 days.
4. Carbon can be removed from the reactor by a manually operated scraper. Less than 5 minutes/day of crew time would be required for the carbon removal and storage process.
5. The carbon produced by the above reactor is dry and free flowing. Carbon migration to other parts of the system can be eliminated by the use of high temperature filters. Because of the carbon's low moisture content and large particle size no filter clogging should occur.

6. At temperatures of 800°C and higher palladium foils can be used to effectively remove H_2 from a CO , CO_2 , H_2 , H_2O mixture with no carbon deposition occurring on the palladium surface.
7. Based on the current performance of the above major system components, a solid electrolyte system to supply pure oxygen to a 4-man, 100-day mission can be built which will weigh about 121 pounds and require approximately 1160 watts of power. The total weight penalty, including sufficient cell redundancy in the electrolysis battery to obtain a reliability of 0.99 for the 100 days, would be approximately 524 pounds.

6.2 Conclusions Concerning Design, Construction, and Operation of Major System Components

6.2.1 The Electrolysis Battery

1. Highest anode performance appears to be obtained from a composite structure consisting of a thin sputtered Pt- ZrO_2 coating topped by a heavier coating of sintered platinum to obtain a suitably low electrode resistance.
2. Battery polarizations were significantly less than predicted on the basis of the testing of single cell devices -- less than 0.3 volts per cell at both 920°C and 1000°C. This improvement appears to have been a result primarily of the development of the composite anode and the more uniform application of the platinum cathode obtained by spraying rather than brushing the Pt in the fabrication process.
3. Total electronic resistance -- including joints, electrodes, and electrode-electrolyte contact -- of less than 0.16 ohms/cell can be obtained. This is demonstrated by the performance of OBS # 8 when the total ohmic resistance at 920°C was 0.52 ohms of which 0.36 ohms was the computed electrolyte resistance.

4. Deterioration of performance, other than that caused by electrolyte cracking, appears to be caused by an increase in cell resistance due to peeling and evaporation of the anode (oxygen electrode). This appears to explain the decline in both current efficiency and power efficiency with time.
5. All changes in current efficiency with time are explainable in terms of increased shunt currents caused by the increase in anode resistance. No change in ionic/electronic conductivity ratio is evident.
6. Electrolyte pitting and cracking does not appear to be a result of an electrode-electrolyte interaction. Considerable understanding of the causes of electrolyte cracking was gained in this research, and its incidence reduced by control over fabrication and operating techniques. However, it still remains as a problem which has not been completely solved.
7. While it does lead to a loss of efficiency, deterioration of the anode does not cause catastrophic failure.
8. Reductions in electrolysis battery weight and power exceeding 10% can be achieved by redesign of the joint to increase current efficiency from 0.80 to 0.95. A further 5% reduction in weight could be achieved by a 40% increase in average cell life.

6.2.2 Carbon Deposition

1. In the presence of 3 to 8 percent H_2 in the $CO-CO_2$ mixture, the steel shell of the reactor is an effective catalyst for the carbon precipitation reaction and the activity of the catalyst does not decline with time.
2. Catalyst consumption with a steel reactor is of the order of 0.037 g per g of carbon produced.

3. With a reactor 1.5 in. I.D. by 12 in. long, carbon deposition rates of 6 g/hr with a CO conversion of approximately 60 percent can be realized from a gas mixture containing 75 percent CO, 21 percent CO₂, and 4 percent H₂.
4. The maximum conversion of CO to CO₂ and carbon occurs at 540°C or below for flow rates equal to the average of the 100-day test.
5. Methane formation in the reactor is low, the concentration in the product gas being of the order of 0.1 percent.
6. The rate of carbon deposition appears to be mass transfer controlled. Initially it appears that the main resistance to mass transfer is diffusion in the gas phase. However, as the carbon layer on the reactor wall begins to build up, the resistance to diffusion through it also becomes important.

6.2.3 H₂ Removal

1. A palladium diffusion membrane in the form of a tube (0.125 in. O.D., 9 in. long, and .005 in. wall) seems completely stable in CO-CO₂-H₂ mixtures at temperatures ranging from 700°C to 950°C.
2. Carbon precipitation on palladium does not occur at temperatures above 800°C.
3. The permeability of palladium to H₂ at 800°C is

$$1.46 \frac{\text{cm}^3}{\text{cm}^2} \frac{\text{mm}}{\sqrt{\text{atm}}} .$$
4. A palladium tube of the dimensions used has sufficient capacity for H₂ separation to meet a 0.5-man requirement.

6.3 Recommendations

It is recommended that the development of a solid electrolyte oxygen regeneration system be continued. It seems logical that

major efforts should be made to:

1. Improve the life and performance of solid electrolyte electrolysis batteries.
2. Assemble the electrolysis battery, carbon deposition reactor, hydrogen diffusion apparatus, heat exchangers, and recycle blower into an integrated bench-scale system to determine the problems of control and general operating difficulties which arise from component interaction.
3. Investigate methods of CO_2 and water concentration which can be used most advantageously with a solid electrolyte system, taking advantage of the available heat and the ability to handle CO_2 and water simultaneously.

The objective of obtaining high performance batteries with long life appears to be of prime importance, and the future research should investigate the techniques for improving the fabrication of joints and anodes outlined in Section 2.4.3.

APPENDIX A
Determination of Open-Circuit Voltage
for C-H-O System

The open circuit voltage of the fuel cell, E_t , can be expressed in terms of the well-known Nernst equation.

$$E_t = \frac{RT}{Fn} \ln \frac{P_{O_2, H}}{P_{O_2, L}} \quad (A-1)$$

where

R = the universal gas constant, 8.134 watt-sec/°K mole

T = the absolute temperature of the cell, °K

n = the total number of electrons participating in the over-all reaction.

F = the number of coulombs per equivalent

= 96,500

$P_{O_2, H}$; $P_{O_2, L}$ = the O_2 partial pressure in the oxygen and feed chambers, respectively, atm.

the oxygen partial pressure in the oxygen chamber is 1.0. The equilibrium reactions in the feed chamber are



Since Equation A-4 can be obtained by subtracting Equation A-2 from A-3 only two of the equations are independent, and the partial pressure

of oxygen in the feed chamber, $P_{O_2,L}$ can be determined from the following equilibria.

$$K_1 = \frac{1}{K'_1} = \exp [+(\Delta F_1)/RT] = \frac{P_{CO_2}}{P_{CO} P_{O_2,L}^{1/2}} \quad (A-5)$$

$$K_3 = \exp [-(\Delta F_3)/RT] = \frac{P_{CO_2} P_{H_2}}{P_{CO} P_{H_2O}} \quad (A-6)$$

where

K_1, K_3 = equilibrium constants for reactions A-2 and A-4

P_i = partial pressure of component i in the fuel chamber

$\Delta F_1, \Delta F_2$ = standard free energy change of reactions A-2 and A-4
cal/mole

The partial pressures in the feed chamber are also related to the total pressure, π , by Dalton's Law

$$\pi = P_{CO} + P_{CO_2} + P_{H_2} + P_{H_2O} + P_{O_2,L} \quad (A-7)$$

The equilibrium partial pressures in the feed chamber can be calculated from Equations A-5, A-6, and A-7 and the oxygen, hydrogen, and carbon content of the gas which is conveniently represented by two ratios: moles O per mole C, O/C; and moles H per mole C, H/C. The equilibrium partial pressures are presented in terms of O/C, H/C, and the equilibrium constants in Table A1. The open circuit voltage is obtained by substituting the expression for $P_{O_2,L}$ into Equation A-1

$$P_{O_2,H} = 1:$$

$$E_t = \frac{RT}{4F} \ln \frac{K_1^2}{\phi} \quad (A-8)$$

where ϕ is defined in Table A1.

TABLE A1

Equilibrium Partial Pressures for Ternary O-H-C System

$$P_{O_2-L} = \frac{\phi^2}{K_1^2}$$

$$P_{CO} = \frac{(1 - \phi^2/K_1^2)}{(1 + \phi)(1 + \frac{1}{2} \frac{H}{C})}$$

$$P_{H_2} = \frac{\frac{1}{2} \frac{H}{C} K_3 (1 - \phi^2/K_1^2)}{(\phi + K_3)(1 + \frac{1}{2} \frac{H}{C})}$$

$$P_{H_2O} = \frac{\frac{1}{2} \frac{H}{C} (1 - \phi^2/K_1^2) \phi}{(\phi + K_3)(1 + \frac{1}{2} \frac{H}{C})}$$

$$P_{CO_2} = \frac{\phi (1 - \phi^2/K_1^2)}{(1 + \phi)(1 + \frac{1}{2} \frac{H}{C})}$$

Where ϕ is given by

$$\phi \left(\frac{O}{C} - 2 \right) + \left(\frac{O}{C} - 1 \right) = \frac{\frac{1}{2} \frac{H}{C} \phi (1 + \phi)}{\phi + K_2} + \frac{2\phi^2}{K_1^2 - \phi^2} \left[(1 + \phi) \left(1 + \frac{1}{2} \frac{H}{C} \right) \right]$$

The percent of the available oxygen removed from the feed chamber can be represented as

$$\% \text{ oxygen removed} = \frac{2 + \frac{1}{2} \frac{H}{C} - \frac{O}{C}}{1 + \frac{1}{2} \frac{H}{C}} \quad (A-9)$$

This expression is obtained by comparing the oxygen present per mole of carbon, $O/C-1$, with the oxygen present per mole of carbon for pure carbon dioxide and water, $2 + 1/2 H/C$.

Figures A1, A2, and A3 present theoretical curves for open circuit voltage vs the percent of oxygen removed for constant H/C parameters at $1200^{\circ}K$ and $1300^{\circ}K$. Hydrogen to carbon ratios are presented corresponding to initial water contents of 0% water, $H/C = 0$; 20% water, $H/C = 0.5$; and 50% water, $H/C = 2.0$.

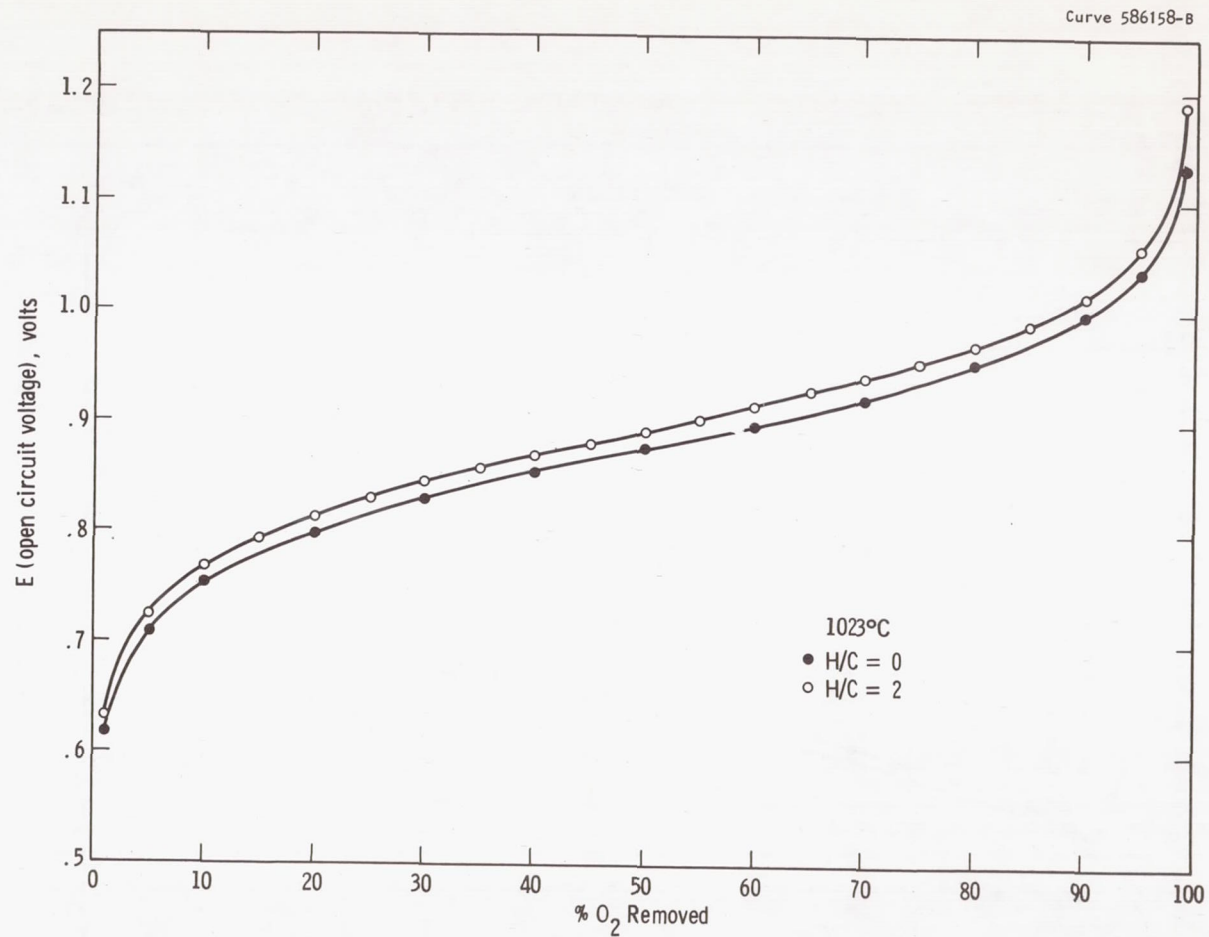


Fig A1 - Thermodynamic voltage, E_t , as a function of the percent of available oxygen removed and as a function of H/C at $1023^\circ C$

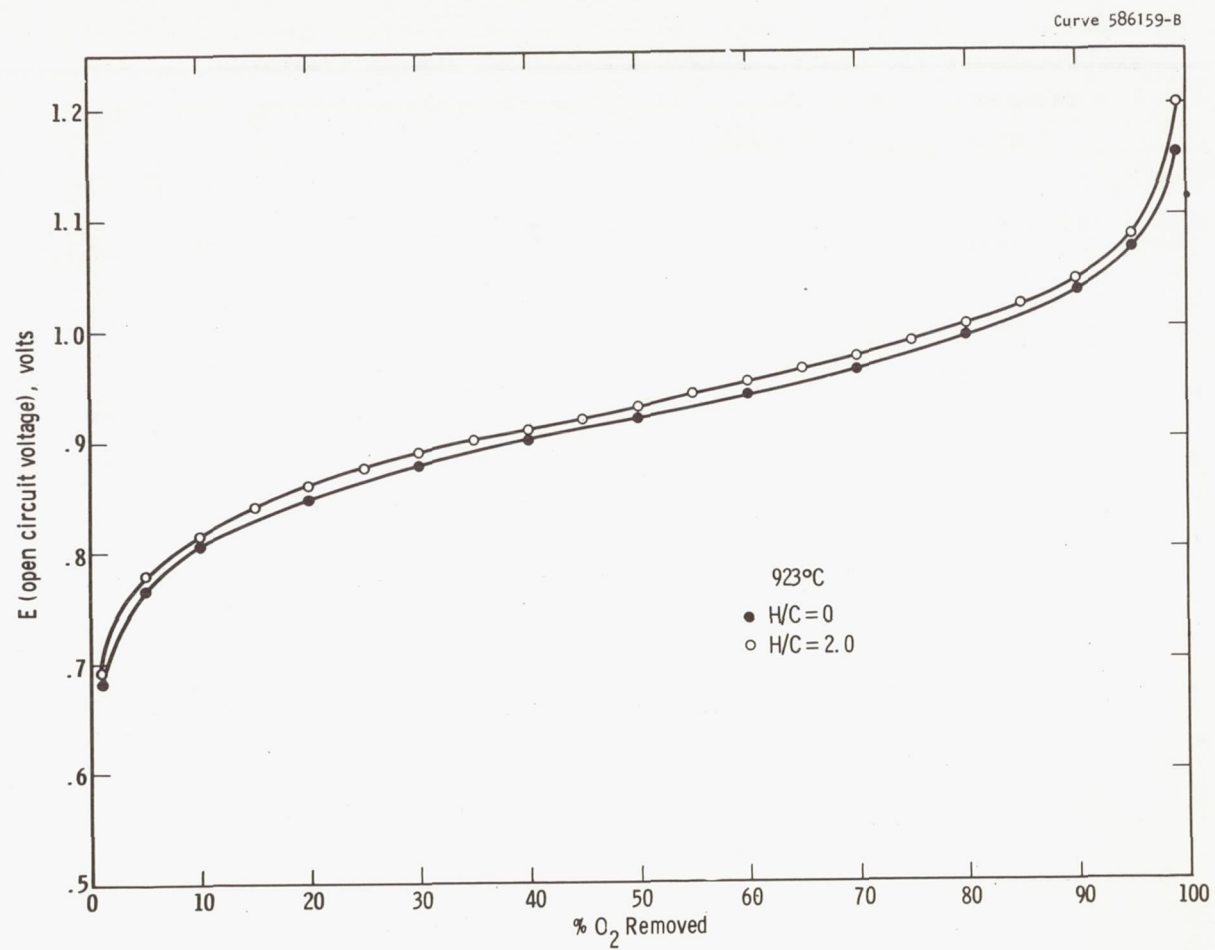


Fig. A2 - Thermodynamic voltage, E_t ,
at 923°C

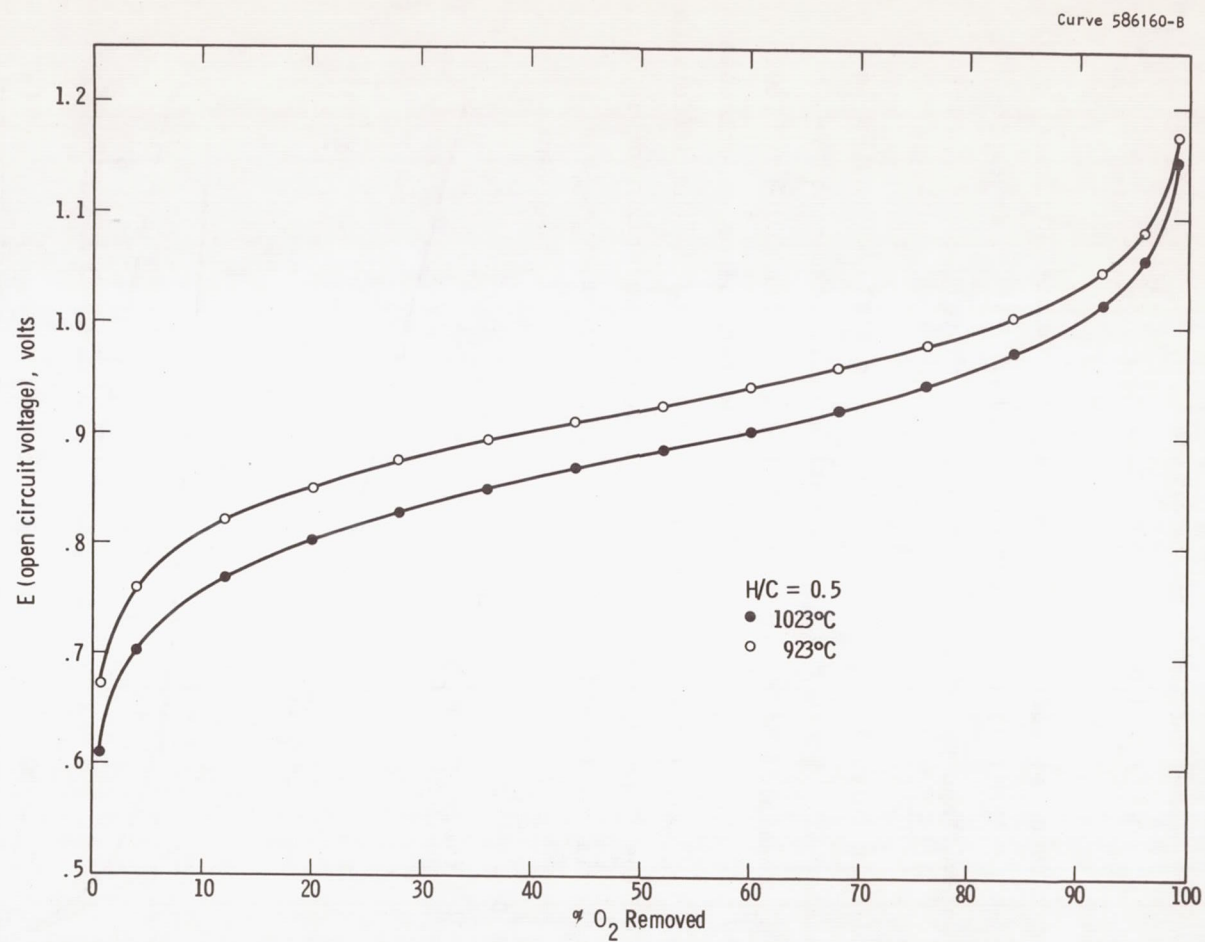


Fig. A3 - Effect of temperature on E_t at fixed H/C ratio

APPENDIX B
Methods Used to Determine
Ohmic and Polarization Losses

Two different methods for determining the ohmic (IR) losses and polarizations of the individual cells were used: direct interpretation of current-voltage plots and interpretation of voltage-time plots obtained by current-interrupt techniques.

The direct interpretation of V-I curves to yield IR and V_p is illustrated in Fig. B1. Curve V is the experimentally determined V-I curve. Curve E_t is a plot of E_t vs current density at the $\text{CO}_2\text{-H}_2\text{O}$ flow rate at which V was obtained; it may be either theoretical or experimental (see Fig. B2). The cell resistance, R, can be determined as the difference in the slopes of the V and E_t curves; the maximum cell polarization is computed to be equal to the difference in the intercepts: $V_0 - e_0$.

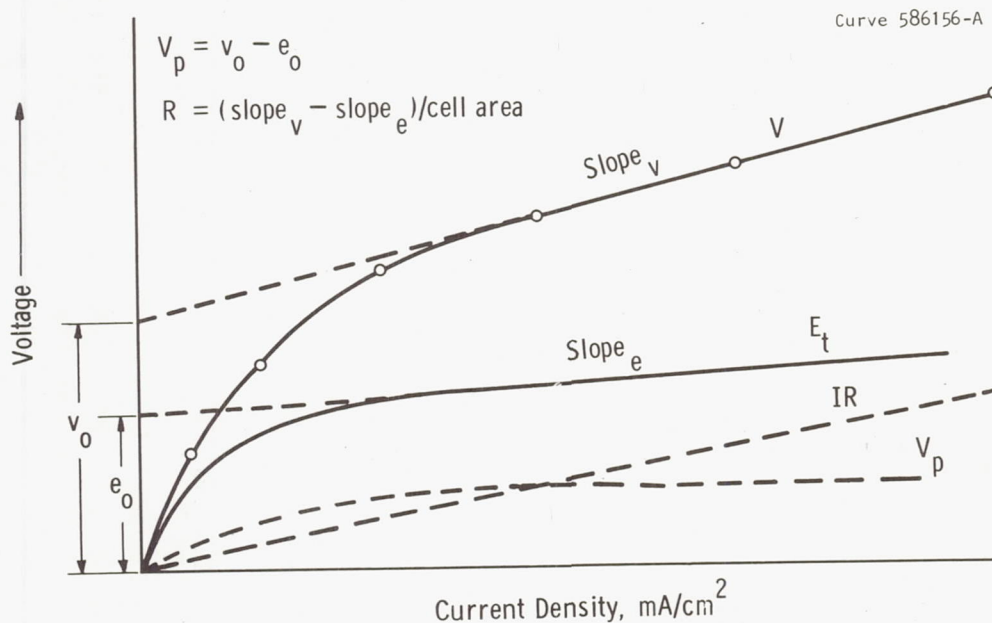


Fig. B1 - Illustration of method used to obtain IR and V_p from V-I curves

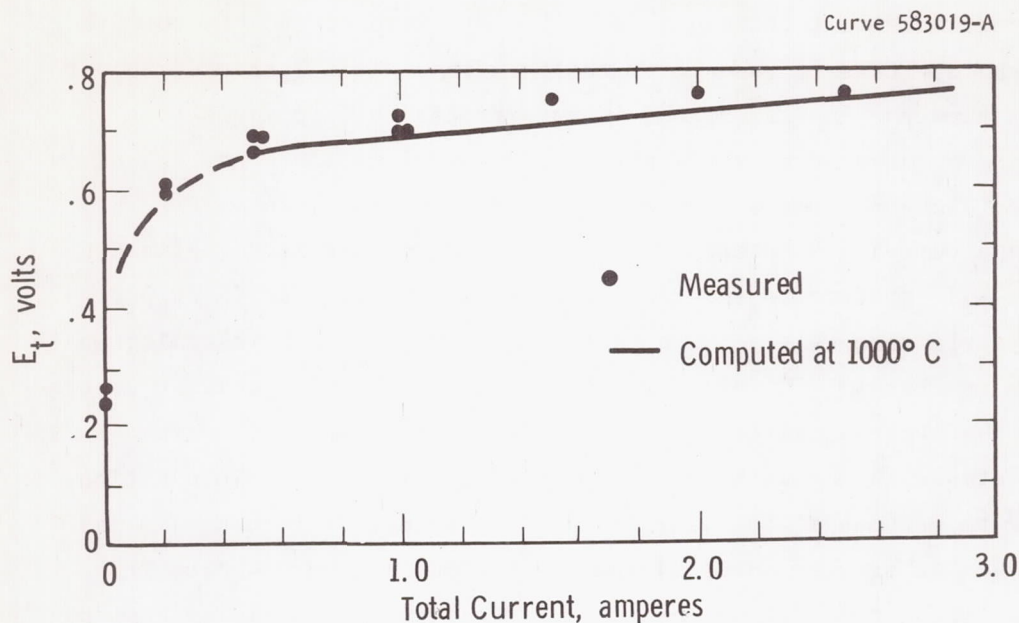


Fig. B2 - Minimum decomposition voltage as a function of total current drawn when the inlet gas flow equals 280 cc/min

Determination of R and V_p in this manner is based upon the fact that polarization tends to vary as $\ln I$:

$$V_p = K \ln I$$

$$\frac{dV_p}{dI} = \frac{K}{I}$$

Thus, as I becomes large, the slope of V_p vs I tends toward zero. Thus, its contribution becomes small compared to the slope of IR vs I and E_t vs I and, in many cases, small compared to the uncertainty in the slope caused by measurement errors. When K is large (i.e., with high polarization electrodes), however, there is a tendency to overestimate R and underestimate V_p when this technique is used.

The cell IR loss and polarization can be separated by using the current interrupt technique described by Sverdrup and his co-workers.²⁴ This technique takes advantage of the fact that ohmic losses disappear instantaneously when the current is interrupted while polarization losses and E_t disappear over a period of several milliseconds. A schematic of an oscillograph from a current interrupt test is shown in Fig. B3. Before the current is interrupted the driving voltage is V (defined by Equation 4). At time t_0 the current is interrupted. The IR drop disappears instantaneously and can be read directly from the oscillograph as shown in Fig. B3. However, reduction in polarization voltage occurs only as the gas composition at the electrode-electrolyte interface equilibrates with the bulk gas composition by diffusion. In addition, the bulk phase composition will change if a significant change in gas composition is brought about by the electrolysis; E_t drops from its operating value to E_{t0} , the open circuit voltage for the inlet gas composition (see Appendix A for discussion of the effect of gas composition on E_t). The total elapsed time from t_0 until the asymptote is "reached" runs from 30 to 200 milliseconds for a good electrode.

Once IR has been determined from the oscillograph and E_t by computations or actual measurement with an open circuited cell in the

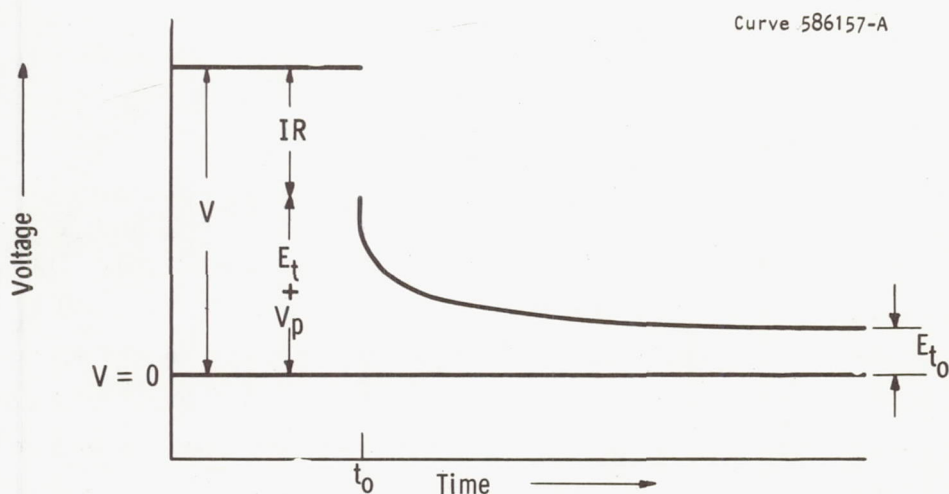


Fig. B3 - Use of current interrupt photo to determine IR, E_t and V_p

gas stream leaving the working cell, (See Fig. B3) V_p can be computed by rearranging Equation 4:

$$V_p = V - E_t - IR$$

The electrolyte prove divides each cell into two half cells so that

$$V = V_c + V_a$$

V_c = Driving voltage for cathode half cell

V_a = Driving voltage for anodic half cell

A separate oscillograph can be taken for each half cell voltage and from them, values of IR_a , IR_c , E_{ta} , E_{tc} , V_{pa} , and V_{pc} can be obtained.

Theoretically, if the electrolyte prove is more than five times the electrolyte thickness away from the electrode edge²⁴, the voltage read is equivalent to the voltage at a plane midway between the two electrodes so that the electrolyte resistance is equally divided between the two half cells.

In actual practice, however, obtaining reliable information from the electrolyte prove proved difficult. Rather than obtaining a 50-50 split of electrolyte resistance between half-cells, splits from 90% anodic - 10% cathodic to 40% anodic - 60% cathodic were measured. In most cases, this uneven split was due to improper register of the electrodes, i.e., the cathode electrode did not lie directly below the anode because of the difficulty in locating the inside electrode precisely.

APPENDIX C
Electrode Application Techniques

C.1 Sputtered Platinum Zirconia Anodes

Reactive sputtering was chosen as the method of applying the platinum zirconia electrodes because of the ease with which films can be applied to cylindrical geometries and the tight bonding between electrolyte and electrode which can be obtained.

A Westinghouse Model 124 manual high-vacuum system was employed for the sputtering process. An MRC dc high voltage supply (0-5 kv; 0-200 ma) was used to sustain the high voltage glow discharge. The cathode placed in the glow discharge to be bombarded by positive ions was pure Zr metal sheet with pure Pt attached in strips. In the glow discharge, such a cathode emits Zr and Pt vapor. During sputtering, the atmosphere was kept sufficiently oxidizing by the presence of H_2O vapor in the argon needed to perform the actual sputtering process so that the Zr reacted to form ZrO_2 as it was deposited on the substrate with the Pt. The deposition parameters were as follows:

Total Pressure	-- 10-20 μ
Leaked-In Sputtering Atmosphere	-- Argon, 50% H_2O
Applied Voltage	-- 6 kv
Plasma Current	-- 200-250 ma
Substrate Temperature	-- 450°C
Total Deposition Time	-- 17-43 Hours
Cathode Area	-- 300 cm ²
Cathode Composition	-- 75% Pt, 25% Zr, by area to 25% Pt, 75% Zr, by area.

Film deposited under these conditions with the tubular substrates oriented along the axis within the cylindrical cathode, averaged 5-10 μ in thickness.

Six single cell devices (SCD's) containing a total of 18 cells were constructed with outside electrodes of sputtered Pt-ZrO₂. The average electrode weights and compositions of each of the SCD's as well as the "sputtering" cathode composition and run time are summarized in Table C-I. The compositions were estimated by removing the tantalum

TABLE C-I

SUMMARY OF WEIGHTS, COMPOSITIONS, AND SPUTTERING CATHODE FOR THE Pt-ZrO₂ ELECTRODES OF SCD's NUMBER 3 THROUGH 8

SCD No	Sputtering Cathode				Run Time, hrs	Electrode Wt, mg/cm ²	Electrode Composition
	Length	Diameter	% Pt	% Zr			
3	5"	6"	60	40	21.2	12.3	94% Pt
4	5"	6"	75	25	24.3	23.3	89% Pt
5	5"	6"	25	75	17.1	16.6	84% Pt
6	5"	6"	25	75	25.9	4.4	-----
7	5"	6"	25	75	25.9	2.56	-----
8	5"	6"	25	75	43.0	1.52	84% Pt

masks used to define the outside electrodes, dissolving the Pt and ZrO₂ deposited thereon and analyzing by wet chemical techniques. A quick glance at Table C-I reveals that little or no control over electrode composition or weight was obtained. The composition does not appear related to the cathode composition; and the weight is not correlated with the run time. Another problem which is not apparent from the table was the wide variation in coating weight with vertical position when the 6" diameter cathode was used. Separate runs made after the construction

of SCD's 3 through 8 were completed showed the coating densities to be more than twice as heavy at the center than at the top or bottom. Evidence that the % ZrO_2 varies from top to bottom also was obtained. All of the above indicates that further experimental work is needed to perfect a sputtering process which will produce coatings of controlled composition and weight which are uniform over the entire substrate region.

Of the six SCD's with sputtered Pt-ZrO_2 constructed, three were tested. Two of the remaining ones were broken prior to testing, and the third was not tested due to a lack of time. Those tested were SCD 3, 4, and 8.

C.2 Sintered Platinum Electrodes (anodes and cathodes)

Before applying the electrodes, the electrolyte surface was cleaned by boiling in aqua regia for 30 minutes, followed by boiling in water to remove the aqua regia, and an air firing to 1000°C to remove the water and any traces of organic material. The following steps were then carried out to apply an electrode to the outside of an electrolyte tube:

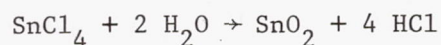
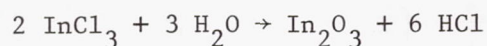
1. Platinum was suspended in turpentine to make a suitable spraying mixture.
2. The electrolyte was masked.
3. A thin layer ($2\text{--}5 \text{ mg/cm}^2$) was sprayed onto the surface using argon as the carrier gas.
4. The sprayed surfaces were dried at $50\text{--}100^\circ\text{C}$ to remove most of the organic solvent and thus prevent blistering during sintering.
5. The coating was sintered in an air atmosphere at 1250°C for one hour.
6. Steps 1-5 were repeated until the final coating weight was reached except that subsequent sinterings are carried out at 1100°C .

Electrodes were applied to the inside of the SCD's by brushing rather than spraying. This was necessitated by the long tube length. A slightly thicker platinum-turpentine suspension was applied to a felt pad which could be located precisely inside of the electrolyte tube and then expanded against and rotated around the tube wall to coat the wall with platinum. The coating weights obtained were generally $1\text{--}3 \text{ mg/cm}^2$

per application. Drying and firing were carried out as described in steps 4, 5, and 6 above.

C.3 Indium Oxide Electrodes

Chemical vapor deposition was used to apply tin-doped In_2O_3 electrodes to the outside of SCD 1 and SCD 2. An aqueous solution of indium and tin chlorides was sprayed into a two zone furnace through a Spraying Systems No. 9564-1/4V nozzle using argon as the carrier gas. In the first zone of the furnace, the solution was evaporated and heated to a temperature of approximately 900°C . The second zone contained the electrolyte substrate to be coated and was maintained at 1000°C - 1050°C . In this temperature range the reactions:



proceed rapidly at the surface, but their rates are negligible in the gas phase. The apparatus used is shown schematically in Fig. C 1.

The coating thickness was controlled primarily by controlling the total amount of solution which was sprayed. Electrode weights from 6.7 to 10 mg/cm^2 were tested.

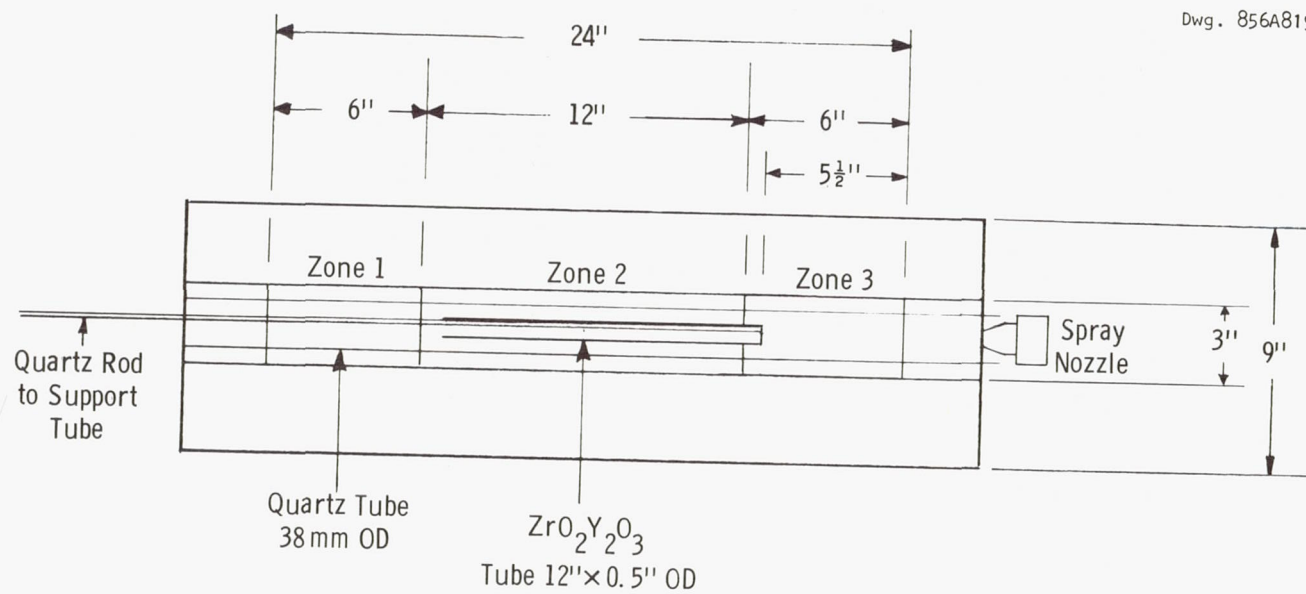


Fig. C 1 - Apparatus used for spraying $\text{ZrO}_2\text{Y}_2\text{O}_3$ tube with Sn doped In_2O_3

APPENDIX D

Cell Joining Techniques

D.1 Bell and Spigot Joints

1. Bell and spigot segments were produced from tubes of $(\text{ZrO}_2)_{0.9}(\text{Y}_2\text{O}_3)_{0.1}$ by cutting and grinding to the dimensions shown in Fig. D1a.
2. Electrodes were applied as shown in Fig. D1b. Inside electrodes were masked and sprayed as described in Steps 1-6 of Appendix C.2. Outside electrodes were prepared either this way or by sputtering as described in Appendix C.1. Both the active electrode and joint regions were coated. The non-joint areas were painted with lacquer.
3. The joint area was platinum plated at a current density of 35 ma for 10 minutes. The plating bath consisted of a solution containing 2% platinum "P" salt, 10% sulfamic acid, and 88% distilled water. A coating thickness estimated at 0.0001 to 0.0002 inches resulted.
4. Using a K Au CN solution, gold plating was applied on top of the platinum plating. The current was 10 ma for one minute.
5. Segments were matched to obtain the tightest possible fit at all joints.
6. A gold wire was placed at the joint so that the gold would flow into the joint when heated. The size of wire varied between 4 and 8 mills in diameter, depending upon the tightness of fit.
7. The cell electrodes above the joints were painted with thick organic "Dag" solution to retard the surface migration of the gold onto the electrodes during firing.
8. In an H_2 atmosphere, the temperature was raised to 1100°C . The gold melted and interdiffused with the gold and platinum plating to form a gold-platinum alloy seal.

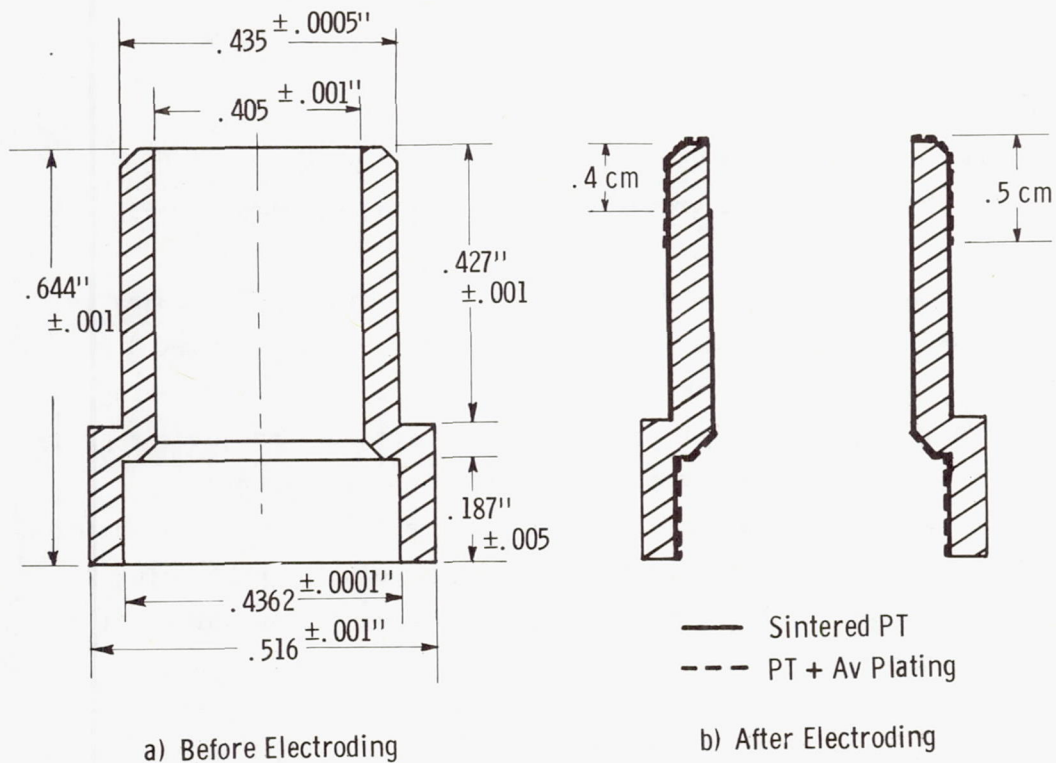


Fig. D1 - Section view of bell and spigot segment before and after electrode application

9. The joints were checked for leakage by pressurizing to 5 psig under water and looking for bubbles. If leaks were present, Steps 6, 7, and 8 were repeated until a tight battery was obtained or until a total of three firings had been carried out.

D.2 All Platinum Butt Joints

1. Segments were cut to length and optically polished.
2. A 10 mg/cm^2 coating of sintered platinum was applied at each end of each cell.
3. The segments, together with end cap and base tube were loaded into a spring-loaded apparatus (Fig. D2) which maintained alignment during subsequent firing and applied a compressive force of approximately 20 pounds (600 psi).
4. The apparatus loaded with the battery was then heated to 1800°C in an RF furnace with a 70% helium, 30% hydrogen atmosphere to melt the platinum and form the joints.
5. The battery was tested for leaks under 1-5 psig pressure in water.
6. The battery was fired in air to 1000°C , and, after cooling, again tested for leaks
7. Electrodes were applied to the inside and outside of the battery in the same manner as previously described in Section C.2 of Appendix C.

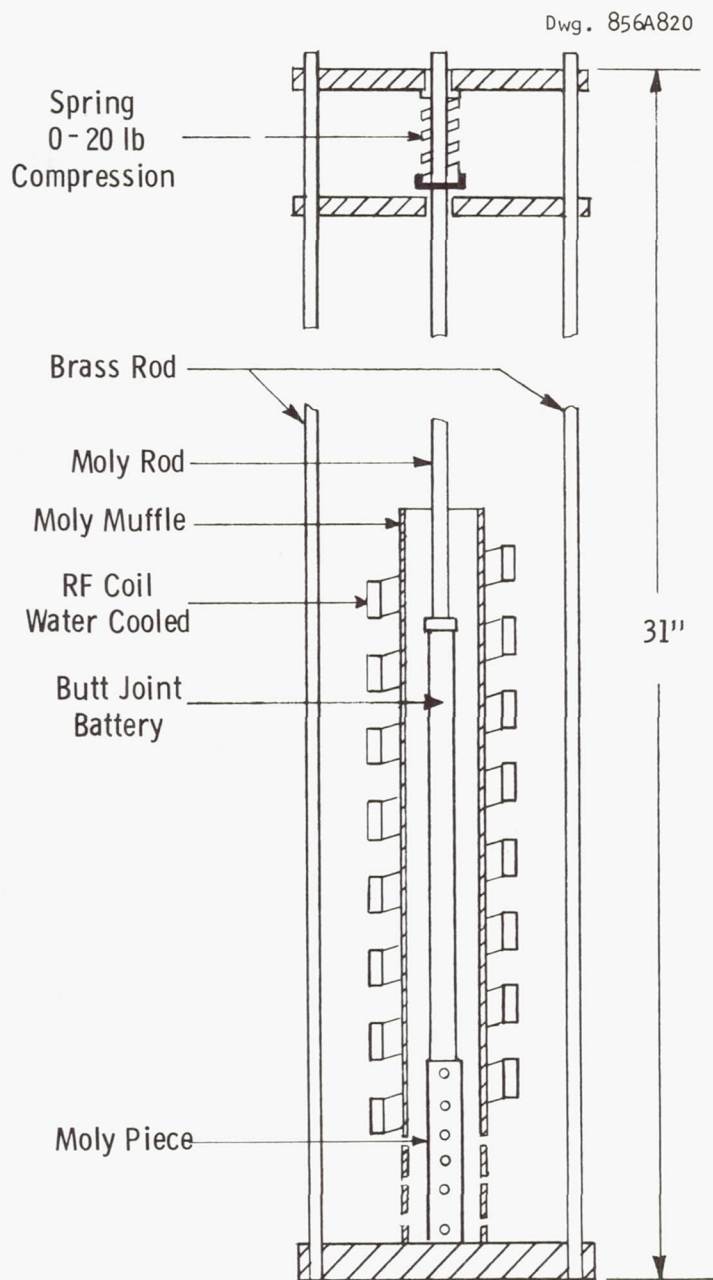


Fig. D2 - Butt jointing apparatus

APPENDIX E

Equations for Computerized Heat Transfer Computations

HYDRAULIC RADIUS

Circular Conduit:

$$R_H = \frac{D}{4} \quad (E-1)$$

Annulus:

$$R_H = \frac{D_2 - D_1}{2} \quad (E-2)$$

where

$$D_2 > D_1$$

LOG MEAN TEMPERATURE DIFFERENCE (See Fig. 49)

$$\Delta T_{LM} = \frac{(T_H - T_L) - (T_H' - T_L')}{\ln \left[\frac{(T_H' - T_L)}{(T_H - T_L')} \right]} \quad (E-3)$$

CONVECTIVE HEAT TRANSFER COEFFICIENTS

Circular Conduit:

$$h_{i1} = 1.86 \left[\frac{k}{D_{i1}} \right] \left[N_{Re} \right]^{1/3} \left[N_{Pr} \right]^{1/3} \left[\frac{D_{i1}}{L} \right]^{1/3} \quad (E-4)$$

Annulus:

$$h_{i2} = h_{o1} = 1.86 \left[\frac{k}{D_{o1}} \right] \left[N_{Re} \right]^{1/3} \left[N_{Pr} \right]^{1/3} \left[\frac{D_{o1}}{L} \right]^{1/3} \quad (E-5,6)$$

Overall Heat Transfer Coefficient Based on the Inside Area of Tube 1:

$$U_{i1} = \left[\frac{1}{h_{i1}} + \frac{D_{i1} \ln \left(\frac{D_{o1}}{D_{i1}} \right)}{K_1} + \frac{D_{i1}}{D_{o1} h_{o1}} \right]^{-1} \quad (E-7)$$

Overall Heat Transfer Coefficient Based on the Outside Area of the Insulation:

$$U_o = \left[\frac{D_{oo}}{D_{i2} h_{i2}} + \frac{D_{oo} \ln \left(\frac{D_{o2}}{D_{i2}} \right)}{K_2} + \frac{D_{oo} \ln \left(\frac{D_{oo}}{D_{o2}} \right)}{K_3} \right]^{-1} \quad (E-8)$$

PRESSURE DROPS

Circular Conduit, Laminar Flow:

$$\Delta P_1 = P_1 - P_2 = P_1 - \left[P_1^2 - \frac{256 R T \mu L F}{\pi D_{i1}^4 g M} \right]^{1/2} \quad (E-9)$$

Annulus, Laminar Flow:

$$\Delta P_1 = P_1 - P_2 = P_1 - \left[P_1^2 - \frac{256 R T \mu L F}{\pi g M (D_{i2}^2 - D_{o1}^2) \left(D_{i2}^2 - D_{o1}^2 - \frac{D_{i2}^2 - D_{o1}^2}{\ln \left(\frac{D_{i2}}{D_{o1}} \right)} \right)} \right]^{1/2} \quad (E-10)$$

VELOCITY

Circular Conduit:

$$v_1 = \left[\frac{4 F}{\rho \pi D_{i1}^2} \right] \quad (E-11)$$

Annulus:

$$v_2 = \left[\frac{4 F}{\rho \pi (D_{i2}^2 - D_{o1}^2)} \right] \quad (E-12)$$

ENTHALPY BALANCE FOR HEAT EXCHANGER OF FIG. 49

Overall Balance:

$$QT - (QX - QL) - QO = 0$$

where QT is calculated from the high temperature stream:

$$QT = [CP] [F(j)] [TH - TA]$$

QX is fixed by the Ratio: $Z = \left(\frac{QX}{QT} \right)$, {an assumed value}

$$QX = Z QT = V_{i1} A_i \Delta T_{LM}$$

QL is fixed by an assumed loss Ratio: $RT = \frac{QL}{QX}$

$$QL = (Z QT) (RT) = V_o A_o \Delta T$$

and

$$QO = QT (1 - Z) = [CP] [F] [TH' - TA]$$

EMPIRICAL EQUATIONS DEFINING TRANSPORT PROPERTIES

Viscosity:

$$\mu_n = \frac{\int_{T_{Lo}-1}^{T_{Hi}+1} [a_n + b_n T + c_n T^2 + d_n T^3 + e_n T^4 + f_n T^5] dt}{(T_{Hi} - T_{Lo} + 2)} \quad (E-13)$$

of a mixture:

$$\mu_{mix} = \frac{\sum_{n=1}^n \frac{c_n \mu_n}{\sum_{m=1}^m c_m \phi_{nm}}}{\quad} \quad (E-14)$$

$$\text{where } \phi_{nm} = \frac{1}{\sqrt{8}} \left(1 + \frac{M_n}{M_m}\right)^{-1/2} \left[1 + \left(\frac{\mu_n}{\mu_m}\right)^{1/2} \left(\frac{M_m}{M_n}\right)^{1/4} \right]^2$$

Thermal Conductivities:

$$k_n = \frac{\int_{T_{Lo}-1}^{T_{Hi}+1} k_o \left(\frac{T}{T_o}\right)^\ell dT}{(T_{Hi} - T_{Lo} + 2)} \quad (E-15)$$

of a mixture

$$k_{mix} = \frac{\sum_{m=1}^m c_n k_n (M_n)^{1/3}}{\sum_{n=1}^n c_n (M_n)^{1/3}} \quad (E-16)$$

Heat Capacities:

$$C_{P_n} = \frac{\int_{T_{Lo}-1}^{T_{Hi}+1} [a_n + b_n T + c_n T^2 + d_n T^3 + e_n T^4] dt}{(T_{Hi} - T_{Lo} + 2)} \quad (E-16)$$

of a mixture:

$$C_{P_{(mix)}} = \sum_{n=1}^n z_n C_{P_n}$$

Identifying All Temperatures, Flow Streams and Transport Properties from
Stream Number (j) in Which They Occur

Exchanger 1

$$QT = Q10$$

$$TA = 20^{\circ}\text{C}$$

$$QX = (Z)(Q10)$$

$$TH = T10$$

$$QL = QL$$

$$TH' = T11$$

$$QO = Q11$$

$$F(j) = F10, F11, F1, F2$$

$$CP_{\text{High}} = CP10$$

Exchanger 2

$$QT = Q6$$

$$TA = 20^{\circ}\text{C}$$

$$QX = (Z)(Q6)$$

$$TH = T6$$

$$QL = QL$$

$$TH^1 = T7$$

$$QO = Q7$$

$$F(j) = F6, F7, F4, F9$$

$$CP_{\text{High}} = CP6$$

NOMENCLATURE LISTING FOR
HEAT EXCHANGER SIMULATION

Subscripts

- i = a value on the inside surface of a tube
- j = a stream number j = 1 to 13
- n,m = denotes component n or m, where n or m can be CO, CO₂,
H₂O, H₂, C, O₂
- φ = denotes a value measured on the outside surface of a
tube
- φφ = an overall or outside dimension
- lm = a log mean difference

Numerical Subscripts

- 1 = inner tube (circular cross-section) of a heat exchanger
- 2 = outer tube (annular cross-section) of a heat exchanger
- 3 = insulation
- 4 = catalyst
- 5 = reactor vessel

Superscripts

- super o = initial
- super s = equilibrium value

Greek Letter

- ρ = density [lb/ft³]
- μ = viscosity [lb/hr ft]

Lower Case Letters

- c_n = mass function of component n in a stream
- h = convective heat transfer coefficient [BTU/hr ft² °C]

k	= thermal conductivity of a gas phase [BTU/hr ft °C]
k_m	= mass transfer coefficient [lb moles/hr ft ²]
x_n	= mole fraction of component n
g	= gravitational unit conversion constant [lb _m ft/lb _f hr ²]
v	= bulk stream velocity [ft/hr]

Upper Case Letters

A	= area for heat transfer [ft ²]
C_p	= heat capacity [BTU/lb °C]
D	= diameter of a heat exchanger component [ft]
ΔD	= a tube wall thickness of a heat exchange tube [ft]
DR	= diameter of a reactor component [ft]
ΔDR	= a wall thickness of a reactor component [ft]
F	= mass flow rate [lb/hr]
G	= mass velocity [lb/hr ft ²]
K	= thermal conductivity of a solid phase [BTU/hr ft °C]
KEQ	= equilibrium constant
L	= length of a heat exchanger [ft]
LR	= length of a reactor [ft]
M	= molecular weight of a component or stream [lb/lb mole]
MF	= molar flow rate [lb mole/hr]
N_{Re}	= Reynolds Number $(\frac{GD}{\mu}) = (\frac{4F}{\pi D \mu})$
N_{Pr}	= Prandtl Number $(\frac{C_p \mu}{k})$
P	= pressure [lb/ft ²]
QA	= heat added [BTU/hr]
QT	= total amount of heat available for heat transfer in a heat exchanger [BTU/hr]
QL	= total amount of heat loss [BTU/hr] through insulation
QO	= total amount of heat in effluent stream [BTU/hr]
QX	= total amount of heat (part of QT) that is transferred between the hot and cold stream of a heat exchanger [BTU/hr]
QRRX	= amount of heat transferred from the carbon deposition reactor [BTU/hr]

$Q(j)$ = the total amount of heat in a stream measured from 20°C up to $T(j)$ [BTU/hr]
 R = ideal gas law constant
 (RT) = (Q_L/Q_X) , the ratio of the amount of heat lost through the insulation of a system component to that exchanged into the stream in question
 ΔT = a temperature change [°C]
 T_A = ambient temperatures [°C]
 T_H = stream temperatures of hot stream entering a heat exchange [°C]
 T_H' = stream temperature of hot stream leaving a heat exchange [°C]
 T_L = stream temperature of cold stream entering a heat exchange [°C]
 T_L' = stream temperature of cold stream leaving a heat exchanger [°C]
 $T(j)$ = temperature of stream (j) [°C]
 T_O = outside wall temperature of the insulation on a heat exchanger [°C]
 T_{OR} = outside wall temperature of the insulation or a reactor [°C]
 U = overall heat transfer coefficient, [BTU/hr ft² °C]
 W = a physical weight of construction materials [lb]
 $W\Delta P$ = weight penalty for pumping [lb]
 $WPEN$ = weight penalty for heating or cooling [lb]
 WT = total weight of heat exchanger [lb]
 WCT = weight of catalyst [lb]
 WRN = weight of insulation around reactor vessel [lb]
 WRV = weight of reactor vessel [lb]
 WCB = carbon collector bottle weight [lb]
 WRS = subweight of reactor [lb]
 WR = total physical weight of reactor [lb]
 WRP = weight penalty for cooling requirement of reactor [lb]
 WRT = total reactor weight ($WRP + WR$). [lb]

APPENDIX F

DAILY LOG OF 100-DAY LIFE TEST
OF CARBON DEPOSITION REACTOR

Day	Gas Input, cc/min ^a			Temp. °C	Carbon Deposit, g	Iron in Deposit, %
	CO	CO ₂	H ₂			
1	160	39	10	579	28.9	5.08
2	160	39	9	590	33.7	
3	195	--	8	590	47.7	
4	195	--	8	564	48.2	
5	195	--	8	569	49.1	
6	162	40	8	569	36.6	2.76
7	162	40	9	569	35.3	
8	162	40	14	577	32.1	
9	163	46.5	9	569	35.0	
10	163	46.5	9	569	44.2	
11	165	46	8	577	32.3	6.10
12	165	47	8.5	577	32.8	
13	165	46.5	8.5	569	33.9	
14	170	46.5	11.5	571	25.0	
15	170	46.5	9.5	571	47.8	
16	170	46.5	9	569	31.7	4.08
17	170	46.5	9.5	573	37.9	
18	170	46.5	13.5	575	35.8	
19	170	46.5	13.5	576	38.2	
20	170	46.5	13.5	571	43.9	
21	170	46.5	13.5	571	34.3	5.40
22	170	46.5	13.5	571	44.5	
23	170	46.5	13.0	572	46.6	
24	170	46.5	13.5	572	23.7	
25	170	46.5	7.5	575	40.7	
26	170	47	7.5	577	29.3	2.73
27	170	46.5	7	574	42.0	
28	170	46.5	7	572	31.7	
29	170	46.5	7	577	39.2	
30	170	46.5	7.5	572	41.9	

APPENDIX F - CONTINUED
DAILY LOG OF 100-DAY LIFE TEST
OF CARBON DEPOSITION REACTOR

Day	Gas Input, cc/min ^a			Temp. °C	Carbon Deposit, g	Iron in Deposit, %
	CO	CO ₂	H ₂			
31	170	46.5	7.5	582	41.7	3.19
32	170	46.5	7	593	31.2	
33	170	46.5	7	593	33.8	
34	170	46.5	7	595	33.8	
35	170	46.5	7.5	595	39.1	
36	170	46.5	7	559	38.2	3.50
37	170	46.5	7	549	39.8	
38	170	46.5	7	547	40.2	
39	170	46.5	7.5	554	37.0	
40	170	46.5	7.5	549	39.3	
41	170	46.5	7.5	546	37.3	5.21
42	170	46.5	8	545	37.7	
43	170	46.5	8.5	549	30.3	
44	170	46.5	7	580	11.4	
45	170	--	30.0	585	30.3	
46	170	46.5	9	571	41.1	7.20
47	170	46.5	9	573	33.4	
48	170	46.5	10	572	31.9	
49	170	46.5	10	572	31.3	
50	170	46.5	10	571	44.7	
51	170	46.5	10	561	41.2	4.32
52	170	46.5	10	561	33.1	
53	170	46.5	10	564	44.1	
54	170	46.5	10	562	33.8	
55	170	46.5	10	557	38.1	
56	170	46.5	10	559	47.0	4.93
57	170	46.5	10	558	34.8	
58	170	46.5	10	547	37.9	
59	170	46.5	10	539	46.9	
60	170	46.5	10.5	543	39.0	
61	170	46.5	10.5	537	33.3	3.95
62	170	46.5	10.5	534	50.6	
63 ^b	340	89.0	19	537	61.9	
64	340	89.0	19	535	82.7	
65	340	89.0	18.5	532	78.6	

APPENDIX F - CONTINUED
DAILY LOG OF 100-DAY LIFE TEST
OF CARBON DEPOSITION REACTOR

Day	Gas Input, cc/min ^a			Temp. °C	Carbon Deposit, g	Iron in Deposit, %
	CO	CO ₂	H ₂			
66	340	89.0	19.0	534	76.1	3.37
67 ^b	170	46.5	9.5	533	48.0	5.80
68	170	46.5	9.5	499	39.1	
69	170	46.5	9.5	499	43.3	
70	170	46.5	9.5	493	39.2	2.64
71 ^b	340	89.0	19.5	492	76.5	
72	340	89.0	19.5	492	80.1	2.34
73	340	89.0	20	499	81.1	1.98
74 ^b	170	46.5	10	537	37.5	
75	170	46.5	10	537	33.9	
76	170	46.5	10	541	43.1	4.67
77	170	46.5	9.5	541	39.7	
78	170	46.5	10	595	39.8	
79	170	46.5	10	598	32.5	4.60
80	170	46.5	10	599	35.6	
81	170	46.5	10.5	601	41.5	
82	170	46.5	13.5	600	29.0	4.16
83	170	46.5	13.5	599	36.1	
84	170	46.5	13.5	544	46.0	
85	170	46.5	13.5	539	42.3	5.79
86	170	46.5	13.5	539	42.2	
87	170	46.5	6	537	51.0	
88	170	46.5	6	539	30.8	2.61
89	170	46.5	6	540	41.7	
90	170	46.5	6	540	42.8	
91	170	62	10	541	27.2	3.56
92	170	62	10	539	38.7	
93	170	62	10	541	47.4	
94	170	33.5	10	541	35.6	4.26
95	170	33.5	10	539	41.3	
96	170	33.5	9.8	539	47.9	
97	170	33.5	9.8	539	40.3	5.02
98 ^b	170	33.5	9.8	541	41.7	
99	680	192	40.5	541	138.6	
100	680	192	41	543	144.1	2.82
101	680	192	41	544	151.5	

a Flow rate at 25°C, 730 mm Hg

b Gas flow rates were changed; majority of day was at flows indicated.

REFERENCES

1. Elikan, L., D. H. Archer and R. L. Zahradnik: Aerospace Life Support. L. Elikan, Editor, American Inst. of Chem. Eng., N. Y. (1966), pp. 30-37.
2. Chandler, H. W. and W. Oser, AMRL-TDR-62-16 (1962).
3. Chandler, H. W., AMRL-TDR-64-62 (May 1964).
4. Chandler, H. W. and F. Z. Pollara: Aerospace Life Support. L. Elikan, Editor, American Inst. of Chem., N. Y. (1966) pp. 38-42.
5. Weissbart, J. and W. H. Smart, NASA CR-680 (February 1967).
6. Archer, D. H., L. Elikan, R. J. Zahradnik: The Performance of Solid-Electrolyte Cells and Batteries on CO-H₂ Mixtures; A 100-Watt Solid Electrolyte Power Supply. Hydrocarbon Fuel Cell Technology, Academic Press, New York (1965), pp. 51-75.
7. Alcock, C. B.: The Gaseous Oxides of Platinum Metals. Platinum Metals Review, 5 (1961), pp. 134-139.
8. Archer, D. H. et al.: An Investigation of Solid Electrolyte Fuel Cells. ASD-TDR-63-448 (July 1963).
9. Walker, P. L., J. F. Rakszawski, and G. R. Imperial: J. Phys. Chem., 63 (1959), pp. 133-148.
10. Haas, L. A., S. E. Khalafalla, and P. L. Weston, Jr.: Bur. Mines Rept. of Investigation 7064 (January 1968).
11. T. F. Berry, R. N. Ames, and R. B. Snow: J. Am. Cer. Soc., 39 (1956), pp. 308-318.
12. Jacques Hui: Bull. Soc. Chimique de France, 8-9 (1963), pp. 1619-1629.
13. Taylor, J.: J. Iron and Steel Inst., 184 (1956). pp. 1-6.
14. Donald, H. J., An Annotated Bibliography of the Literature and Patents Relating to the Production of Carbon by the Decomposition of Carbon Monoxide. Mellon Inst. of Ind. Research, Pittsburgh (1956).
15. Gleuckert, A. J. and G. A. Remus: NASA CR-66403.

16. McAdams, W. H.: Heat Transmission. 3rd ed., McGraw-Hill, New York (1954), p. 233
17. Dushman, Saul: Scientific Foundations of Vacuum Technique. 2nd ed., John Wiley & Sons, New York, (1960), p. 24.
18. Seybolt, A. U. and J. E. Burke: Procedures in Experimental Metallurgy. John Wiley & Sons, New York (1953), p. 110.
19. Hunter, J. P.: Ultrapure Hydrogen by Diffusion Through Palladium Alloys. Presented at Symposium on the Production of Hydrogen, Am. Chem. Soc., New York (1963).
20. Lewis, F. A.: The Palladium Hydrogen System. Academic Press, New York (1967) pp. 94-117.
21. Barlow, R. E., F. Proschan, and L. C. Hunter: Mathematical Theory of Reliability. John Wiley & Sons, New York (1967).
22. Duffin, R. J., E. L. Peterson and C. Zener: Geometric Programming. John Wiley & Sons, New York (1967), p. 176.
23. Paliguev, S. F., and A. D. Neuimin: Study of the Type of Conductivity of Solid Oxides. Doklady Academic Nauk SSSR (English Translation) 141 (1961), pp. 90-96.
24. Sverdrup, E. F. et al.: Testing of Electrodes for High-Temperature Solid-Electrolyte Fuel Cells. Hydrocarbon Fuel Cell Technology, Academic Press, New York (1965) pp. 311-333.
25. Thermophysical Properties Research Center Data Book. Vol. II, Purdue University (1966).
26. Bird, R. B., W. E. Stewart and E. N. Lightfoot: Transport Phenomena. John Wiley & Sons, New York, (1960), p. 24.
27. Tsedesberg, N. V.: Thermal Conductivity of Gases and Liquids. M.I.T. Press, Cambridge (1965).
28. Chemical Engineers' Handbook, 4th ed., R. H. Perry, ed., McGraw-Hill, New York (1963).